

2013 (Heisei 25)

Doctoral Thesis

Predicting and Controlling Sediment Runoff caused by Heavy Rain in a Mountain Watershed

by

Norio Harada

River Department, Erosion Control Division, Mitsui Consultants Co., Ltd., Japan

P. E. J. (Civil Engineering: *River, Coastal & Ocean Engineering and Soil Mechanics & Foundation*)

Ritsumeikan University

Graduate School of Science and Engineering

Doctoral Program in Science and Engineering

Norio Harada

ACKNOWLEDGMENT

First of all, I would like to take this opportunity to express my deepest gratitude to my supervising professor, Yoshifumi Satofuka, at the Department of Civil Engineering, Ritsumeikan University, for all of the encouragement, support and insights over the years. Thanks for giving me the opportunity to study this fascinating subject with the freedom to choose my research topics during my doctoral program at Ritsumeikan University.

I would like to thank the staff members of the Department of Civil Engineering, Ritsumeikan University; Faculty of Agriculture, Kyoto University; and the Disaster Prevention Research Institute, Kyoto University. The suggestions of Professor Ryoichi Fukagawa and Professor Kazuyuki Izuno at the Department of Civil Engineering, Ritsumeikan University, were very helpful in clarifying this thesis.

The financial support provided by Mitsui Consultants Co., Ltd. is gratefully acknowledged.

Norio Harada
March, 2014

ABSTRACT

In Japan, there have been numerous problems associated with sediment runoff processes, including countermeasures against flooding caused by landslide dam collapses. To control sediment runoff, structures have been built in our rivers; however, problems in managing these structures often arise. Recently, it has been reported that new facilities to control sediment runoff have not functioned correctly. In addition, there have been reports of flood hazards caused by the failure of old irrigation levees due to heavy rainfall and earthquakes. Furthermore, deposition of sediment in dam reservoirs of a mountain watershed is a significant problem, and control measures are required to maintain these facilities.

To control sediment runoff, accurate predictions of the runoff are required, which take the prevailing conditions (*e.g.*, climate and geographical features) into account. This thesis aims to develop methods to predict and control the sediment runoff in a mountain watershed area, using experimentally measured and simulated data. First, the deformation and flood outflow processes accompanying landslide dam failure were investigated using field experiments with a small-scale artificial landslide dam. The effects of moisture content on erosion of landslide dams were investigated using a numerical model that incorporated both erosion and infiltration processes. In addition, the dependence of the flood runoff to the downstream area on the characteristics of the inflow hydrograph from the reservoir was analyzed, and a new index of flood risk was arrived at. We developed an existing numerical model to create a novel technique to predict flooding and sediment deposition, and the validity of this model was assessed via comparison of observations and simulated data. Finally, an ideal structure to control sediment runoff was identified, examining the function of multiple grid SABO dam design parameters, and the function of grid SABO dams constructed under different design guidelines was evaluated considering the grain-size distribution of the sediment. This thesis describes methods to predict and control sediment runoff in the design of these structures.

Norio Harada
March, 2014

CONTENTS

Acknowledgment

Abstract

Chapter 1: Introduction	1
Chapter 2: Sediment Discharge caused by Landslide Dam Failure	5
2.1. Introduction	5
2.2. Deformation processes based on field observation data	9
2.3. Numerical analysis of erosion processes due to overtopping of landslide dams	11
2.4. Factors that affect flood outflow in real life	21
2.5. Numerical analysis of landslide dam failure considering infiltration flow	25
2.6. Summary	36
BIBLIOGRAPHY	38
Chapter 3: Flood Runoff Processes affected by Hydrographic Characteristics	40
3.1. Introduction	40
3.2. Numerical analysis of flood runoff processes affected by hydrographic differences	41
3.3. Evaluation of flood runoff affected by the hydrographic characteristics	46
3.4. Summary	48
BIBLIOGRAPHY	48
Chapter 4: Prediction of Sediment Runoff in a Mountain Watershed	49
4.1. Introduction	49
4.2. Prediction of channel width using the basin area	50
4.3. Numerical analysis for prediction of sediment runoff in mountain channels	57
4.4. Summary	75
BIBLIOGRAPHY	76
Chapter 5: Debris Flow Control by Steel-grid Sabo Dams	77
5.1. Introduction	77
5.2. Ideal structure of a grid SABO dam for controlling sediment runoff	79
5.3. Evaluating capture rate versus grain-size distribution in a real mountain streambed	88
5.4. Summary	92
BIBLIOGRAPHY	93
Chapter 6: Conclusions and Future Works	94

Chapter 1

Introduction

“For wisdom will enter your heart, and knowledge will be pleasant to your soul.”

Proverbs 2:10

Generally, in Japan, sediment yield and runoff are affected by the steep geographical features, vulnerable geological structures, and heavy rain due to typhoons or the rainy season. Many problems related to sediment processes in watersheds and coastal areas have been reported. To control sediment runoff, structures have been constructed in our rivers. Furthermore, new structures such as permeable SABO dams have been developed after considering the reduction of construction costs and environmental problems. However, many of these structures still need to be managed appropriately.

There are numerous examples of damage caused by excessive sediment yield and runoff. For example, in 2011, *Tropical Storm Talas* dumped heavy rain on Wakayama, Nara, and Mie prefectures, turning a large portion of the area into swamps. The Japan Geotechnical Society *et al.* (2011) reported that the total sediment yield caused by the heavy rain was approximately one billion m³. The heavy rain caused sediment disasters, such as debris flows and landslides. To counter the flooding caused by landslide dam failure, these hazards must be predicted to make countermeasures. Nevertheless, many residents had to be evacuated for a long period to escape the landslides caused by large-scale slope collapse in mountain watersheds.

It has been reported that the facilities controlling sediment runoff are not functioning properly. To

prevent disasters due to debris flow in mountain watersheds, steel-grid SABO dams have been constructed both to preserve the fluvial environment (*i.e.*, ensure continuous mobility) in the river and to increase the capture capacity of the dam (the design code for SABO dam 2007), compared to the initial impermeable SABO dams. However, Yoshida *et al.* (2010) reported that a steel-grid SABO dam failed to capture the sediment when debris flow occurred in the Hachiman Valley in Hofu, Yamaguchi Prefecture, in 2009. This failure was postulated to have occurred when the coarse particles necessary for blockade could not flow to the dam, namely, separated from the debris flow and were deposited on the gradually sloping riverbed upstream from the dam. In the future, the blockade characteristics should be understood after considering the field conditions.

The maintenance management problems reported to the River Institute in recent years includes flood hazards caused by the failure of an old pond levee that was not managed properly due to heavy rains and earthquakes. Hori (2005) showed the need for measures to counter the floods caused by levee failure of an irrigation tank. Furthermore, deposition in the reservoir of a hydroelectric dam in a mountain watershed was an important problem; the development of a numerical model to predict the deposition in the reservoirs and control measures are important. In addition, the deposition in the reservoir of a real mountain stream is more rapid than that assumed initially due to sediment caused by heavy rain in a mountainous area (Kawata *et al.*, 2010). Therefore, a numerical model sufficiently accurate to predict sediment runoff in mountain streams must be developed immediately.

Generally, river management organizations need to control sediment runoff to prevent sediment disasters downstream. Therefore, the prediction of sediment runoff considering the conditions (*e.g.*, the climate and geographical features) is important to control sediment runoff. Furthermore, the design must consider the field conditions generating sediment runoff, based on the mechanisms of sediment yield and sediment runoff processes, which are not fully understood.

This thesis sought to develop a method for predicting and controlling the sediment runoff caused by heavy rain in a mountain watershed. The sediment runoff processes in a mountain watershed caused by heavy rain were analyzed using both experimental results and numerical models, in order to design countermeasures that take into consideration the appropriate field conditions.

This thesis is organized as follows:

Chapter 1 presents the research background and problems with sediment runoff in a mountain watershed. The motivation for and objectives of the thesis are then outlined.

Chapter 2 presents the landslide dam deformation processes and outflow discharge from burst landslide dams to compare experimental results in a mountain stream with the results calculated using a numerical model (Takahashi *et al.*, 2002), and the factors that affect the outflow processes from landslide dams using a numerical model, as shown by Harada *et al.* (2013a). In addition, landslide-dam deformation caused by erosion due to overtopping, after the moisture content is taken

into consideration, is discussed together with the numerical results, as shown by Harada & Satofuka (2012).

Chapter 3 focuses on the effects of the hydrographic characteristics on flood runoff processes; the flow discharge is analyzed under different flow conditions, using a one-dimensional model (Takahashi & Nakagawa, 1991), as shown in Harada *et al.* (2013b).

Chapter 4 outlines the development of the numerical model used to predict the sediment runoff in a mountain watershed, taking into consideration the sediment yield caused by slope failure. In addition, the calculated and observed data for a mountainous area were compared to confirm the validity of the numerical model. Furthermore, a new relationship between the watershed area and channel width is proposed based on a statistical analysis of data from over 800 mountain streams, as shown by Harada & Satofuka (2013a).

Chapter 5 presents the ideal structure of a steel-grid SABO dam for controlling debris flow using laboratory results under different conditions, as shown by Harada & Satofuka (2013b). In addition, the capture rate of steel-grid SABO dams, based on the design code for SABO dams and taking into consideration the field conditions (grain-size distribution), is evaluated.

Chapter 6 summarizes the main conclusions of this thesis, which were presented at the end of each chapter. This chapter discusses the prediction and control of sediment runoff caused by heavy rain in a mountain watershed, along with future work.

BIBLIOGRAPHY

1. Harada N, Akazawa F, Hayami S & Satofuka Y. 2013a. Numerical simulation of landslide dam deformation caused by erosion. *Advances in River Sediment Research*, ISBN 978-1-138-00062-9: 1107-1116.
2. Harada N, Akazawa F, Hayami S & Satofuka Y. 2013b. Prediction of runoff characteristic due to irrigation tank overflow. *Annual Journal of Hydro science and Hydraulic Engineering*, Vol. 69: 1213-1218.
3. Harada N & Satofuka Y. 2012. Numerical simulation to predict deposit deformation due to erosion for saturated and unsaturated conditions. *Advances in River Engineering*, Vol. 18: 287-292.
4. Harada N & Satofuka Y. 2013a. Numerical prediction of flooding considering sediment runoff. *Advances in River Engineering*, Vol. 19: 217-222.

5. Harada N & Satofuka Y. 2013b. Counterplans for hazards due to debris flow around a historic site: site considerations. *Disaster Mitigation of Cultural Heritage and Historic Cities*, Vol. 7: 31-38.
6. Hori T. 2005. Damage of small earth dams for irrigation induced by heavy rainfall. *Technical Report of the National Institute for Rural Engineering*, Vol. 44: 139-247.
7. Kawata N, Yamamoto M, Shikano K, Yoshino H & Fujita M. 2010. Study on prediction of reservoir sediment progress affected by climate change. *Advances in River Engineering*, Vol. 16: 65-70.
8. National Institute for Land and Infrastructure Management Ministry of Land, Japan. 2007. *Manual of Technical Standard for designing Sabo facilities against debris flow and driftwood*.
9. Takahashi T & Nakagawa H. 1991. Prediction of stony debris flow induced by severe rainfall. *Journal archive/sabo*, Vol.44/ No.3: 12–19.
10. Takahashi T, Nakagawa H & Satofuka Y. 2002. Study on sediment flushing using a reverse-flow system. *Disaster Prevention Research Institute Annuals for Kyoto University*, No.45/B: 91-100.
11. The Japan Geotechnical Society, the Seismological Society of Japan, Japan Society of Engineering Geology, Kansai Geotechnical Consultants Association, and Committee Chubu Geotechnical Consultants Association. 2011. Survey report of the Landslides caused by typhoon No. 12 in Kii Peninsula, Japan.
12. Yoshida K, Yamaguchi S, Oosumi H, Isikawa N & Mizuyama T. 2010. Case study of debris flow controlled by grid dams. *Annual research presentation meeting, Japan Society of Erosion Control Engineering*, A: 192-193.

Chapter 2

Sediment Discharge caused by Landslide Dam Failure

“So God made the vault and separated the water under the vault from the water above it. And it was so.”

Genesis 1:7

2.1. Introduction

Landslide dams are caused by large-scale slope collapse. Predicting their failures is important because hazardous flooding may result when landslide dams burst and rapidly release their reservoirs of headwater. Landslide dam failure has been investigated in many papers (*e.g.*, Takahashi & Kuang, 1988; Mizuyama *et al.*, 1989; Chiba, 2013; Mori *et al.*, 2011). Takahashi and Kuang (1988) identified three types of dam deformation, as shown in **Figure 2.1**: (1) erosion due to overtopping, (2) instantaneous slip failure, and (3) progressive failure caused by infiltration flow. Almost all previous methods of predicting these phenomena have relied on numerical models developed for each deformation type. Mizuyama *et al.* (1989) showed that most landslide dam failures were caused by erosion due to overtopping. However, the exact mechanisms are not fully understood, as shown in **Figure 2.2**. Chiba (2013) indicated a relationship between the landslide dam deformation processes and the vertical section form of the dam, using landslide dam failures that occurred recently.

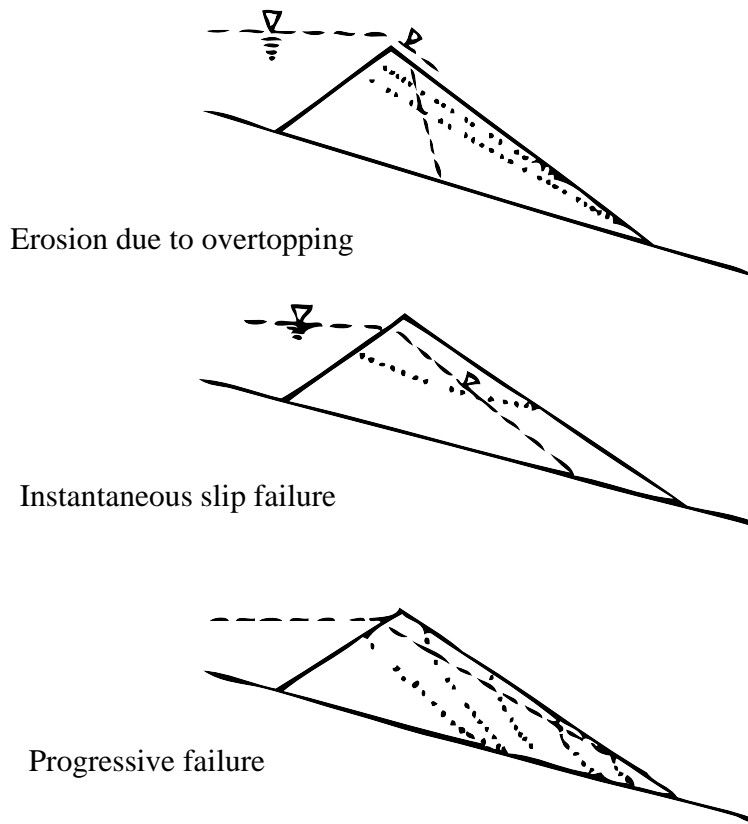


Figure 2.1: Three types of dam failure (Takahashi & Kuang, 1988).

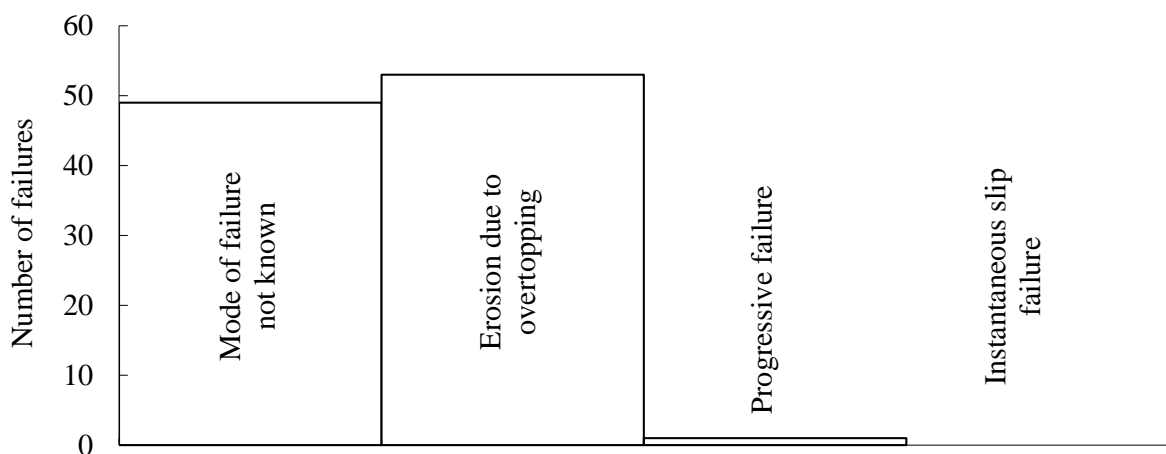


Figure 2.2: Modes of failure in landslide dams based on 103 failures (Mizuyama *et al.*, 1989).

Mori *et al.* (2011) reported 168 landslide dam failures that occurred in Japan. To understand the factors determining the height of the landslide dam, these factors combined with information on the

dams' altitude above sea level (**Figure 2.3**) were analyzed using a statistical analysis technique (Mathematical Quantification Theory Class III) in this study. The results suggest that the reservoir volume, height, and landslide area of landslide dams caused by heavy rain are smaller than those of landslide dams caused by earthquakes. Additionally, the results suggested a relationship between the area of the basin above the dam and the height of the landslide dam.

In this study, multiple regression analysis was used to identify the factors affecting landslide dam height, in an effort to provide a model for easily predicting landslide dam height. These factors were extracted using a stepwise method, based on 51 failures of landslide dams caused by earthquakes.

The landslide dam height caused by earthquakes H_1 is given as follows:

$$H_1 = 0.095h_l + 0.033h_0 - 17i_s - 0.017l_h - 0.0046A_1 + 0.06A_2, \quad (2.1)$$

where h_l is the height from the head of the landslide to the stream bed, h_0 is the altitude from the sea level, i_s is the gradient of slope (height/distance), l_h is the horizontal distance from the landslide to the stream bed, A_1 is the upstream basin area from a river channel blockage point, and A_2 is the landslide area. **Figure 2.4** shows a comparison between the observations and calculations using equation (2.1) for the heights of landslide dams. The correlation coefficient of equation (2.1) is 0.81.

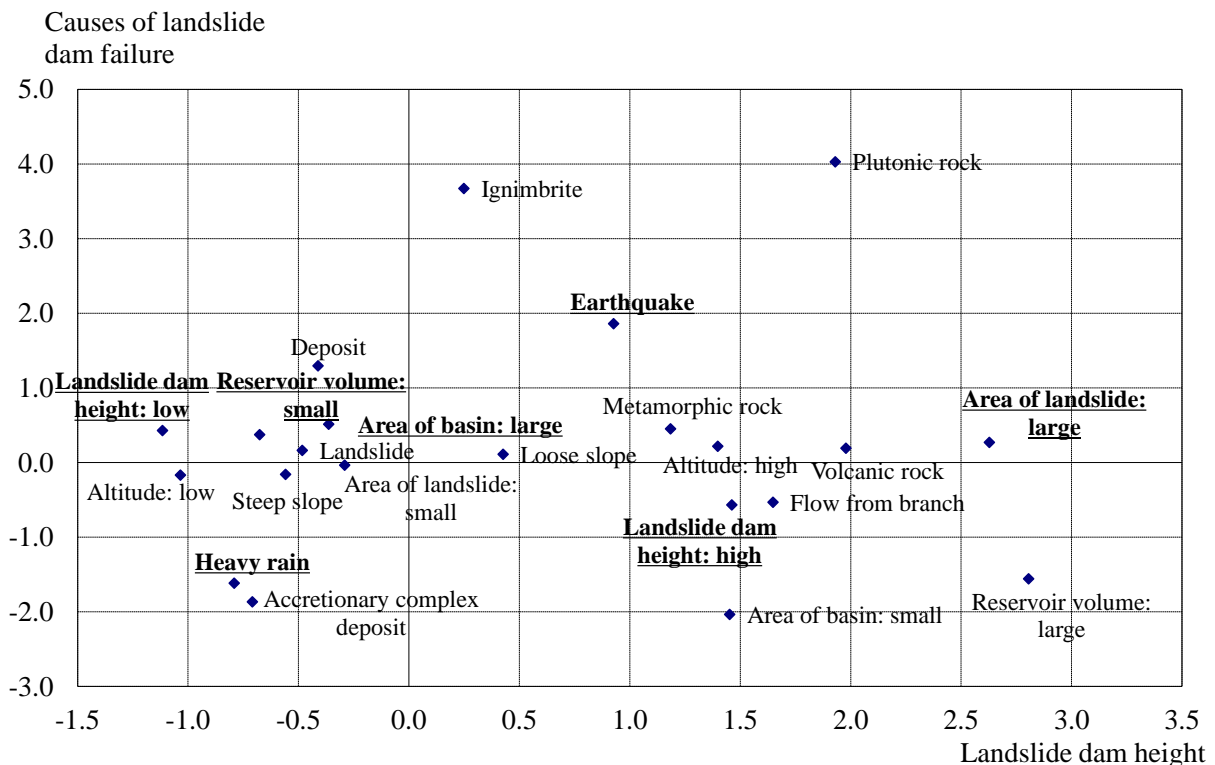


Figure 2.3: Factors determining landslide dam height using Mathematical Quantification Theory Class III.

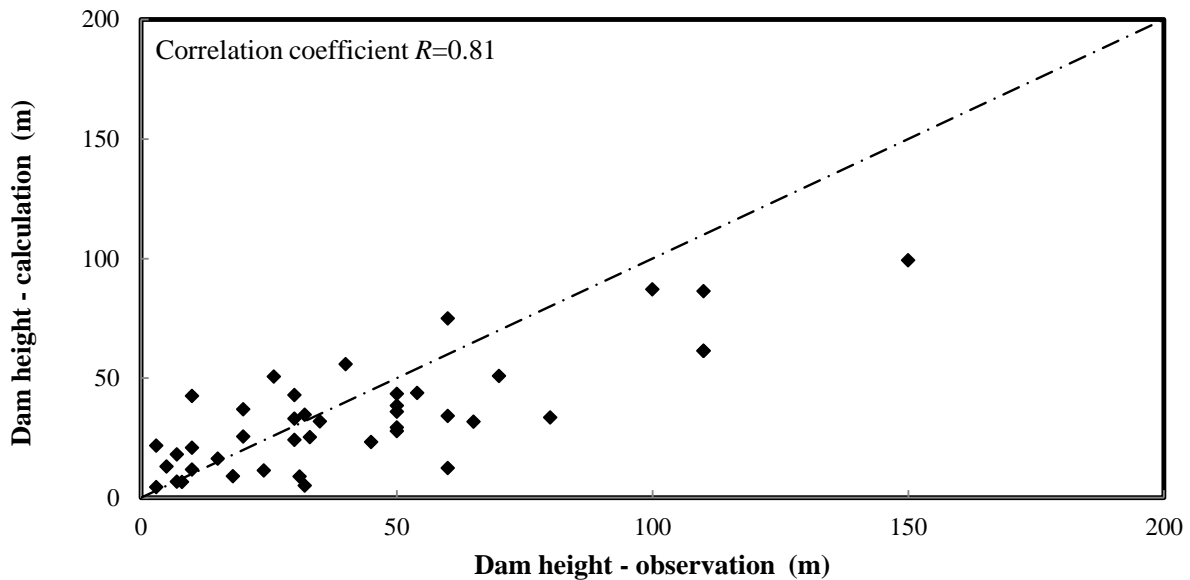


Figure 2.4: Comparison between observations and calculations for the landslide dam height.

However, a detailed explanation of the factors is limited due to the lack of detailed information on landslide dam failures. In the future, more examples of landslide dam failures that have occurred abroad will be analyzed.

Many studies of landslide dam failure have been performed under ideal conditions, such as flume experiments in the laboratory (Takahashi & Nakagawa, 1993; Fujisawa *et al.*, 2006; Oda *et al.*, 2006). Costa (1988) analyzed examples of past damage statistically and proposed a relationship between the peak outflow discharge from dams and the dam factor (dam factor = dam height \times reservoir volume). However, to date, no experiments have been conducted in mountainous areas to clarify the landslide dam deformation processes.

Many previous studies of river levee failures that resulted from both erosion and infiltration flow have been conducted (Hashimoto *et al.*, 1984; Yoden *et al.*, 2010); these same processes contribute to landslide dam failure. The large-scale models that were constructed showed that failure processes due to erosion were related to the moisture content in the river levee (Hashimoto *et al.*, 1984). However, no model has yet been developed to predict both the infiltration flow and the deformation processes due to erosion under inhomogeneous landslide dam conditions.

To understand both landslide dam deformation processes and outflow discharge from landslide dams that have burst, this study observed the deformation of a small artificial landslide dam in a mountainous area. The results provided by numerical simulation were compared with measurements obtained experimentally and with examples of past damage using a two-dimensional (2-D) numerical model (Takahashi *et al.*, 2002) under conditions in which overtopping eroded the dam.

The numerical model could also be used to analyze changes to the stream bed and to identify and

evaluate factors that affect the outflow processes from landslide dams, as shown in this study.

Finally, the moisture content of the dam, such as that provided by infiltration flow, must be considered in the model of a landslide dam. In this study, a numerical model that incorporates both erosion and infiltration flow processes under saturated and unsaturated conditions was developed based on the theoretical model of Satofuka and Mizuyama (2009) using field observation data. The model proposed in this study successfully predicted the infiltration observed in laboratory flume experiments. Possible improvements to the model are discussed at the end of this chapter.

2.2. Deformation processes based on field observation data

2.2.1. Materials and Methods

Slope failures in narrow channels in mountainous areas can create blockages that form reservoirs. The resulting inundation causes widespread damage in basin areas above the dam. Additionally, when a landslide dam bursts, a large volume of water is released quickly, resulting in disasters such as flash flooding or debris flow in downstream areas. A numerical model to predict both landslide dam deformation and outflow discharge would be useful for developing countermeasures against these hazards.

For the field experiments on landslide dam deformation and outflow, a 5-m-wide landslide dam using sand of uniform particle size on a stream bed was constructed. The gradient of the downstream slope was ~ 6.3 degrees. The stream bed used was free from deposits other than the sand added for the experiment. A schematic diagram of the experimental setup is shown in **Figure 2.5**. **Table 2.1** shows the gradients for the three case studies. The experiment was repeated three times, with two different slope inclines downstream (twice at $1/2$ and once at $1/3$), to allow comparison with previous findings (Takahashi & Kuang, 1988) as well as with slope variation in general.

The soil in the experiment had the following characteristics: an initial water content of 8.23%, a permeability of $1.4 \times 10^{-2} \text{ m s}^{-1}$, and an average particle diameter of 1.5 mm. The landslide dam was constructed under dry conditions using a temporary drainage pipe.

The procedure for collecting the experimental data is given as follows:

1. The inflow discharge into the reservoir q_{in} was continually measured using a temporary overflow barrier ~ 50 m upstream. Additionally, the discharge was calculated using Boss's critical theory (minimum specific energy theory).
2. The outflow discharge q_{out} into the lower basin was calculated at ~ 50 m downstream.
3. The reservoir discharge V was measured continuously using a hydrographic scale installed in the reservoir.

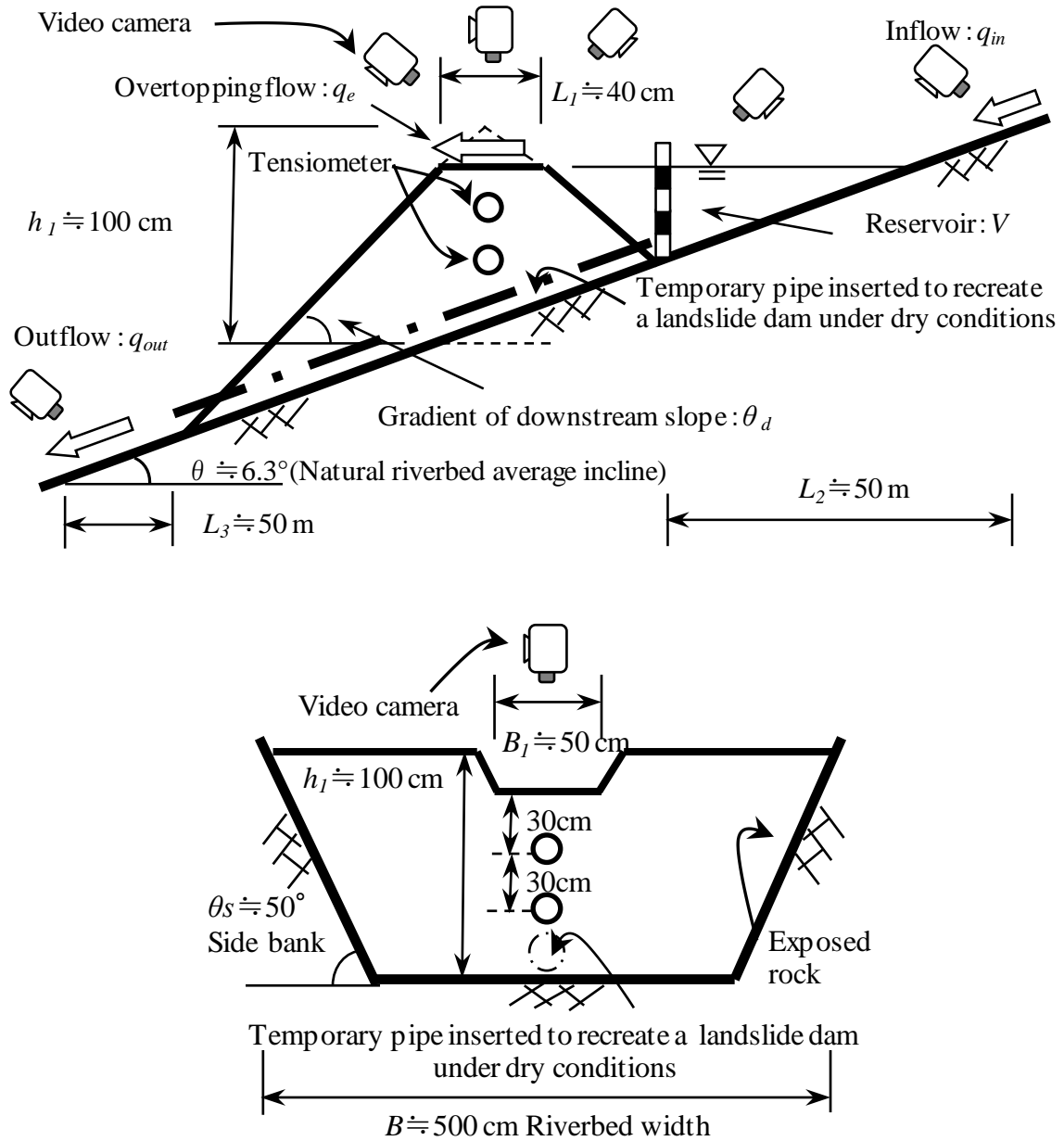


Figure 2.5: Schematic diagram of the field experiment.

Table 2.1: Experimental case study for three different slope inclines.

	Gradient of downstream slope: θ_d
CASE 1-1	26.6 ° (1/2)
CASE 1-2	18.4 ° (1/3)
CASE 1-3	26.6 ° (1/2)

4. Landslide dam failure processes, including deformation, erosion width, and flow discharge q_e were recorded using video cameras.
5. To observe the water content of the landslide dam, two tensiometers were inserted into the landslide dam in CASE 1-2 at depths of 0.3 m and 0.6 m from the top of the landslide dam.

2.2.2. Flood outflow affected by landslide dam deformation processes

The inflow discharge was approximately constant at $\sim 0.016 \text{ m}^3 \text{ s}^{-1}$. The data for landslide dam failure in the three experiments are shown in **Table 2.2**. In the CASE 1-1 experiment, which was performed first, progressive slip failure due to piping in the landslide dam was observed. A pipe was inserted, but it was not possible to completely compact the soil around it. This meant that there were air spaces in the surrounding soil that caused progressive slip failure. Additionally, in both the CASE 1-2 and CASE 1-3 experiments, erosion due to overtopping was observed.

Figure 2.6 shows the experimental results for outflow discharge from the landslide dam (CASES 1-1, 1-2, & 1-3). The collapse of the landslide dam influenced the flood outflow process, namely, the flood hydrograph. CASE 1-3 (gradient of the downstream slope incline: 1/2) had a flow of $\sim 1.59\times$ that of CASE 1-2 (1/3), as shown in **Figure 2.6**. The failure time of CASE 1-3 was $\sim 0.6\times$ that of CASE 1-2. CASE 1-3 (dam failure process: overtopping erosion) had a flow quantity of $\sim 1.25\times$ that of CASE 1-1 (progressive slip failure). These differences reflect differences in flow velocity due to the different slope inclines caused by downslope deformation of the landslide dams.

2.3. Numerical analysis of erosion processes due to overtopping of landslide dams

2.3.1. Governing equations

Table 2.2: Case studies of downstream slope gradient and corresponding dam failure processes.

	Gradient of downstream slope: θ_d	Dam failure process
CASE 1-1	26.6 ° (1/2)	Progressive failure
CASE 1-2	18.4 ° (1/3)	Erosion due to overtopping
CASE 1-3	26.6 ° (1/2)	Erosion due to overtopping

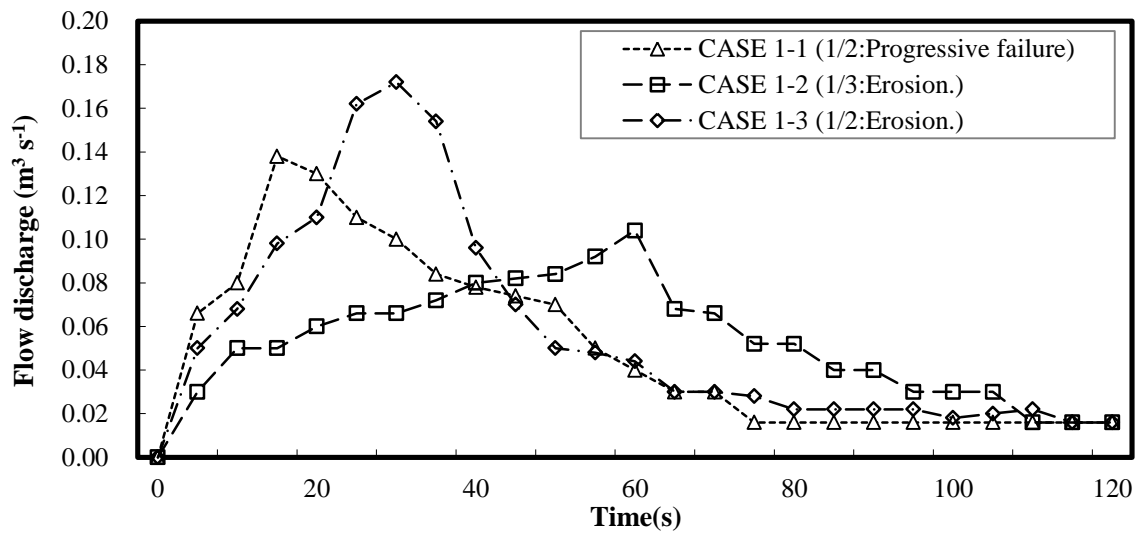


Figure 2.6: Experimental results for outflow discharge from landslide dams as a function of time (CASES 1-1, 1-2, & 1-3).

Generally, the riverbed deformation caused by erosion due to overtopping is affected by 2-D water flow, sediment discharge, and riverbed variation. For landslide dam deformation processes, the water volume, sediment discharge, and deformation changes due to overtopping, are larger than in other processes. In this study, the calculations for the experiments were used in a 2-D simulation model for water depth, depth-averaged velocity, and riverbed variation. Therefore, erosion may also be caused by localized flow. The 2-D simulation model (Takahashi *et al.*, 2002), which predicts both sediment flow and riverbed variations in a non-equilibrium state, was developed based on a previous model (Takahashi & Nakagawa, 1991), which considered both riverbed erosion and deposition caused by sediment flow.

Figure 2.7 shows the relationship used to predict riverbed variation. Sediment discharge in previous models was calculated as follows:

1. The tractive force in the flow is calculated using the riverbed conditions and geographical feature conditions.
2. The sediment discharge at some point is calculated from the tractive force using an equation for the prediction of the equilibrium sediment discharge.
3. Variations in the riverbed conditions are calculated using sediment discharge.

The 2-D simulation model of Takahashi *et al.* (2002) considered the erosion/deposition velocity (Takahashi & Nakagawa, 1991), as follows:

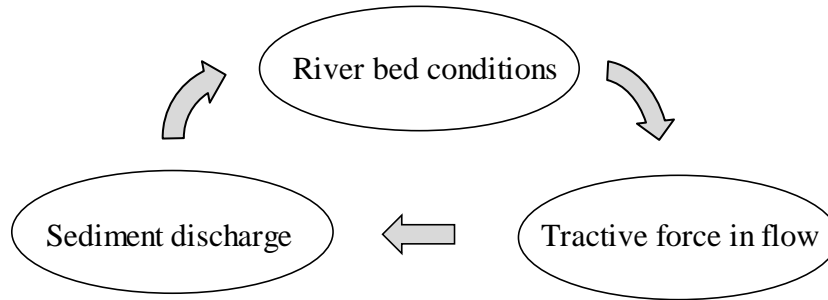


Figure 2.7: Relationship used to predict variations in the riverbed.

1. The sediment concentration of the volume flow is calculated with the tractive force of the flow and compared with the equilibrium sediment concentration obtained by the gradient of the riverbed.
2. The erosion/deposition velocity at a local point is calculated from the difference between the equilibrium sediment concentration of the volume flow and the sediment discharge of the flow at this point.
3. The riverbed variation is calculated using the erosion/deposition velocity.

Erosion and deposition involve nonequilibrium riverbed variations. Previous models that considered equilibrium sediment discharge could not predict the riverbed variations in which fixed and moving riverbeds intermingle continuously. Under these conditions, the calculations for equilibrium sediment discharge must be rectified by geographical features; however, the method for rectification is not clear due to a lack of knowledge. Using the erosion/deposition velocity enables prediction of riverbed variations without rectification.

Ashida and Michiue (1972) proposed a numerical simulation model that considers nonequilibrium sediment discharge in terms of a pick-up rate and step length for bed-load transport. However, it is difficult to apply this model to sediment discharge over extended periods of time due to complications associated with several factors in the calculation. The model proposed by Takahashi *et al.* (2002) provides a means to predict sediment discharge without extended periods of time.

In 2-D space, the sediment flow and momentum equations are given by equations 2.2–2.4 below, where the flow is in the x direction, and the y direction is the transverse direction with respect to the flow:

$$\frac{\partial h}{\partial t} + \frac{\partial uh}{\partial x} + \frac{\partial vh}{\partial y} - i_b = 0, \quad (2.2)$$

$$\frac{\partial u}{\partial t} + u \frac{\partial u}{\partial x} + v \frac{\partial u}{\partial y} = -\frac{1}{\rho} \frac{\partial p}{\partial x} - \frac{\tau_x}{\rho h} + 2 \frac{\partial}{\partial x} \left(\varepsilon \frac{\partial u}{\partial x} \right) + \frac{\partial}{\partial y} \left(\varepsilon \frac{\partial u}{\partial y} \right), \quad \text{and} \quad (2.3)$$

$$\frac{\partial v}{\partial t} + u \frac{\partial v}{\partial x} + v \frac{\partial v}{\partial y} = -\frac{1}{\rho} \frac{\partial p}{\partial y} - \frac{\tau_y}{\rho h} + \frac{\partial}{\partial x} \left(\varepsilon \frac{\partial v}{\partial x} \right) + 2 \frac{\partial}{\partial y} \left(\varepsilon \frac{\partial v}{\partial y} \right), \quad (2.4)$$

where h is the flow depth, u and v are the average velocity components in the x and y directions, respectively, i_b is the erosion/deposition velocity, p is the pressure, ρ is the interstitial fluid density, and ε is the eddy momentum diffusivity.

The riverbed shear stresses in the x and y directions, τ_x and τ_y , are given by equations (2.5) and (2.6), respectively:

$$\frac{\tau_x}{\rho h} = \frac{u}{\sqrt{u^2 + v^2}} \frac{u_*^2}{h}, \quad \text{and} \quad (2.5)$$

$$\frac{\tau_y}{\rho h} = \frac{v}{\sqrt{u^2 + v^2}} \frac{u_*^2}{h}, \quad (2.6)$$

where u_* is the shear velocity, given by

$$u_*^2 = \frac{\sqrt{u^2 + v^2}}{6.0 + 5.75 \log(h/k_s)}, \quad (2.7)$$

and k_s is the equivalent roughness coefficient, which is generally equal to the particle diameter of grit d .

The eddy momentum diffusivity ε is given as:

$$\varepsilon = \frac{\kappa}{6} u_* h, \quad (2.8)$$

where κ is Von Karman's constant.

Assuming that the vertical component of velocity is negligible and that the pressure is hydrostatic, the first clause of the right side of the equation in both equations (2.3) and (2.4) is given by equations (2.9) and (2.10), respectively:

$$-\frac{1}{\rho} \frac{\partial p}{\partial x} = -g \frac{\partial(h+z)}{\partial x}, \quad \text{and} \quad (2.9)$$

$$-\frac{1}{\rho} \frac{\partial p}{\partial y} = -g \frac{\partial(h+z)}{\partial y}, \quad (2.10)$$

where z is the movable bed layer depth, and g is the acceleration due to gravity.

According to Takahashi *et al.* (1997), the erosion/deposition velocity i_k for each particle diameter of grit k is given by the following:

1. Erosion: $C_\infty - C > 0$

$$i_k = \begin{cases} \delta_e \frac{C_\infty - C}{C_*} |u_* - u_{*c}| & (u_* > u_{*c}) \\ 0 & (u_* \leq u_{*c}) \end{cases}, \quad (2.11)$$

2. Deposition: $C_\infty - C \leq 0$

$$i_k = \begin{cases} \delta_d \frac{C_\infty - C}{C_*} |u_* - u_{*c}| & (u_* < u_{*c}) \\ 0 & (u_* \geq u_{*c}) \end{cases}, \quad (2.12)$$

where δ_e is the erosion velocity coefficient, δ_d is the deposition velocity coefficient, C_∞ is the equilibrium sediment concentration of the volume flow, u_* is the friction velocity, C_* is the sediment concentration by volume in the movable bed layer, and C is the sediment concentration of the volume flow at the point.

Using the equilibrium sediment concentration of the volume flow (Ashida & Michiue, 1972), the equilibrium sediment discharge q_b is given as:

$$q_b = 17\sqrt{sgd^3} \tau_*^{3/2} \left(1 - \frac{\tau_{*c}}{\tau_*}\right) \left(1 - \frac{u_{*c}}{u_*}\right), \quad (2.13)$$

where τ_* is the non-dimensional riverbed shear stress in the flow, u_{*c} is the critical friction velocity, g is the acceleration due to gravity, d is the particle diameter of grit, $s = \rho/\sigma - 1$ and σ is the bulk density of grit.

The non-dimensional riverbed shear stress τ_* can be represented as follows:

$$\tau_* = \frac{u_*^2}{sgd}. \quad (2.14)$$

Using the equilibrium sediment discharge q_b obtained using equation (2.13), the equilibrium sediment concentration of the volume flow C_∞ is given by

$$C_\infty = \frac{q_b}{q}. \quad (2.15)$$

The flow discharge (including water and grit) q is given as

$$q = h\sqrt{u^2 + v^2}. \quad (2.16)$$

The continuity equation for the riverbed with the erosion/deposition velocity i_b is as follows:

$$\frac{\partial z}{\partial t} + i_b = 0. \quad (2.17)$$

The continuity equation for the flow is given as

$$\frac{\partial Ch}{\partial t} + \frac{\partial Chu'}{\partial x} + \frac{\partial Chv'}{\partial y} - i_b C_* = 0, \quad (2.18)$$

where u' and v' are the sediment flow velocities in the x -axis and y -axis, respectively, which are affected by the cross slope of the riverbed. Considering the total amount of the sediment discharge, u' and v' can be calculated as follows:

$$u' = \sqrt{u^2 + v^2} \cos(\beta_1 + \beta_2), \quad \text{and} \quad (2.19)$$

$$v' = \sqrt{u^2 + v^2} \sin(\beta_1 + \beta_2). \quad (2.20)$$

As shown in **Figure 2.8**, the angle β_1 between the flow direction (s -axis) and x -axis is as follows:

$$\beta_1 = \arctan\left(\frac{v}{u}\right). \quad (2.21)$$

The angle β_2 between the sediment flow direction and s -axis is as follows:

$$\beta_2 = \arctan\left(\frac{q_{bn}}{q_{bs}}\right), \quad (2.22)$$

where q_{bs} is the sediment discharge in the flow direction, and q_{bn} is the sediment discharge in the perpendicular direction of the flow.

According to Hasegawa (1986), the sediment discharge for the n -direction flow q_{bn} is as follows:

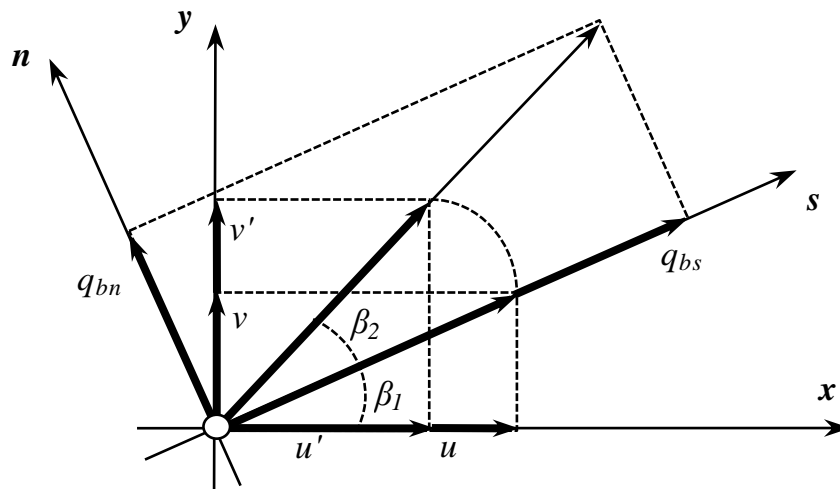


Figure 2.8: Relationship between the flow velocity and sediment flow.

$$q_{bn} = q_{bs} \left(\frac{h}{r} N_* + \sqrt{\frac{\tau_{*c}}{\mu_s \mu_k \tau_*} \frac{\partial z}{\partial n}} \right), \quad (2.23)$$

where r is the radius of curvature of the flow, and N_* , μ_s , and μ_k are coefficients.

The radius of curvature of the flow r is given by Shimizu and Itakura (1991):

$$\frac{1}{r} = \frac{1}{(u^2 + v^2)^{3/2}} \left\{ u \left(u \frac{\partial v}{\partial x} - v \frac{\partial u}{\partial x} \right) + v \left(u \frac{\partial v}{\partial y} - v \frac{\partial u}{\partial y} \right) \right\}. \quad (2.24)$$

Generally, the shear force causes side-shore erosion on the outside of a curve. Equations (2.19–2.24) consider the characteristic of the cross slope of the riverbed. However, when the riverbed variation is affected by rapid changes in the local flow, the erosion velocity is required to consider the effect of the local slope change in the riverbed.

Considering the effect of the local slope change in the riverbed with erosion velocity i_b^j on the riverbed z_j , as shown in **Figure 2.9**, erosion velocity i^j considering the side-shore is as follows:

$$i^j = i_b^j + \frac{\Delta z}{\Delta y} i_s^j, \quad (2.25)$$

where Δz is the difference in adjoined riverbed heights, i_s^j is the side-shore erosion velocity, and Δy is the distance between these calculating points as shown in **Figure 2.9**. The side-shore erosion in four directions was considered, as well as the direction of up-and-down flow and the horizontal direction.

Considering the non-dimensional riverbed shear stress τ_{*s} , the side-shore erosion velocity i_s is given by equation (2.26) (Ashida *et al.*, 1983):

$$i_s = a_1 \tau_{*s} \left(1 - a_2 \frac{\tau_{*c}}{\tau_{*s}} \right), \quad (2.26)$$

$$a_1 = 0.01 \sqrt{sgd}, \quad (2.27)$$

$$s = \sigma / \rho - 1, \text{ and} \quad (2.28)$$

$$a_2 = 2 \sqrt{\frac{1 - (1/\tan \theta)^2 (\partial z / \partial n)^2}{1 + (\partial z / \partial n)^2}}. \quad (2.29)$$

Assuming that the shear velocity u_{*s} of the side-shore is proportional to the bed-load velocity U_L , the non-dimensional shear stress τ_{*s} of the side-shore can be expressed as

$$u_{*s} = a_3 U_L, \text{ and} \quad (2.30)$$

$$\tau_{*s} = \frac{u_{*s}^2}{(\sigma / \rho - 1)gd} = \frac{a_3^2 U_L^2}{(\sigma / \rho - 1)gd}, \quad (2.31)$$

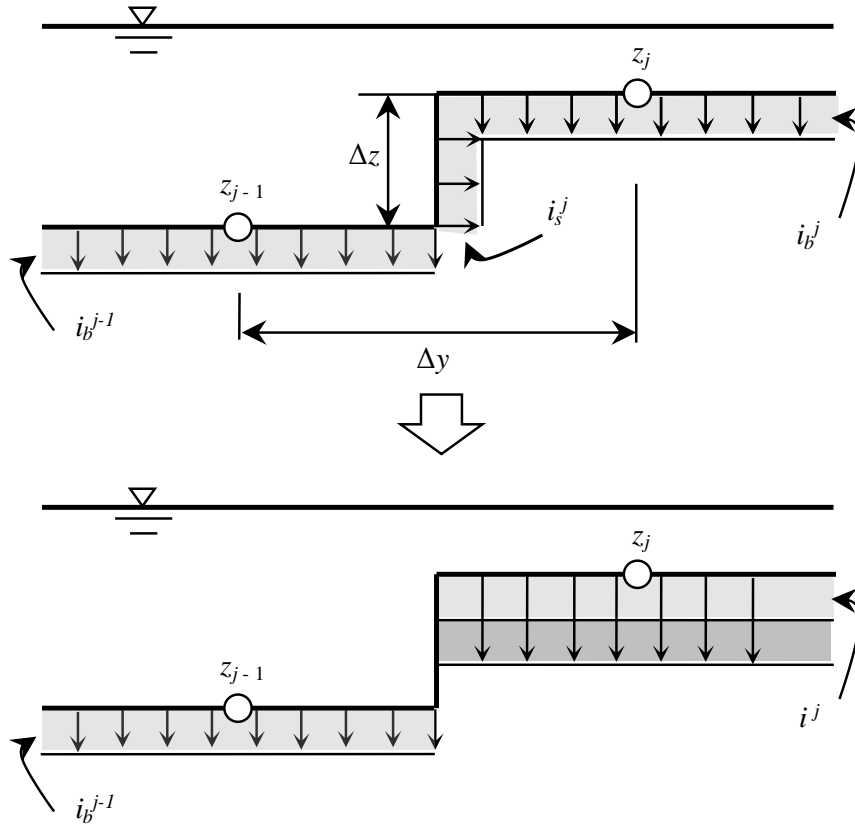


Figure 2.9: Schematic diagram of side-shore erosion.

where θ is the gradient of the riverbed, and a_3 is a coefficient.

Using both the horizontal flow velocity U and the vertical flow velocity V , the bed-load velocity U_L is given as follows:

$$U = \sqrt{u^2 + v^2}, \quad (2.32)$$

$$V = -\frac{h}{r} N_* U, \text{ and} \quad (2.33)$$

$$U_L = \sqrt{U^2 + V^2} = \sqrt{1 + \frac{h^2}{r^2} N_*^2} \sqrt{u^2 + v^2}. \quad (2.34)$$

In future research, the proposed model described above will also consider the combined effect of both steep slopes and vertical flow.

2.3.2. Calculation conditions

Both the landslide dam failure processes and outflow discharge due to overtopping in CASE 1-3 were

calculated using the numerical model (Takahashi *et al.*, 2002). These calculations were based on the same conditions as those used in the field experiments.

Table 2.3 shows the parameters used in the calculations. The particle diameter and internal frictional angle were determined using experimental results; the other parameters were determined by referring to Takahashi *et al.* (2002).

2.3.3. Comparison of the observed data with the calculated results

Figure 2.10 shows the simulation results of erosion-induced deformation processes of a landslide dam. Both stream-bed and side-shore erosion were indicated. I estimated a hydrograph to show the flood outflow process from the landslide dam using the numerical model results. Additionally, **Photograph 2.1**, taken with a video camera, shows a picture of the deformation for comparison with the calculated results obtained from numerical simulations.

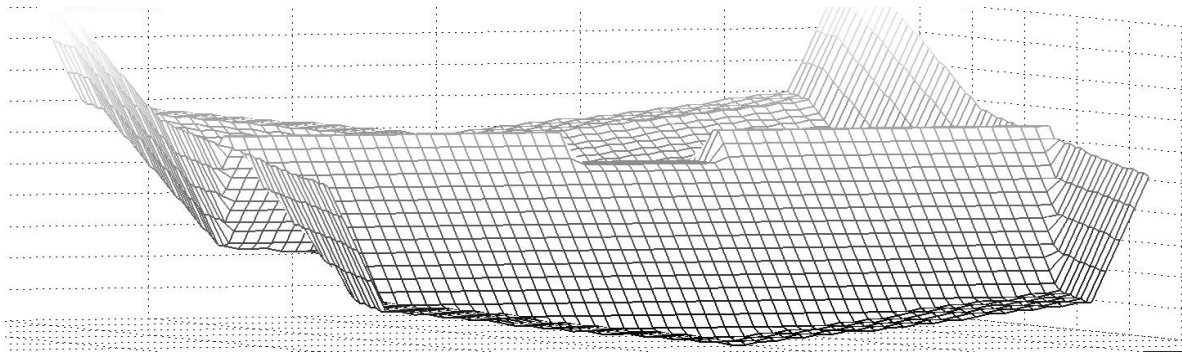
Figure 2.11 shows a comparison of hydrographs from observed and calculated data for the landslide dam. The calculated results were mostly consistent with experimental data and observations.

Table 2.3: Parameters used in the calculation for CASE (1-3).

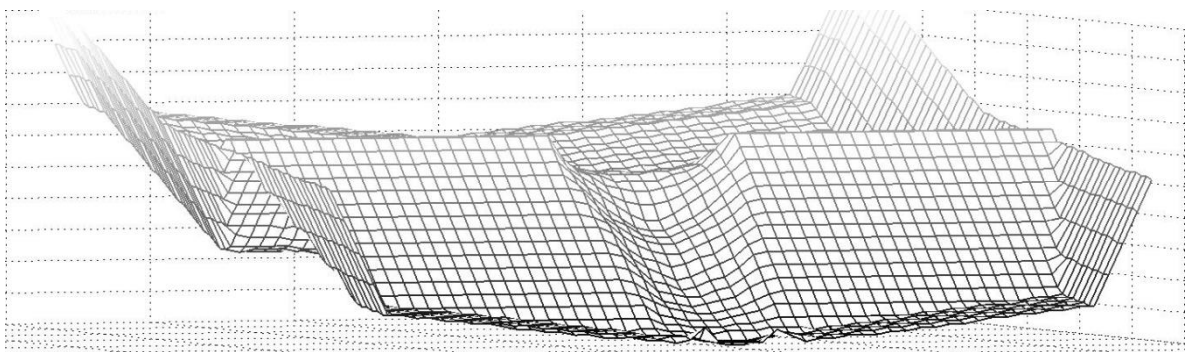
d (mm)	ϕ (°)	Δx (cm)	Δy (cm)	Δt (s)	n_m (m ^{-1/3} s)
1.5	37	10	10	0.001	0.05



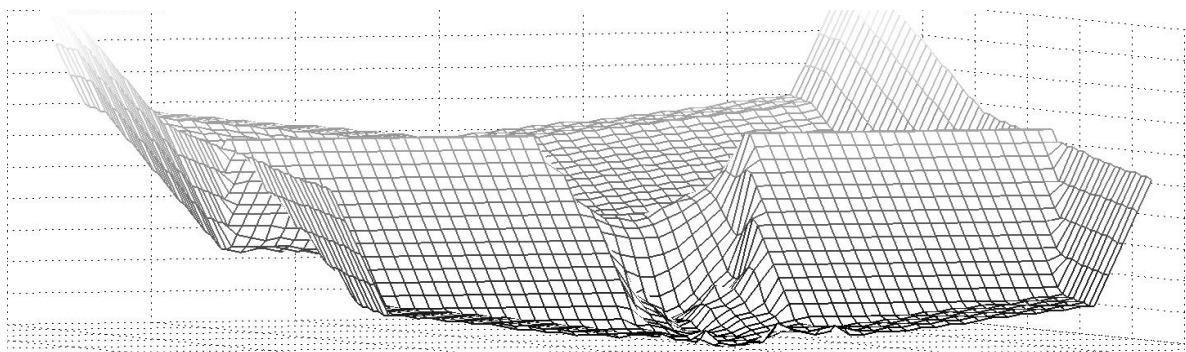
Photograph 2.1: Observed results (landslide dam deformation for CASE 1-3).



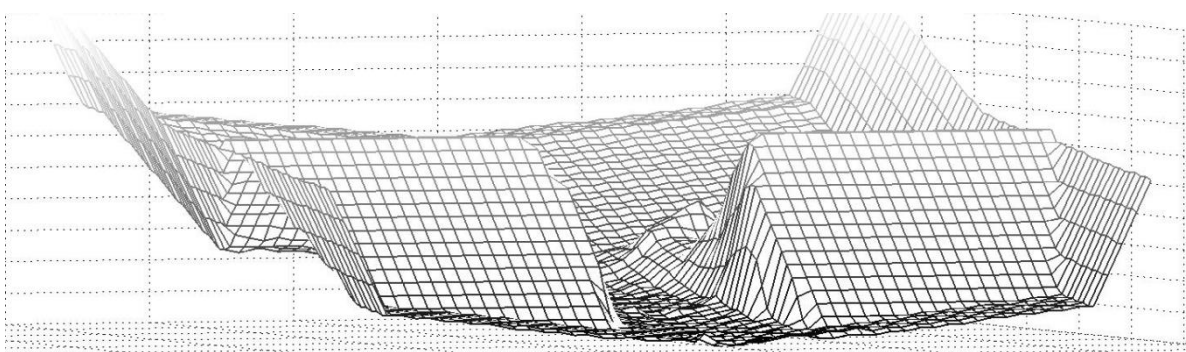
$t = 0$ s: before start.



$t = 10$ s: at the time of the erosion start.



$t = 30$ s: at the time of maximum flow.



$t = 60$ s: at the time of the end of vertical erosion.

Figure 2.10: Analysis results (landslide dam deformation processes for CASE 1-3).

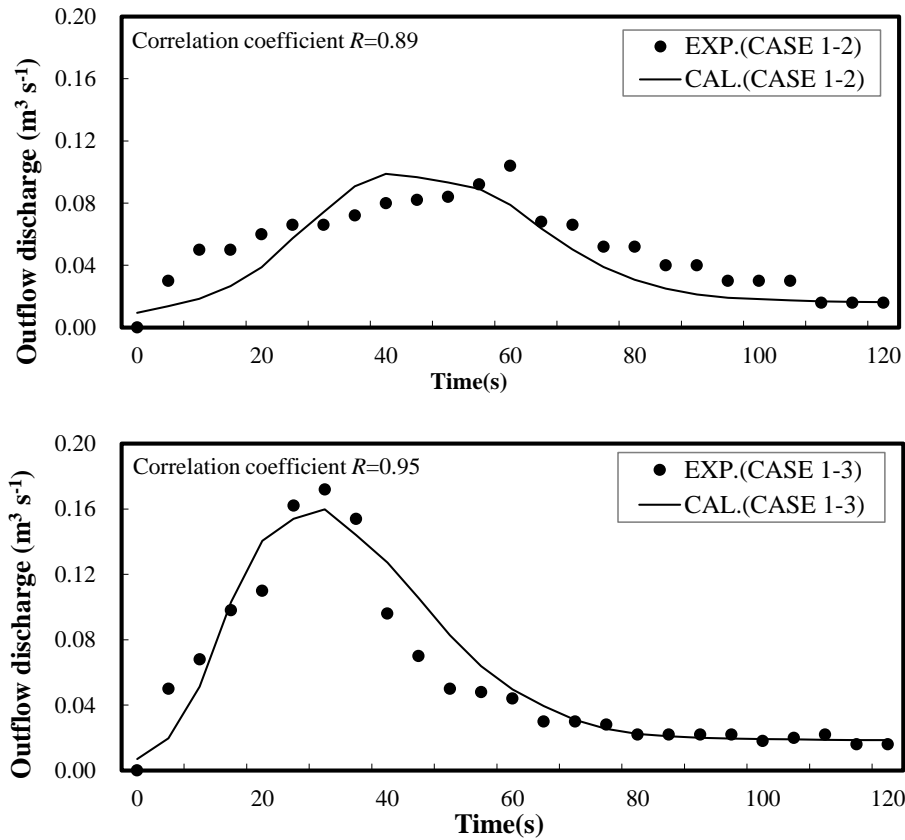


Figure 2.11: Comparison between the calculated and observed outflow discharge results for CASES 1-2 and 1-3.

Table 2.4: Analysis cases for the real-life scale simulations.

	Dam height (m)	Dam volume (m ³)
CASE 2-1	5.8	7,400
CASE 2-2	18.0	910,000
CASE 2-3	5.8	42,600
CASE 2-4	5.8	96,000

2.4. Factors that affect the flood outflow in real life

2.4.1. Applicability to real-life scales using the numerical model

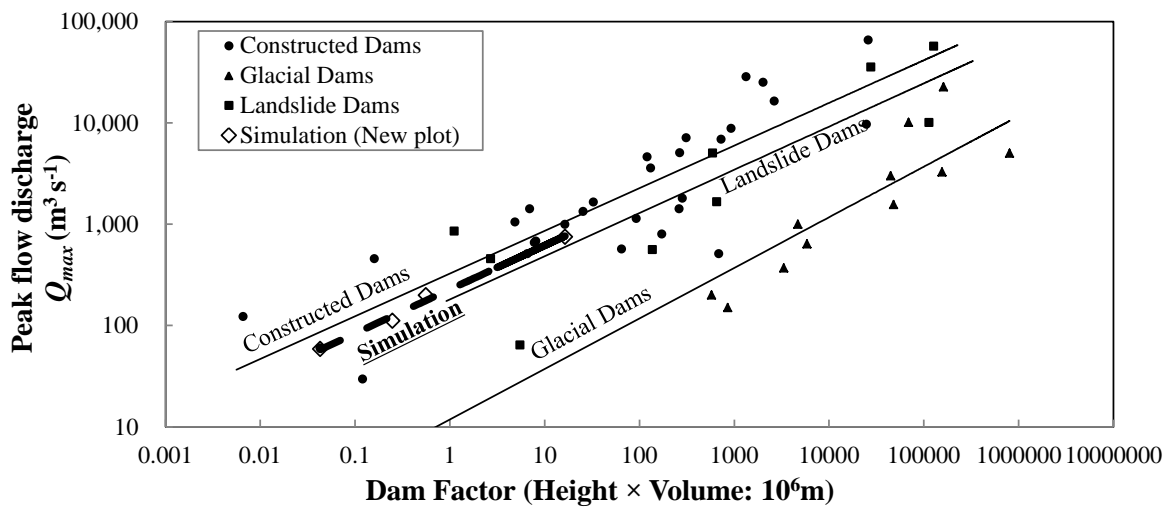
To verify the applicability of the model to real-life scales, this study used a numerical model (Takahashi *et al.*, 2002) to analyze the same conditions as in past examples (CASES 2-1 & 2-2: Coast, 1988), as shown in **Table 2.4**. **Tables 2.5** and **2.6** show the parameters used in the calculation, which refer to Coast (1988).

Table 2.5: Parameters used in the calculation.

d (cm)	ϕ ($^{\circ}$)	Δx (m)	Δy (m)	Δt (s)	n_m ($\text{m}^{-1/3} \text{s}$)	ρ (kg m^{-3})
5	30	5	5	0.01	0.05	1.1

Table 2.6: Parameters used in the calculation.

Average stream-bed slope	Angle in the up-and-down slopes of the dam
1/200	1/3.0 (up, down)

**Figure 2.12:** Relationship between the peak outflow discharge and the dam factor according to Coast, 1988.

To validate the model's applicability at real-life scales, this study plotted the calculated relationship between the peak outflow discharge and the dam factor (Coast, 1988). The comparison shows that the numerical simulation model can be used effectively at real-life scales (landslide dams), as shown in **Figure 2.12**.

2.4.2. Factors that affect flood outflow processes

Generally, flood flow processes are affected by the volume of water in the reservoir, the dam height, and the gradient of the downstream slope (Takahashi & Nakagawa, 1993; Coast, 1988). However, these causes were not clear.

To understand the factors that affect flood outflow processes from a reservoir at real-life scales, this study calculated the change in the outflow discharge, varying the following conditions: the volume of water in the reservoir, the dam height, and the gradient of the slope upstream and downstream of the dam, as shown in **Table 2.7**.

This study examined various flood outflow processes for 13 different cases (CASES 3.1–3.13) as a function of dam height, dam volume, and slope gradient. **Figure 2.13** shows CASES 3.1–3.3 in which the dam height remained constant, but the reservoir water volume was varied. The ratio of the peak-outflow discharge to the volume of water in the reservoir was largely the same in all cases. The results suggest that the volume of water in the reservoir greatly affected the flood outflow processes.

This study also analyzed cases in which the volume of water in the reservoir was constant, but the dam heights differed (CASES 3.4–3.6 in **Table 2.7**, as shown in **Figure 2.14**). Unlike previous studies (Coast, 1988), dam height did not affect flood outflow processes. This will be explained in the discussion that follows. The outflow discharge Q from the landslide dam, shown schematically in **Figure 2.15**, is given by Honma (1940) as follows:

$$Q = CBh^{3/2}, \quad (2.35)$$

$$m_1 = 0 \sim 4/3, \quad m_2 \geq 5/3 \quad C = 1.37 + 1.02 (h/W), \quad (2.36)$$

$$m_1 = 0 \sim 2/3, \quad m_2 \doteq 1/1 \quad C = 1.28 + 1.42 (h/W), \quad (2.37)$$

$$m_1 = 0 \sim 1/3, \quad m_2 \doteq 2/3 \quad C = 1.24 + 1.64 (h/W), \text{ and} \quad (2.38)$$

$$m_1 = m_2 = 0, \quad h/L < 1/2 \quad C = 1.55, \quad (2.39)$$

Table 2.7: Analysis cases for the factors that affect the flood outflow processes.

	Dam-height (m)	Dam-volume (m ³)	Gradient of slope	
			Up (u)	Down (d)
CASE 3-1	6.0	2,600	1/2.5	1/2.5
CASE 3-2		5,200		
CASE 3-3		7,800		
CASE 3-4	2.0	2,600	1/2.5	1/2.5
CASE 3-5	4.0			
CASE 3-6	6.0			
CASE 3-7	6.0	7,800	1/2.0	1/2.0
CASE 3-8			1/2.5	1/2.5
CASE 3-9			1/3.0	1/3.0
CASE 3-10			1/2.5	1/2.0
CASE 3-11			1/2.5	1/3.0
CASE 3-12			1/2.0	1/2.5
CASE 3-13			1/3.0	1/2.5

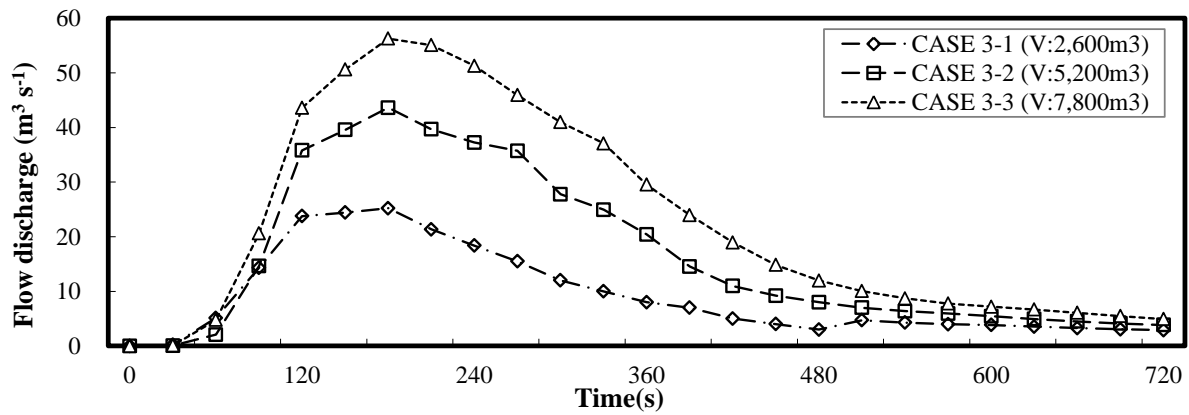


Figure 2.13: Flow discharge over time at three different reservoir water volumes, with a fixed dam height and slope gradient.

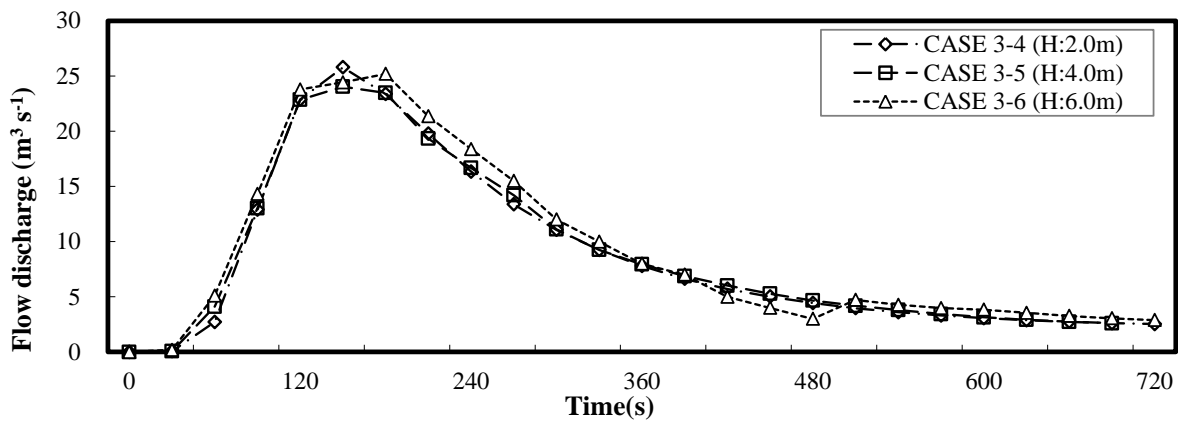


Figure 2.14: Flow discharge over time at differing dam heights, with a fixed dam volume and slope gradient.

where B is the crossing width of the dam, h is the flow depth due to overtopping, m_1 is the gradient of the upstream slope, m_2 is the gradient of the downstream slope, C is a coefficient for the flow, W is the height of the dam, and L is the length of the dam. The difference between the water level of the reservoir and the top of the dam affects strongly the outflow discharge (**Figure 2.15**): namely, the overflow depth, not the dam height. Coast (1988) proposed a statistical theory for dams based only on past examples. However, it is natural that dams containing a large volume of water tend to be high; thus, the theory should be modified. In the future, examples with differing dam heights, but similar reservoir volumes, should be compared. Additionally, for this study, cases with different slopes upstream and downstream from the dam were analyzed, holding the other variables constant (CASES 3.7–3.13 in **Table 2.7**, as shown in **Figure 2.16**). Steep slopes (both upstream and downstream) affected the peak outflow processes; however, previous studies reported only that a steep slope of the downstream affected the peak outflow processes.

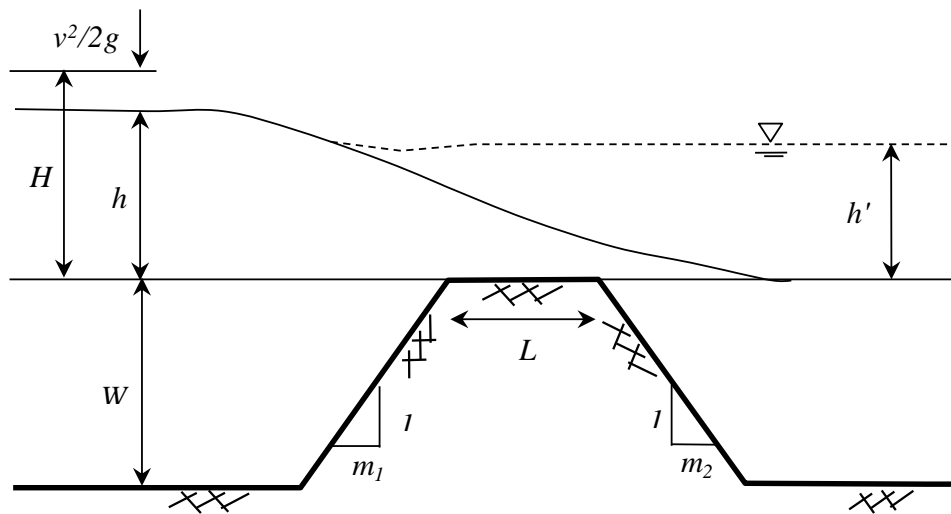


Figure 2.15: Schematic diagram of the outflow due to overtopping of the dam (Honma, 1940).

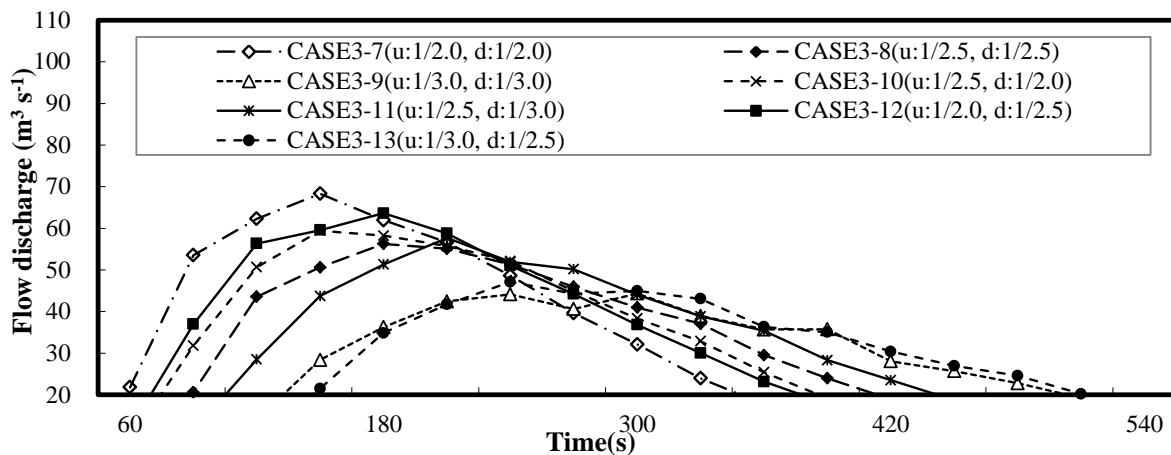


Figure 2.16: Flow discharge over time in cases with different upstream and downstream slopes, with a fixed dam height and reservoir volume.

2.5. Numerical analysis of landslide dam failure considering infiltration flow

2.5.1. Basic equations for erosion and infiltration

The numerical model of Satofuka and Mizuyama (2009) simultaneously predicts infiltration flow under both unsaturated and saturated conditions and erosion due to overtopping, which includes outflow over the landslide dam. This model also considers the quantity of water flowing on the

riverbed surface and through the deposited layers. To calculate water quantity, this study calculated the difference between the water pressure acting on the riverbed surface and the internal pressure of the deposit. To predict erosion and infiltration flow simultaneously, the flow fluxes were solved using a difference method, specifically, the backward difference method.

The 2-D vertical field is a constant frame of reference determined by the gravitational field. It can be used to predict infiltration outflow more easily than can be done in three dimensions. The field study results for this study indicate that the amount of vertical erosion was greater than that of transverse erosion, as shown in **Figure 2.10**. The model used to describe infiltration flow under unsaturated conditions was based on previous studies that predicted the sedimentation of bed loads on riverbeds (Ogasawara *et al.*, 2005). The x -axis is parallel to the river bank, and the z -axis is perpendicular to the x -axis, as shown in **Figure 2.17**.

The relationship between the volumetric water content θ and pressure head ψ is given by Richard's equation:

$$\left(\frac{\partial \theta}{\partial \psi} + \beta S_s \right) \frac{\partial \psi}{\partial t} = \frac{\partial}{\partial x} \left\{ K \left(\frac{\partial \psi}{\partial x} - \sin \alpha \right) \right\} + \frac{\partial}{\partial z} \left\{ K \left(\frac{\partial \psi}{\partial z} + \cos \alpha \right) \right\}, \quad (2.40)$$

where K is the coefficient of permeability, t is time, S_s is the storage ratio coefficient, z is the depth of the deposit layer, α is the gradient of the riverbed, and β is the coefficient describing soil saturation. When the soil is saturated, $\beta = 1$, whereas when the soil is unsaturated, $\beta = 0$.

Tani (1982) reported the relationship between the water content θ and pressure head ψ . The relationship between the coefficient of permeability in unsaturated soil K and water content θ is as follows:

$$\theta = (\theta_s - \theta_r) \left(\frac{\psi}{\psi_0} + 1 \right) \exp \left(-\frac{\psi}{\psi_0} \right) + \theta_r, \quad (2.41)$$

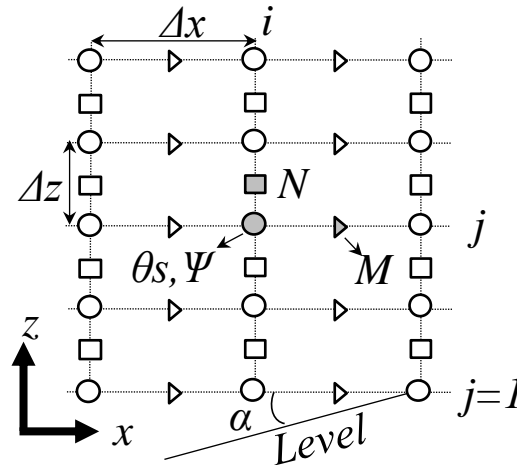


Figure 2.17: Discretization of variables in the simulation.

$$K = K_s \left\{ \frac{\theta - \theta_r}{\theta_s - \theta_r} \right\}^m, \quad (2.42)$$

where θ_s is the saturated volumetric water content, θ_r is the residual volumetric water content, ψ_0 is the pressure head at the inflection point of the characteristic moisture curve, K_s is the saturated hydraulic conductivity, and m is a coefficient for infiltration flow.

To calculate both infiltration flow and pressure head, equation (2.40) can be rewritten as follows:

$$\left(\frac{\partial \theta}{\partial \psi} + \beta S_s \right) \frac{\partial M}{\partial t} = - \left(\frac{\partial M}{\partial x} + \frac{\partial N}{\partial z} \right), \quad (2.43)$$

$$M = -K \left(\frac{\partial \psi}{\partial x} - \sin \alpha \right), \quad \text{and} \quad (2.44)$$

$$N = -K \left(\frac{\partial \psi}{\partial z} + \cos \alpha \right), \quad (2.45)$$

where M is the flow flux along the x -axis, and N is the flow flux along the z -axis, as shown in **Figure 2.17**. Each flux is obtained by both the pressure head ψ and the coefficient of permeability K using equations (2.44) and (2.45). Additionally, the coefficient of permeability K is obtained using equation (2.42); thus, the time interval needs to be short.

Under unsaturated conditions ($\beta = 0$), using equation (2.43), the relationship between the pressure head ψ and water content θ of the deposit is described as follows:

$$\frac{\partial \theta}{\partial t} = - \left(\frac{\partial M}{\partial x} + \frac{\partial N}{\partial z} \right). \quad (2.46)$$

Equation (2.46) shows that the water content is changed by infiltration flow.

The relationship between the water content and pressure head (negative pressure) is determined by the soil-water characteristic curves. Using equations (2.41-2.46), the fluxes M and N can be used to obtain the water content θ and head pressure ψ . However, the inverse function is needed to calculate the water content θ and pressure head ψ using equation (2.41).

In the saturated deposit (namely, $\theta = \theta_s$ and $\beta = 1$), equation (2.43) is rewritten as follows:

$$S_s \frac{\partial \psi}{\partial t} = - \left(\frac{\partial M}{\partial x} + \frac{\partial N}{\partial z} \right). \quad (2.47)$$

Equation (2.47) shows that the infiltration flow under saturated conditions affects the pressure head (positive pressure) directly.

The exchange flux between the deposition and flow layers is determined by the pressure gradient,

which is evaluated using the water pressure acting on the riverbed surface and the pressure head under the surface of the deposit layer. Consideration of the changes in the deposit layer depth is necessary to calculate the exchange flux. The deposit layers were divided into segments of equal thickness, as shown in **Figure 2.18**.

The riverbed variation takes place in the highest segment ($0 < \Delta z' \leq \Delta z$) of the deposit layer. In contrast, the flow layers are not divided.

As shown in **Figure 2.19** (left side), in $\Delta z/2 < \Delta z' \leq \Delta z$, the exchange flux w_i between the deposit and flow layers at point i is determined by the pressure head of the inside deposit layers (closest to the surface), as described by the following equation:

$$w_i = -K \left\{ \frac{h_i \cos \alpha - \psi_{i,jb-1}}{\Delta z' - \Delta z/2} + \cos \alpha \right\}, \quad (2.48)$$

assuming that the length between the riverbed surface and the calculation point $\psi_{i,jb-1}$ is obtained using $\Delta z' - \Delta z/2$, where h_i is the flow depth.

From $0 < \Delta z' \leq \Delta z/2$ in **Figure 2.19** (right side), the exchange flux w_i between the deposit and flow layers is determined by the pressure head of the inside deposit layers (closest to the surface), which is represented by

$$w_i = -K \left\{ \frac{h_i \cos \alpha - \psi_{i,jb-1}}{\Delta z' + \Delta z/2} + \cos \alpha \right\}, \quad (2.49)$$

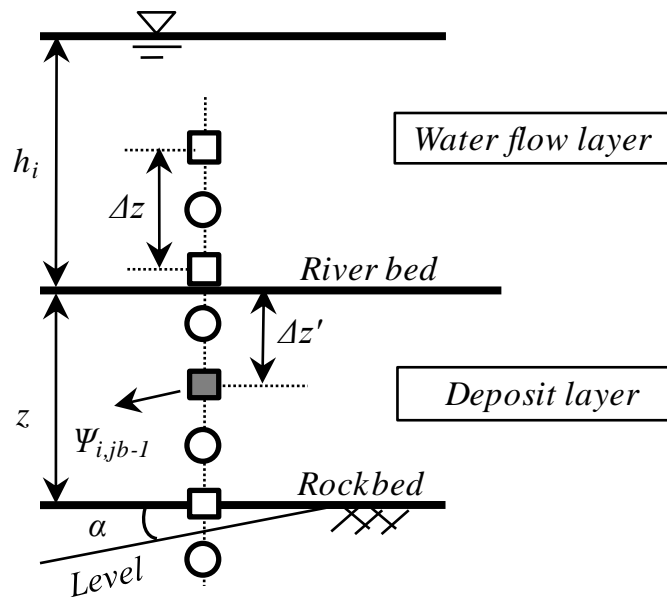


Figure 2.18: Schematic diagram of the model used for the exchange flux calculation around a riverbed.

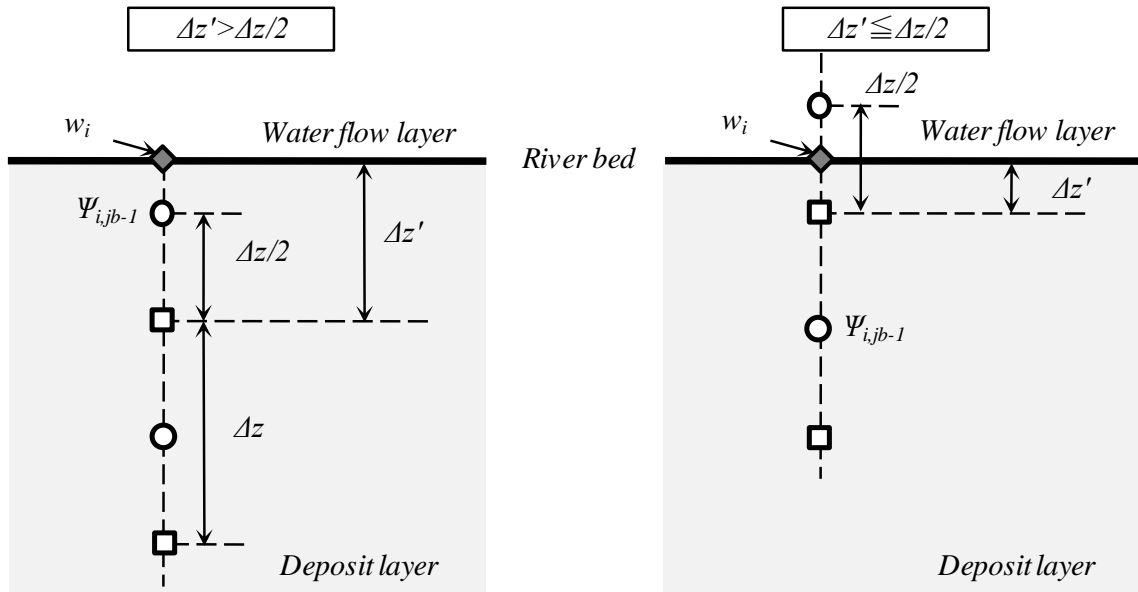


Figure 2.19: Relationship among variables used for the exchange flux calculation near the riverbed surface.

where w_i is used to calculate the infiltration of the deposit.

The equations for momentum, continuity, riverbed variation, erosion/deposition velocity, and riverbed shear stress were based on Takahashi and Nakagawa (1991), as were the staggered scheme and arrangement of variables. Only one particle size was considered.

The continuity equation for the total volume of the debris flow is as follows:

$$\frac{\partial h}{\partial t} + \frac{\partial uh}{\partial x} = w_i + \left\{ C_* + (1 - C_*) \frac{\theta}{\theta_s} \right\}, \quad (2.50)$$

where h is the flow depth, t is time, u is the flow velocity in the x -axis direction, and C_* is the sediment concentration by volume in the movable bed layer.

The continuity equation for the debris flow is as follows:

$$\frac{\partial Ch}{\partial t} + \frac{\partial Chu}{\partial x} = i_b C_* , \quad (2.51)$$

where C is the sediment concentration of the volume debris flow, and i_b is the erosion/deposition velocity.

The flow along the x -axis is described by the momentum equation:

$$\frac{\partial u}{\partial t} + u \frac{\partial u}{\partial x} + \frac{uw_i}{h} = g \sin \alpha - \frac{\partial(z+h)}{\partial x} g \cos \alpha - \frac{\tau_b}{\rho h}, \quad (2.52)$$

where g is the acceleration due to gravity, τ_b is the riverbed shear stress in the x -axis direction, α is the incline of the riverbed, and ρ is the interstitial fluid density. Additionally, the third calculation clause on the left side of equation (2.52) shows the difference in the water momentum caused by the

exchange flux between the deposit and flow layers.

The riverbed shear stress τ_b is given as follows:

1. Stone debris flow: $C \geq 0.4C_*$

$$\frac{\tau_b}{\rho h} = \frac{d^2 u |u|}{8h^3 \{C + (1-C)\rho/\sigma\} \left\{ (C_*/C)^{1/3} - 1 \right\}^2}, \quad (2.53)$$

2. Immature debris flow: $0.01 < C < 0.4C_*$

$$\frac{\tau_b}{\rho h} = \frac{1}{0.49} \frac{d^2}{h^3} u |u|, \quad (2.54)$$

3. Bed load transport: $h/d \geq 30$, or $C \leq 0.01$

$$\frac{\tau_b}{\rho h} = \frac{g n_m^2 u |u|}{h^{4/3}}, \quad (2.55)$$

where ρ is the interstitial fluid density, d is the particle diameter of the grit, and n_m is Manning's roughness coefficient.

The erosion/deposition velocity i_b is given as follows:

1. Erosion: $C < C_\infty$

$$i_b = \delta_e \frac{C_\infty - C}{C_* - C_\infty} \frac{q}{d}, \quad (2.56)$$

2. Deposition: $C \geq C_\infty$

$$i_b = \delta_d \frac{C_\infty - C}{C_*} \frac{q}{h}, \quad (2.57)$$

where C_∞ is the equilibrium sediment concentration, q is the unit width flow discharge, δ_e is the coefficient of erosion, and δ_d is the coefficient of deposition. The equilibrium sediment concentration is as follows:

$$C_\infty = \frac{\rho \tan \theta_w}{(\sigma - \rho)(\tan \phi - \tan \theta_w)}, \quad (2.58)$$

where θ_w is the water-surface gradient, and ϕ is the internal frictional angle of grit.

The processes of debris flow generation and development are calculated with the staggered scheme.

2.5.2. Verification of the numerical model through laboratory experiments

This study compared the calculated results to experiments that were conducted under ideal conditions in a laboratory flume. Using the numerical model developed from existing models and the field model data allowed us to obtain results (infiltration flows) that could not be achieved in previous studies (*i.e.*, Satofuka & Mizuyama, 2009). To verify this approach under ideal conditions, this study used a dam composed of anthracite, which has a homogeneous coefficient of permeability.

Figure 2.20 shows the experimental apparatus. The flume waterway was filled with anthracite and inclined at a fixed angle of 6 degrees. The structure was 10 cm in height and width and 300 cm in length. This study observed the water discharge resulting from supply to the upper end at a rate of $5.3 \text{ cm}^3 \text{ s}^{-1}$, using a collection beaker at the downstream end.

Experiments were conducted for two cases. In one case (CASE 4-2) an obstacle was present, and in the other it was removed (CASE 4-1). The obstacle was 3 cm in height, 10 cm in width, and 20 cm in length. It was made using nonpermeable materials and was installed at the center of the waterway. To observe infiltration, glass was used as the side wall of the waterway. The permeability coefficient of anthracite is 10.0 cm s^{-1} . **Figure 2.21** shows the experimental relationship between soil moisture content and pressure head for anthracite. The results were obtained by pF (potential free energy) testing.

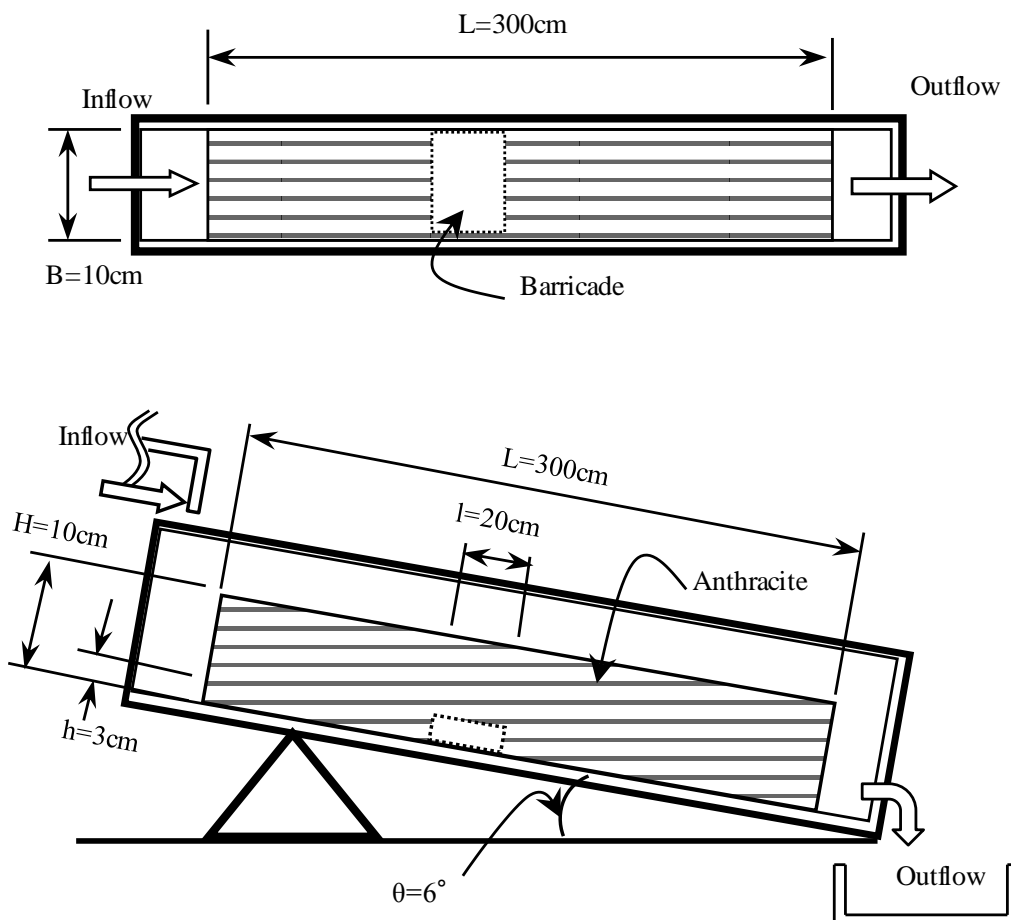


Figure 2.20: Schematic diagram of the experimental waterway flume.

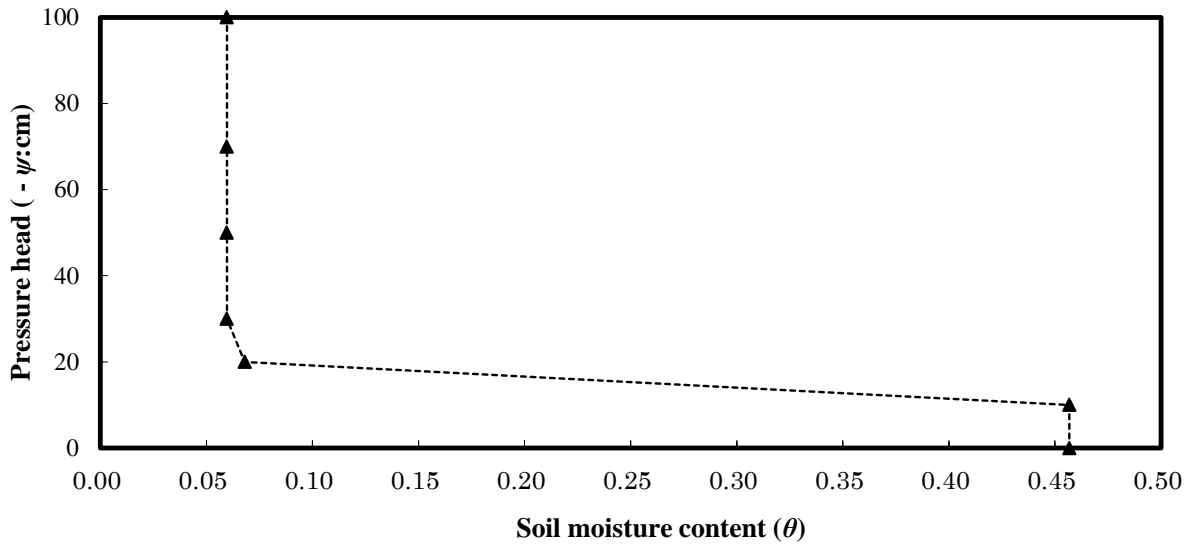


Figure 2.21: Relationship between soil moisture content and pressure head for anthracite.

Table 2.8: Parameters used in the calculation, obtained from experimental values.

θ_s	θ_r	ψ_0 (m)	K_s (cm s ⁻¹)
0.46	0.06	-0.15	10.0

Table 2.9: Parameters used in the calculation, taken from a previous study.

m	S_s	Δx (cm)	Δz (cm)	Δt (s)
6	1	10.0	0.5	0.0002

Using this numerical model, this study calculated the infiltration processes based on the same conditions as those used in the experiment. **Tables 2.8** and **2.9** show the parameters used in the calculation. The parameters in **Table 2.8** were obtained from experimental values, and those in **Table 2.9** were taken from a previous study (*e.g.*, Satofuka & Mizuyama, 2009).

Figure 2.22 shows a comparison between the laboratory observations and theoretical results for the infiltration processes. Additionally, **Figure 2.23** shows the results for the filtration flux around an obstacle after 25 min for CASE 4-2. **Figure 2.22** shows good agreement between the observed data and calculated results; the average correlation coefficient R is 0.92 (range 0.85 – 0.96). However, the assumed parameters (*i.e.*, S_s : the storage ratio coefficient) remain an issue for future research because differences between them affected the predicted infiltration flow.

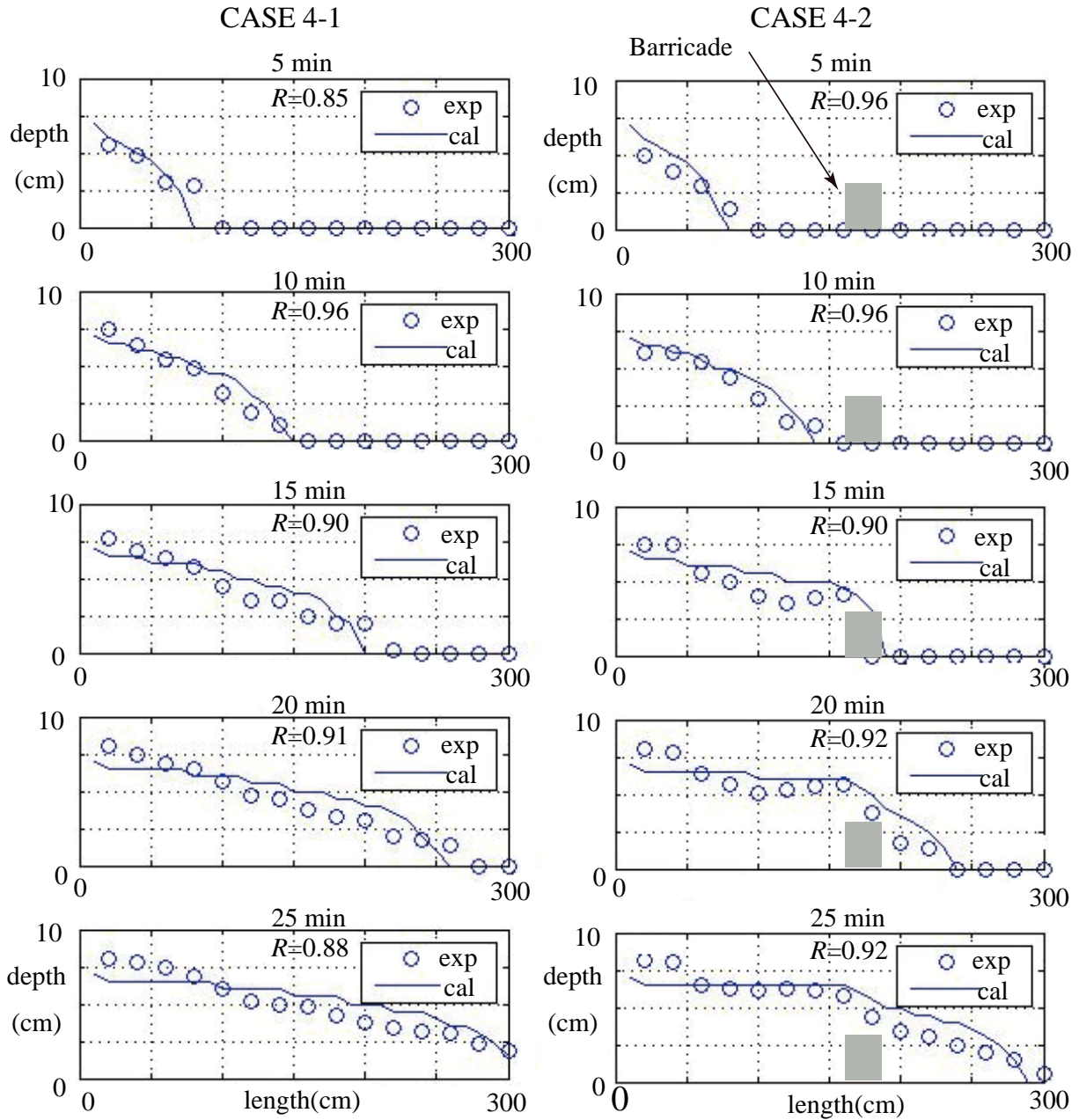


Figure 2.22: Analysis and observation results (water level under soil for CASES 4-1 & 4-2).

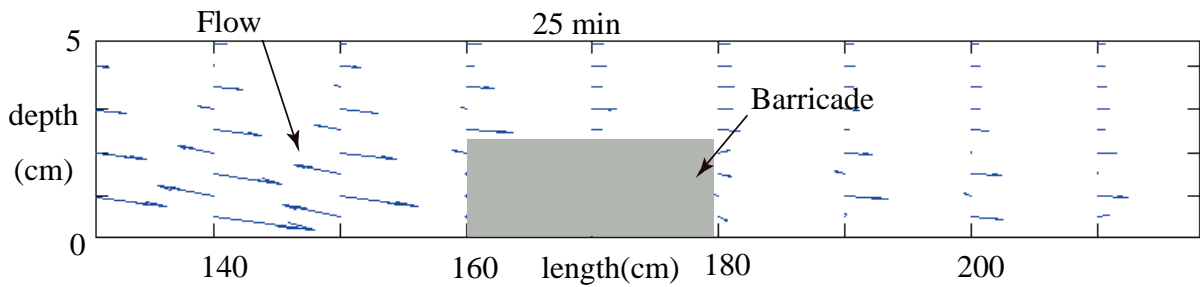


Figure 2.23: Analysis results for infiltration flux around the obstacle in CASE 4-2 ($t = 25$ min).

2.5.3. Calculation conditions

The landslide dam failure processes for both infiltration flow under unsaturated conditions and erosion due to overtopping in CASE 1-2 were calculated using the numerical model. Comparison of the observed with the calculated data confirms the validity of the model.

For this study, the numerical model proposed was used to calculate the infiltration processes based on the same conditions as those used in the field experiments. **Tables 2.10** and **2.11** show the parameters used in the calculation. The parameters listed in **Table 2.10** were obtained from experimental values. The parameters listed in **Table 2.11** are from a previous study (*e.g.*, Satofuka & Mizuyama, 2009). Additionally, this study considered water transfer between the deposit and water layers, *i.e.*, between the landslide dam deposit and overtop flow.

2.5.4. Effect caused by water transfer between soil and water layers

Figure 2.24 shows the calculated results obtained by numerical simulation for infiltration flow and erosion due to overtopping of experimental landslide dams. To understand the influence of water exchange between the soil and water layers on deformation processes due to erosion, the difference between considering and not considering water transfer on the soil and water layers is also shown. The colors in the diagram indicate the water pressure in the deposit; the water pressure was affected by the infiltration flow under unsaturated conditions.

Water exchange affects the erosion processes in a slope. The calculated results of the water pressure were consistent with the observational data obtained using a tensiometer. As shown in **Figure 2.24**, the overtopping starting point was faster than the infiltration flow endpoint because the coefficient of permeability is large. Additionally, saturated conditions on the surface of the landslide dam slope due to water infiltration into the deposit layers are shown in the diagram.

Table 2.10: Parameters used in the calculation, obtained from experimental values.

θ_s	θ_r	ψ_0 (m)	K_s (cm s ⁻¹)	α (°)	d (mm)	ϕ (°)
0.4	0.06	-0.05	1.4	6	1.5	37

Table 2.11: Parameters used in the calculation, taken from a previous study.

m	S_s	$\triangle x$ (cm)	$\triangle y$ (cm)	$\triangle t$ (s)	n_m (m ^{-1/3} s)
6	1.0	20	10	0.001	0.05

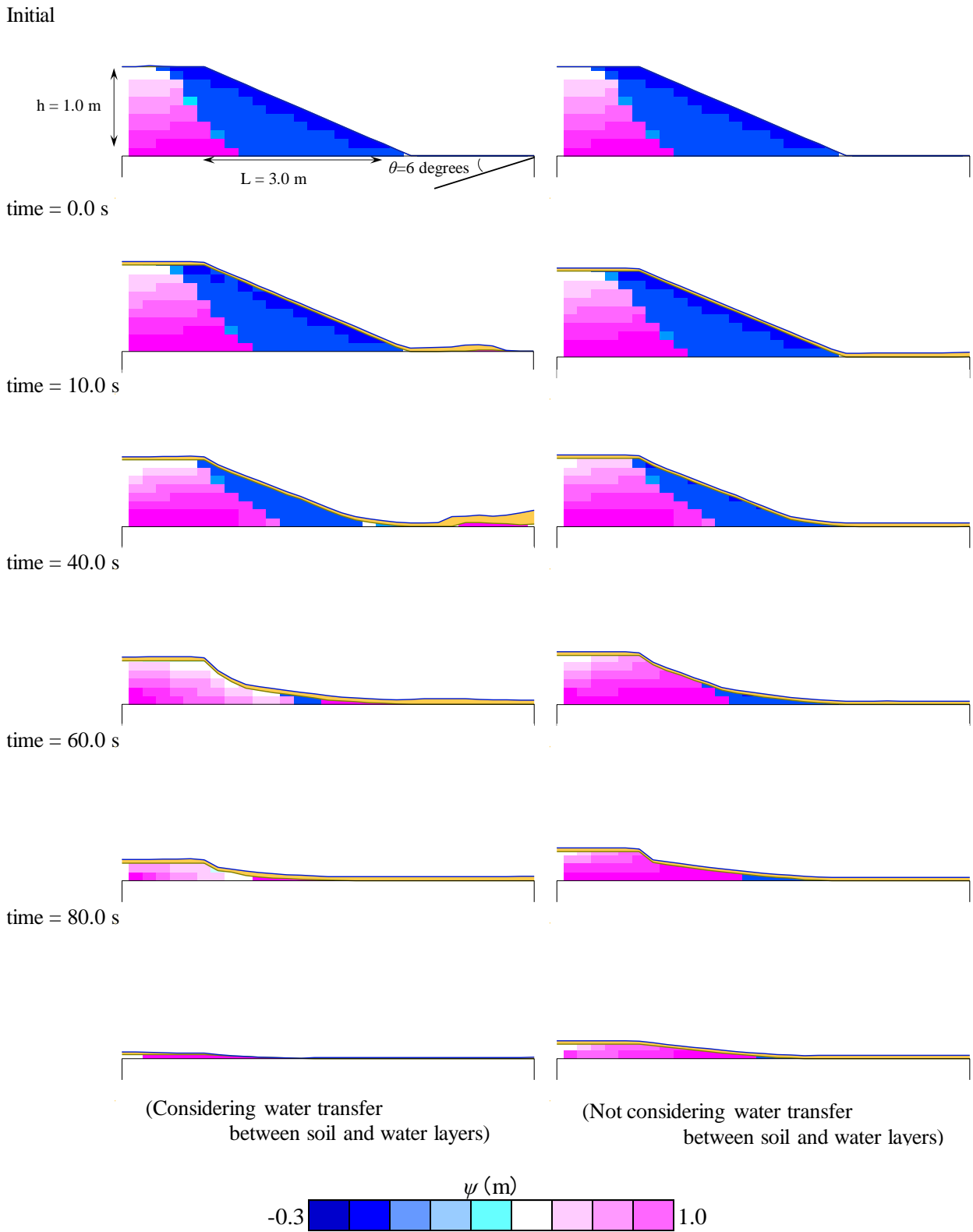


Figure 2.24: Analysis results for infiltration flow and erosion for CASE 1-2.

Comparison of the observed with the calculated data shows that the numerical model that considers the water exchange between soil and water layers can effectively predict landslide dam deformation, as shown in **Figure 2.25**. Additionally, the difference between considering and not considering this water exchange affected landslide dam failure processes.

Figure 2.26 shows the difference in erosion (time = 40.0 s) between considering and not considering water exchange, which affected the erosion in the slope. At the start of erosion, sedimentary layers had already been permeated by the flow due to overtopping. Additionally, the depth of water in the slope increased as water flowed out from the deposit layer into the flow layer, as shown in **Figure 2.26**. This result suggests that the differences in the water depth caused by the water exchange affected the deformation of the landslide dam. Moreover, the thin surface of the deposit layers was saturated due to the water exchange between the soil and water layers. Thus, riverbed shear stress is not needed to account for unsaturated conditions in the calculation of landslide dam deformation caused by erosion due to overtopping. More work is needed to identify the effects of side-shore erosion due to infiltration flow; hence, a 3-D numerical model will be developed in the near future.

2.6. Summary

To predict the flood outflow accompanying landslide dam failure, this study examined the failure and outflow processes of small-scale landslide dam failures through field experiments, small-scale modeling, and statistical analyses. Based on the field experiments, the landslide dam deformation and outflow processes due to overtopping erosion were analyzed using a numerical model.

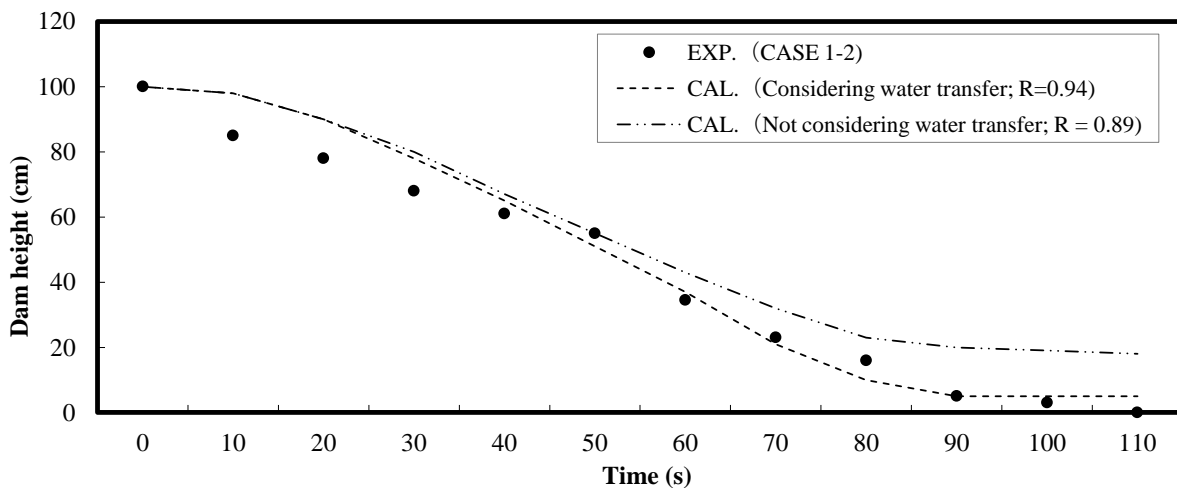


Figure 2.25: Comparison of analysis with experimental data for CASE 1-2.

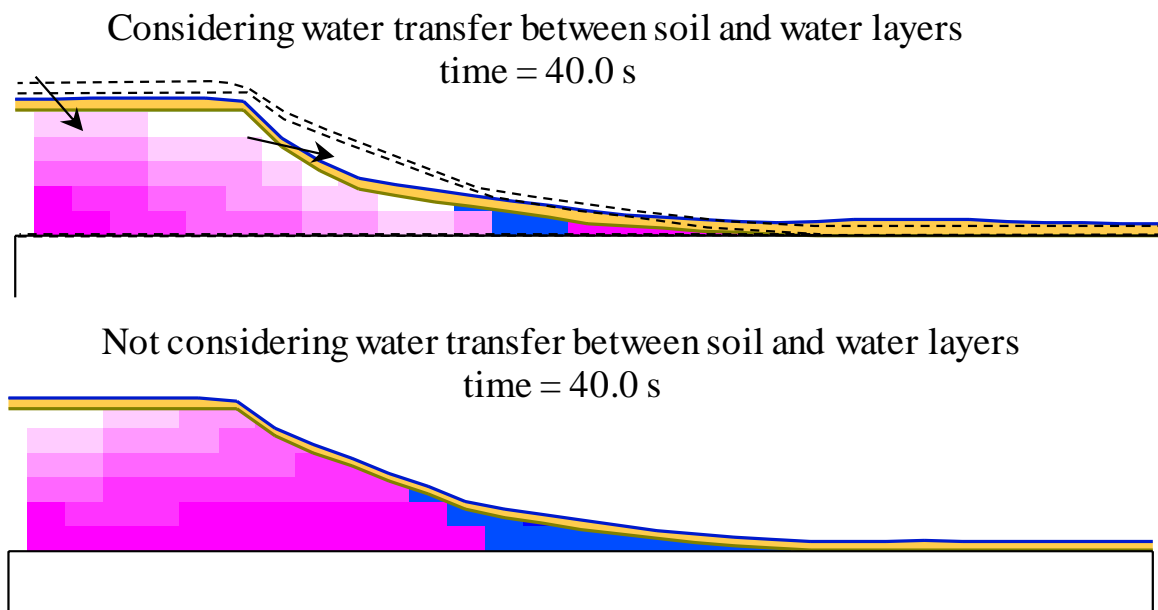


Figure 2.26: Comparison between considering and not considering water transfer with an exchange time of 40.0 s.

Additionally, this study investigated the effect of moisture content on the erosion of landslide dams using a numerical model that incorporated both erosion and infiltration flow processes under saturated and unsaturated conditions.

Experiments with a small-scale artificial landslide dam showed that erosion had a greater effect than other collapse processes. The gradient of the downstream slope affected landslide dam deformation and flood outflow. The flood outflow discharge caused by overtopping erosion was observed to be greater than that in the case of progressive collapse.

The proposed model accurately reproduced the landslide dam collapse and flood outflow processes for both these experiments and past examples of dam deformation. Additionally, the model was used to analyze changes in the stream bed due to erosion. The gradients of both the upstream and downstream slopes and the volume of water in the reservoir behind the landslide dam affected the peak outflow discharge. However, dam height did not have an effect on the results.

The developed model correctly simulated the landslide dam collapse experiment by including unsaturated percolation in the deposit. The calculated results suggest that the difference in water depth caused by water exchange affected the deformation processes of the landslide dam. Future work is needed to identify the effects of side-shore erosion due to infiltration.

BIBLIOGRAPHY

1. Ashida K & Michiue M. 1972. Study on hydraulic resistance and bed-load transport rate in alluvial streams. *Journal of Japan Society of Civil Engineers*, Vol. 206: 55-69.
2. Ashida K, Egashira S & Kamoto M. 1983. Study on the erosion and variation of mountain streams. *Disaster Prevention Research Institute Annuals of Kyoto University*, Vol.26/B-2: 353-361.
3. Chiba M. 2013. Landslide dam failure in Dominican. *Annual research presentation meeting. Japan Society of Erosion Control Engineering*, B: 202-203.
4. Costa J. E. 1988. Floods from dam failure. *Flood Geomorphology*, 436-439.
5. Fujisawa K, Momoki S, Yamamoto K, Kobayashi A & Aoyama S. 2006. Failure mechanism of an embankment due to overflowing from a reservoir. *Journal of Applied Mechanics*, Vol.9: 385-394.
6. Hasegawa K. 1983. Channel morphology of rivers in upstream region. *Thesis of Hokkaido University*.
7. Hashimoto H, Fujita K & Katou Y. 1984. Investigation of levee-erosion mechanism due to flood flow with overtopping. *Technical note of PWRI*, Vol. 2074.
8. Honma H. 1940. A coefficient of overflow on dams. *JSCE Magazine, Civil Engineering*, Vol.26-6: 849-862.
9. Mizuyama T, Ishikawa Y & Fukumoto A. 1989. Report on the failure of a natural dam and countermeasures. *Memorandum of PWRI*, Vol.2744.
10. Mori, T. Sakaguchi T, Inoue K & Mizuyama T. 2011. Measure against landslide dam in Japan. *Kokon Shoin*, 6-11.
11. Oda A, Mizuyama T, Hasegawa Y, Mori T & Kawada K. 2006. Experimental study of process and outflow rate when landslide dams outburst. *Journal of the Japan Society of Erosion Control Engineering*, Vol.59: 29-34.
12. Ogasawara M & Sekine M. 2005. Numerical analysis on formation processes of deposition landform over a permeable bed. *Annual Journal of Hydraulic Engineering*, Vol. 58/No.1, 979-984.
13. Satofuka Y & Mizuyama T. 2009. Numerical simulation of stony debris flow developing on unsaturated deposit. *Annual Journal of Hydraulic Engineering*, Vol. 53: 697-702.
14. Shimizu Y & Itakura T. 1991. Calculation of flow and bed deformation with a general nonorthogonal coordinate system, *Proc of XXIV IAHR Congress, Madrid, Spain*, C-2: 241-248.
15. Takahashi T & Kuang S. F. 1988. Hydrograph prediction of debris flow due to failure of landslide dam. *Disaster Prevention Research Institute Annuals of Kyoto University*, Vol. 31/ B-2: 601-615.

16. Takahashi T, Nakagawa H, Satofuka Y, Okumura Y & Yasumoto D. 1997. Study on the erosion process in mountainous river. *Disaster Prevention Research Institute Annuals of Kyoto University*, Vol. 41/ B-2: 259-273.
17. Takahashi T & Nakagawa H. 1991. Prediction of stony debris flow induced by severe rainfall. *Journal archive/sabo*, Vol.44/No.3: 12-19.
18. Takahashi T & Nakagawa H. 1993. Flood and debris flow hydrograph due to collapse of a natural dam by overtopping. *Annual Journal of Hydro science and Hydraulic Engineering*, Vol. 12: 41-49.
19. Takahashi T, Nakagawa H & Satofuka Y. 2002. Study on sediment flushing using a reverse-flow system. *Disaster Prevention Research Institute Annuals for Kyoto University*, No.45/B: 91-100.
20. Tani M. 1982. The properties of a water-table rise produced by a one-dimensional, vertical, unsaturated flow. *Journal of the Japanese Forest Society*, Vol.64: 409-418.
21. Yoden T, Nakagawa H, Sekiguchi H, Oka F, Gotoh H & Omata A. 2010. Experimental study to understand mechanisms of river embankment by seepage flow and erosion due to overtopping water by using small-scale model. *Advances in River Engineering*, Vol. 16: 347-352.

Chapter 3

Flood Runoff Processes affected by Hydrograph Characteristics

God said to Noah, "I am going to bring floodwaters on the earth to destroy all life under the heavens, every creature that has the breath of life in it. Everything on earth will perish."

Genesis 6:17

3.1. Introduction

Flood control measures using pond reservoirs have been suggested (Ogawa *et al.*, 2012). However, there have been reports of flood hazards caused by pond levee failure due to heavy rains and earthquakes (*e.g.*, The Japanese society of irrigation, drainage and rural engineering, 2005; Hori *et al.*, 2012).

Flooding hazard maps for levee failure of ponds analyzed using a numerical model have been made public by local governments. However, these maps do not consider flood runoff processes affected by the characteristics of the inflow hydrograph from a reservoir (*i.e.*, a pond), which are due to the pond reservoir volume and the levee shape, assuming inflow discharge from the pond (Ootake

et al., 2006; Mori & Nishimura, 2008). For accurate prediction of hazardous flooding downstream, however, it is necessary to take into consideration the characteristics of the inflow hydrograph from the pond (*i.e.*, the timescale).

As discussed in **Chapter 2**, Coast (1988) proposed a relationship between the peak outflow discharge from dams and the dam factor (dam factor = dam height \times reservoir volume). Consequently, the relationship considers the peak flow discharge without changes in the waveform shape (*i.e.*, the characteristics of the hydrograph).

To understand the effects of the hydrograph characteristics from the reservoir (*i.e.*, flood runoff processes), the flow discharge was analyzed under different flow conditions, such as riverbed shearing stress affected by the topography conditions, using a one-dimensional numerical model (Takahashi & Nakagawa, 1991), which considers the water and sediment flow. Finally, a new index is proposed that represents the flood hazardous grade in downstream areas caused by pond levee failure.

3.2. Numerical analysis of flood runoff processes affected by hydrographic differences

3.2.1. Governing equations

Previous studies (Hori *et al.*, 2012) suggested that the flood runoff caused by pond levee failure flows straight to downstream areas. Here, a one-dimensional numerical model that considers the water and sediment flows is used for simplicity (Takahashi & Nakagawa, 1991).

The equation for momentum in the flow direction under depth-average velocity is

$$\frac{\partial u}{\partial t} + u \frac{\partial u}{\partial x} = -g \frac{\partial H}{\partial x} - \frac{\tau_b}{\rho h}. \quad (3.1)$$

The equation for continuation in the flow direction is

$$\frac{\partial h}{\partial t} + \frac{\partial uh}{\partial x} = i_b. \quad (3.2)$$

The equation for continuation of the grid is

$$\frac{\partial Ch}{\partial t} + \frac{\partial Chu}{\partial x} = i_b C_*, \quad (3.3)$$

and the equation for continuation of the riverbed is

$$\frac{\partial z}{\partial t} + i_b = 0, \quad (3.4)$$

where u is the average velocity in the direction of flow, t is time, x is the flow distance, g is the acceleration due to gravity, τ_b is the riverbed shearing stress, H is the altitude from the sea level, ρ is the interstitial fluid density, h is the flow depth, i_b is the erosion/deposition velocity, C is the sediment concentration of the volume flow, C_* is the sediment concentration by volume in the movable bed layer, and z is the riverbed height.

Considering the characteristics of the sediment concentration of the volume flow, the riverbed shearing stresses of flow τ_b were classified into three types (Takahashi & Nakagawa, 1991): stone debris flow, immature debris flow, and bed load transport. These are represented by the following equations:

1. Stone debris flow: $C \geq 0.4C_*$

$$\frac{\tau_b}{\rho h} = \frac{d^2 u |u|}{8h^3 \{C + (1-C)\rho/\sigma\} \{(C_*/C)^{1/3} - 1\}^2}, \quad (3.5)$$

2. Immature debris flow: $0.01 < C < 0.4C_*$

$$\frac{\tau_b}{\rho h} = \frac{1}{0.49} \frac{d^2}{h^3} u |u|, \quad (3.6)$$

3. Bed load transport: $h/d \geq 30$ or $C \leq 0.01$

$$\frac{\tau_b}{\rho h} = \frac{gn_m^2 u |u|}{h^{4/3}}, \quad (3.7)$$

where ρ is the interstitial fluid density, σ is the bulk density of grit, d is the particle diameter of the grit, and n_m is Manning's riverbed roughness coefficient.

The erosion/deposition velocity i_b is

1. Erosion: $C < C_\infty$

$$i_b = \delta_e \frac{C_\infty - C}{C_* - C_\infty} \frac{q}{d}, \quad (3.8)$$

2. Deposition: $C \geq C_\infty$

$$i_b = \delta_d \frac{C - C_\infty}{C_* - C_\infty} \frac{q}{h}, \quad (3.9)$$

where C_∞ is the equilibrium sediment concentration, q is the unit width flow discharge, δ_e is the coefficient of erosion, and δ_d is the coefficient of deposition. The equilibrium sediment concentration C_∞ is

$$C_{\infty} = \frac{\rho \tan \theta_w}{(\sigma - \rho)(\tan \phi - \tan \theta_w)}, \quad (3.10)$$

where θ_w is the water-surface gradient and ϕ is the internal frictional angle of the grit.

The generation and development of debris flow are calculated with a staggered scheme and arrangement variables.

3.2.2. Calculation conditions

The flood runoff processes affected by the characteristics of the inflow hydrographs from the reservoir were estimated under ideal conditions that were assumed with reference to Takahashi & Nakagawa (1991), as shown in **Table 3.1**. Here, the flood runoff processes affected by the river width, riverbed gradient, and sediment concentration of the volume flow are analyzed.

To understand the flood runoff processes affected by the characteristics of the inflow hydrograph from the reservoir as an upstream condition, the factors that affected the flood runoff processes were analyzed using the numerical model for seven assumed hydrographs, as shown in **Figure 3.1**.

3.2.3. Factors affected by the characteristics of the hydrograph from the pond

Table 3.1: Parameters used in the calculation.

Δt (s)	Δx (m)	ρ (kg m ⁻³)	n_m (m ^{-1/3} s)	d (m)
0.001	10.0	1.1	0.05	0.1

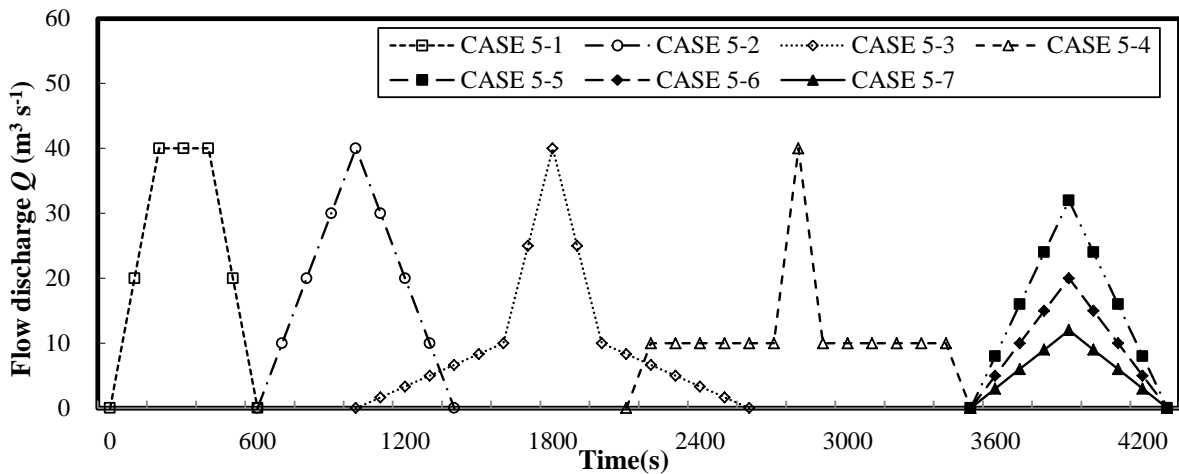


Figure 3.1: Analysis case study for hydrograph under inflow conditions.

To understand the flood flow processes affected by the characteristics of the inflow hydrograph from the reservoir, the peak outflow discharge at different observation points (different flow distances) was analyzed using the hydrograph (CASES 5-1, 5-2, 5-3, & 5-4) as shown in **Figure 3.1**. Other variables were kept constant: riverbed gradient $i = 0.04$, river width $B = 10$ m, and sediment concentration of volume flow $C = 0$, as shown in **Figure 3.2**.

In **Figure 3.2**, the y-axis is the non-dimensional peak flow discharge at each observation point (*i.e.*, the peak outflow discharge at each observation point divided by the maximum outflow discharge; $Q_{0\max} = 40 \text{ m}^3 \text{ s}^{-1}$), and the x-axis is the flow distance between the boundary of the upstream (pond) and the observation point.

The peak flow discharge of each hydrograph as shown in **Figure 3.1** changed under the flood runoff processes affected by the characteristics of the inflow hydrograph from the reservoir. In addition, **Figure 3.2** suggests that the ratio of each peak outflow discharge was almost unchanged in the downstream area from more than 500 m downstream.

Here, the peak flow discharge was analyzed in cases with different riverbed gradients. However, other variables were constant: the flow distance at the observation point $L = 1,500$ m, the river width $B = 10$ m, and the sediment concentration of the volume flow $C = 0$, as shown in **Figure 3.3**.

In **Figure 3.3**, the y-axis is the non-dimensional peak flow discharge, and the x-axis is the riverbed gradient. The peak flow discharge of each inflow hydrograph, as shown in **Figure 3.1**, changed under the flood runoff processes affected by the characteristics of the inflow hydrograph from the reservoir.

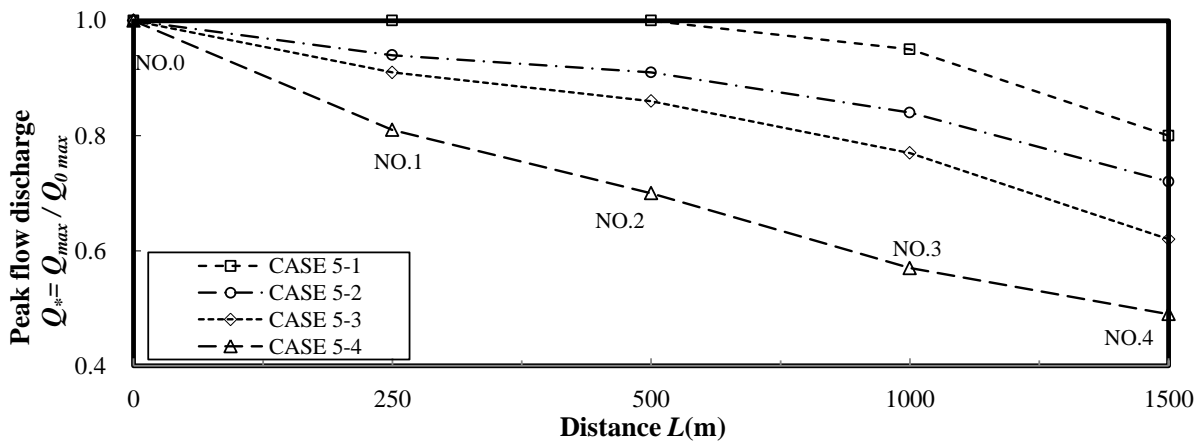


Figure 3.2: Relationship between flow distance and non-dimensional peak flow discharge (CASES 5-1, 5-2, 5-3, & 5-4).

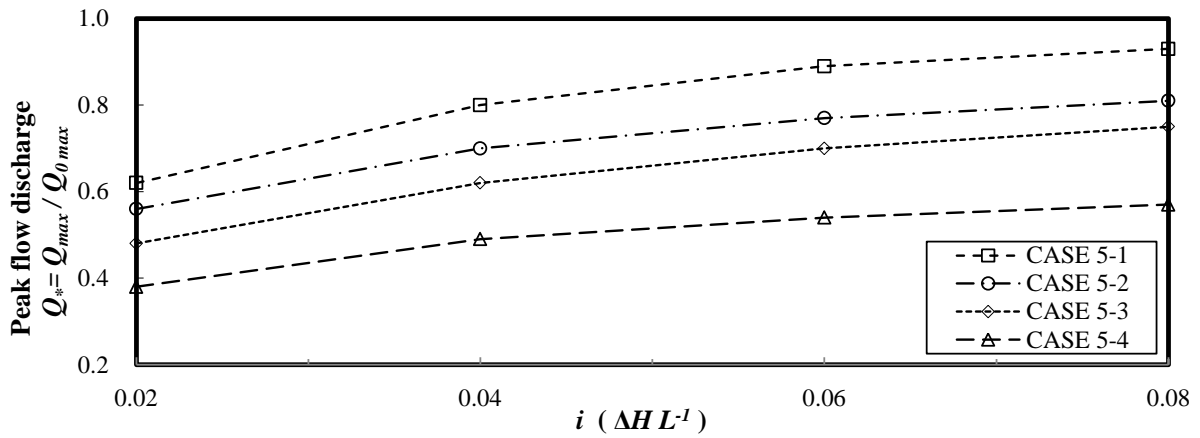


Figure 3.3: Relationship between the riverbed gradient and non-dimensional flow discharge (CASES 5-1, 5-2, 5-3, & 5-4).

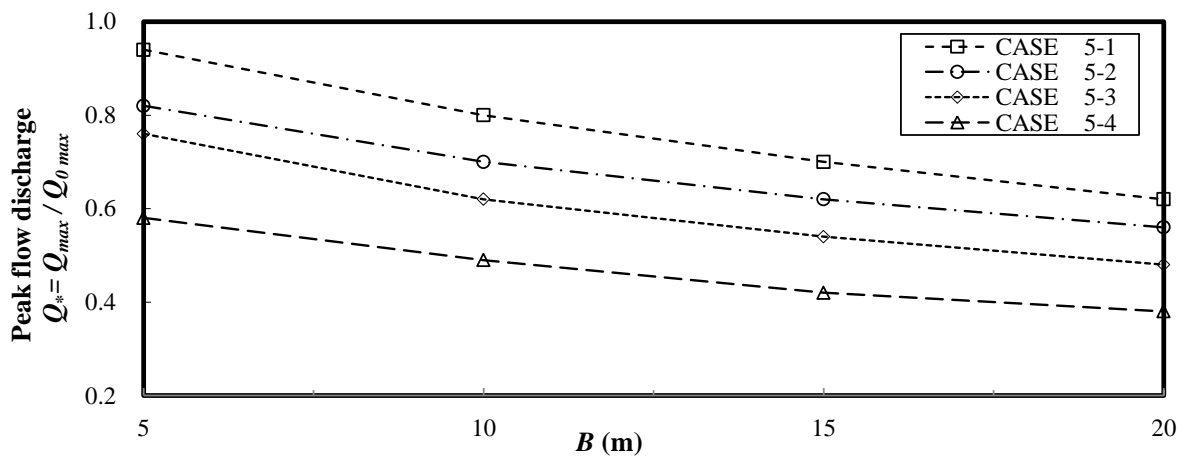


Figure 3.4: Relationship between the river width and the non-dimensional flow discharge (CASES 5-1, 5-2, 5-3, & 5-4).

Here, the peak flow discharge was analyzed in cases with different river widths. However, other variables were constant: the flow distance at the observation point $L = 1500$ m, the riverbed gradient $i = 0.04$, and the sediment concentration of volume flow $C = 0$, as shown in **Figure 3.4**.

In **Figure 3.4**, the y -axis is the non-dimensional peak flow discharge and the x -axis is the river width. The peak flow discharge of each hydrograph, as shown in **Figure 3.1**, changed under the flood runoff processes affected by the characteristics of the inflow hydrograph from the reservoir.

Finally, the flow discharge was analyzed in cases with different volume flow sediment concentrations.

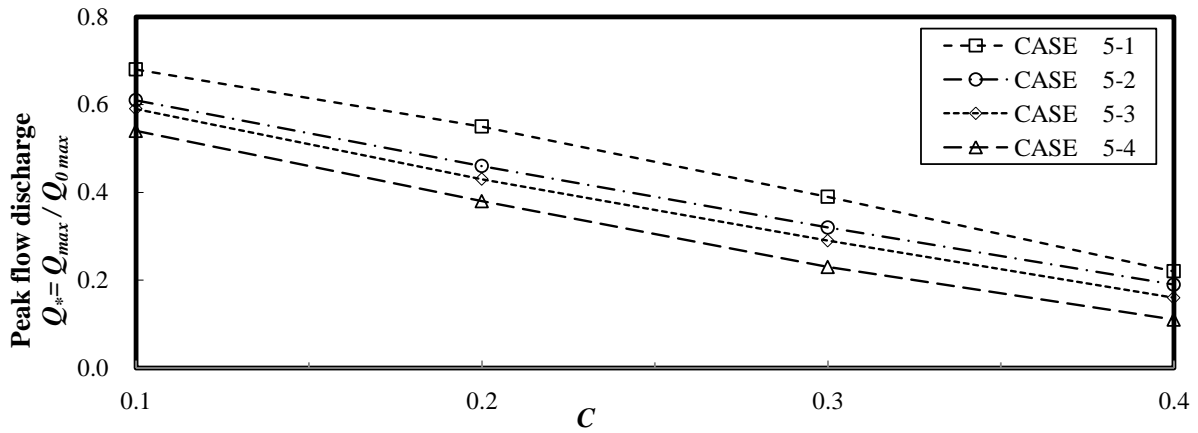


Figure 3.5: Relationship between the sediment concentration of the volume flow and the non-dimensional flow discharge (CASES 5-1, 5-2, 5-3, & 5-4).

However, the other variables were constant: flow distance at the observation point $L = 1500$ m, riverbed gradient $i = 0.04$, and river width $B = 10$ m, as shown in **Figure 3.5**.

In **Figure 3.5**, the y-axis is the non-dimensional peak outflow discharge, and the x-axis is the sediment concentration of the volume flow. Comparison of the results shown in **Figure 3.5** with those in **Figures 3.2, 3.3, and 3.4** indicates that the different sediment concentrations of the volume flow were not affected by the characteristics of the hydrograph from the reservoir.

3.3. Evaluation of flood runoff affected by the hydrographic characteristics

The effects of the characteristics of the inflow hydrograph from the reservoir can be used to evaluate the flood flow processes affected by these characteristics. Using the ratio of the flow discharge difference shown in **Figure 3.2**, the results obtained here suggested a relationship between the effects of a characteristic on the inflow hydrograph from the reservoir and flow discharge by trial and error. The relationship between flow discharge and inflow hydrograph characteristics is

$$Q_{\max} = \alpha \cdot Q_{0\max}^{\beta} \cdot \Sigma Q_{85}, \quad (3.11)$$

where Q_{\max} is the flood flow discharge in the downstream area, $Q_{0\max}$ is the inflow discharge from the reservoir as shown in **Figure 3.6**, and ΣQ_{85} is the proposed new index obtained by sensitivity analysis: subtraction of 15 % of the lower flow discharge from the whole flow discharge as shown in **Figure 3.6**, where both α and β are coefficients. Consequently, this new index is proposed as a flood hazard degree in the downstream area, considering the characteristics of the inflow hydrograph from the reservoir as

$$F_H = Q_{0max}^{1/2} \cdot \Sigma Q_{85}, \tag{3.12}$$

where F_H is the proposed new index, assuming $\alpha = 1.0$. If F_H is larger, the hazardous flooding in the downstream area is greater. The results of the analysis suggested that the correlation coefficient was 0.89, assuming $\beta = 0.5$, as shown in **Figure 3.7**. Further work is needed to improve the accuracy of the new index.

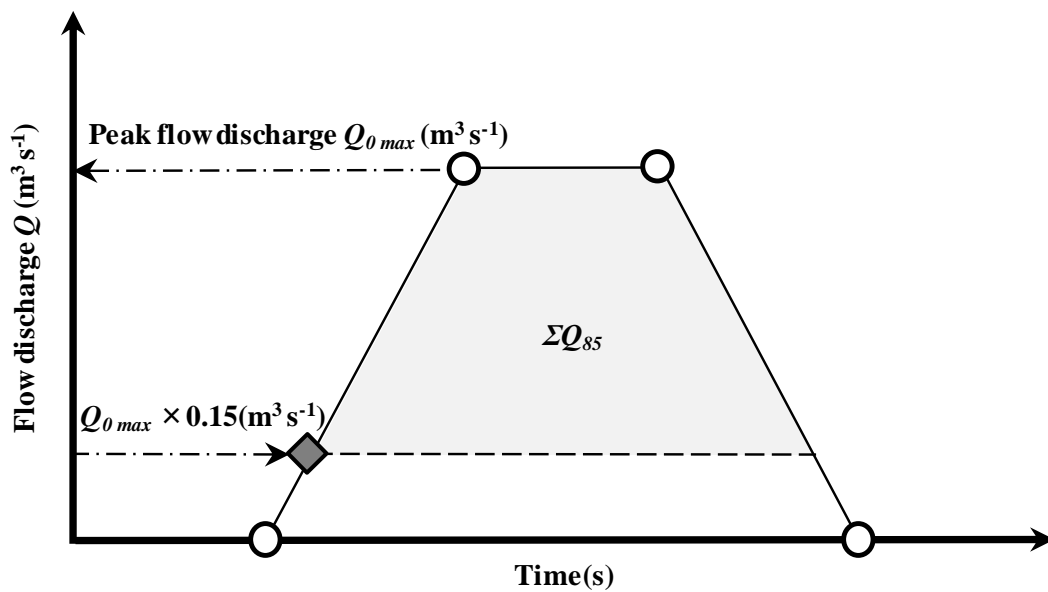


Figure 3.6: Schematic to calculate the proposed new index F_H .

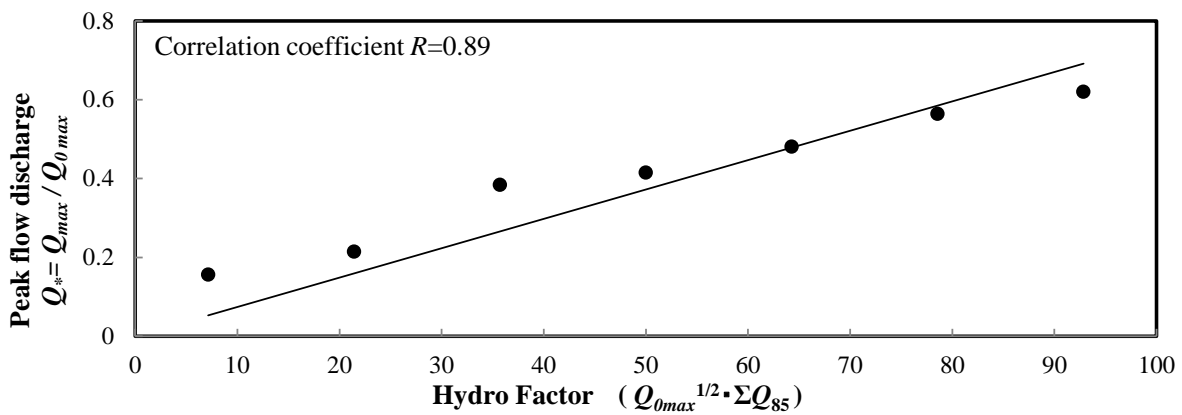


Figure 3.7: Relationship between the new index and non-dimensional peak flow discharge.

3.4. Summary

To understand flood runoff processes to the downstream area affected by the characteristics of the inflow hydrograph from the reservoir (e.g., pond, landslide dam), the relationship between the effects and characteristics of the inflow hydrograph from the reservoir were analyzed using a one-dimensional numerical model that considered the water and sediment flow.

The results suggested that the characteristics of the inflow hydrograph from the reservoir due to the levee failure affected flood runoff processes in the downstream area. In addition, a new index of flood hazard grade in the downstream areas was proposed, considering the characteristics of the inflow hydrograph from the reservoir.

BIBLIOGRAPHY

1. Costa J. E. 1988. Floods from dam failure. *Flood Geomorphology*, 436-439.
2. Hori T, Mouri E & Ueno K. 2012. Damage of a reservoir and seismic capacity evaluation. *The Foundation Engineering & Equipment*, Vol. 40 (8): 65-67.
3. The Japanese society of irrigation, drainage and rural engineering. 2005. Report of the Awaji reservoir damage investigation caused by the 2004 typhoon No. 23.
4. Mori T & Nishimura S. 2008. Risk assessment and reliability-based design for overflow of irrigation tank, *The Japanese society of irrigation, drainage and rural engineering annual meeting, the collection of lecture summaries*, 622-623.
5. Ogawa K, Tamura T, Mutou H & Takigawa N. 2012. Evaluation of measures and effective use of flood control ponds in small and medium-sized rivers with flood damage. *Advance in River Engineering*, Vol. 18: 505-510.
6. Ootake T, Motooka T, Nakagawa T, Kitamura S, Katou H & Ootake Y. 2006. Reservoir flooding simulation using the two-dimensional flow models and a hazard map. *The Japanese society of irrigation, drainage and rural engineering annual meeting, the collection of lecture summaries*, 910-911.
7. Takahashi T & Nakagawa H. 1991. Prediction of stony debris flow induced by severe rainfall. *Journal archive/sabo*, Vol. 44/ No.3: 12-19.

Chapter 4

Prediction of Sediment Runoff in a Mountain Watershed

Moses said to the LORD, "The people cannot come up Mount Sinai, because you yourself warned us, 'Put limits around the mountain and set it apart as holy.'"

Exodus 19:23

4.1. Introduction

Prediction of flood runoff under rainfall conditions is an important factor in assessment of the potential environmental impacts of a river system on its adjacent land uses. Araki *et al.* (2008) developed a numerical model that describes a system for distributed rainfall–runoff prediction. However, the point of predicting rainfall and flood runoff is to ascertain flow water levels that are needed to evaluate both water depth and river sedimentation. Previous numerical models of rainfall–runoff considered only water flow, not variations on the riverbed. Takahashi *et al.* (1999) reported the necessity of considering riverbed variation caused by the sediment yield of mountainous areas, which tend to yield sediment depending on the geology type. Improving the numerical model with analysis of the sediment runoff could enable the prediction of ordinary riverbed variations, which is in turn an effective method for identification of thresholds beyond which potential environmental problems arise, such as reservoir sedimentation, bridge-pier scour, and watershed-sedimentation management.

Consequently, the improved numerical model can be used in several cases, not just in the analysis of flood runoff.

Prediction of sediment runoff has been investigated by numerous researchers (Takahashi *et al.*, 2000; Hashimoto *et al.*, 2003; Mouri *et al.*, 2003; Ozawa *et al.*, 2011; and Hirasawa *et al.*, 2012). Takahashi *et al.* (2000) analyzed changes in the distribution of several particle diameters in sediment runoff. Hashimoto *et al.* (2003) studied the suspended sediment runoff in large concentrations. Mouri *et al.* (2003) calculated the sediment yield using an infinite slope stability model. Ozawa *et al.* (2011) predicted sediment runoff considering water-borne particulates as being under non-equilibrium suspension before deposition in reservoirs. Finally, Hirasawa *et al.* (2012) compared the results of observations in a mountainous basin for 20 days with results simulated with the numerical model of Takahashi *et al.* (2000).

To verify the numerical model in predicting sediment runoff as enhanced of Hirasawa *et al.* (2000), the results of seven months of observations are compared with calculations using this new model. In addition, a new relationship between watershed area and channel width is proposed using statistical analysis of data from over 800 mountain streams.

4.2. Prediction of channel width using the basin area

4.2.1. Relationship between channel width and basin area using Resume's theory

Interpretation of aerial photographs was used to compile geological data for the numerical model. Unfortunately, forest obscures much of the mountainous terrain, which results in loss of data. To help relieve this situation, a relationship is proposed here between channel width and the basin area based on the results of statistical analysis of existing stream data (Shiga Prefecture, 2011).

According to Resume's theory, the relationship of channel width and flow discharge is as follows:

$$B_0 \approx \alpha Q^{1/2}, \text{ and} \quad (4.1)$$

$$B_0 \approx (\alpha k^{1/2} r_e^{1/2}) A^{1/2} = \beta A^{1/2}, \quad (4.2)$$

where B_0 is the channel width, Q is the flow discharge, r_e is the effective rainfall intensity, A is the area of the upper basin, and α , β , and k are coefficients: β was determined statistically using the data from 838 stream channels.

4.2.2. Factors determining the channel width

Figure 4.1 shows the relationship between channel width and other factors by statistical analysis. Channel width is strongly related to the area of the upper basin as well as to geology and vegetation.

4.2.3. Predicted relation of channel width based on regression analysis

Considering the basin geology and vegetation, the relationship between basin area and channel width was subjected to regression analysis to obtain the coefficient β ; part of the analytical results considered only the geology, and not vegetation type, due to lack of samples.

Table 4.1 shows the regression analytical results based on a scatter diagram, and Figures 4.2 to 4.13 show the regression lines. The average correlation coefficient R is 0.73 (range 0.57 – 0.86). Further studies are needed to verify the regression coefficient β for other watersheds.

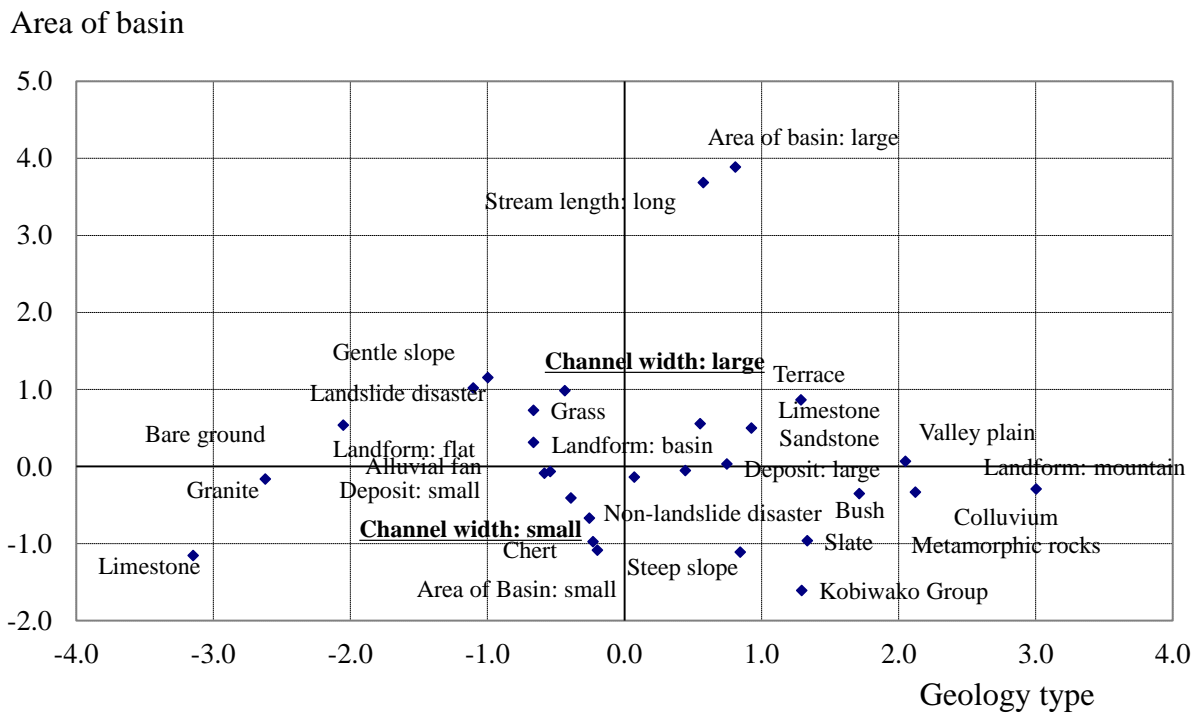


Figure 4.1: Factors determining channel width using Mathematical Quantification Theory Class III.

Table 4.1: Regression analytical results of factors determining channel width.

Geology	Vegetation	Number	Correlation coefficient: R	Regression coefficient: β
<i>Limestone or Sandstone</i>	Forest	171	0.57	6.8
	Grasses	87	0.70	9.4
	Bare ground	55	0.71	5.4
<i>Slate</i>	-	29	0.74	5.7
<i>Chert</i>	-	13	<u>0.86</u>	6.0
<i>Granite</i>	Forest	72	0.69	10.9
	Grasses	74	0.61	5.8
	Bare ground	111	0.72	5.4
<i>Pliocene–Pleistocene Kobiwako Group</i>	-	18	0.79	4.8
<i>Colluvium or Metamorphic Rocks</i>	Forest	135	0.71	9.3
	Grasses	34	<u>0.80</u>	7.9
	Bare ground	39	<u>0.86</u>	8.2

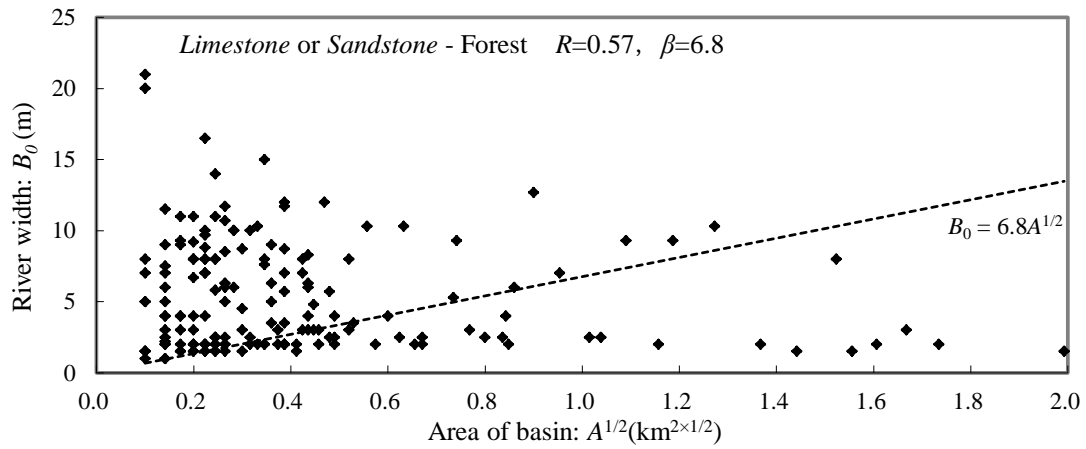


Figure 4.2: Relationship between channel width and basin area
(geology: *Limestone or Sandstone*; vegetation: Forest) .

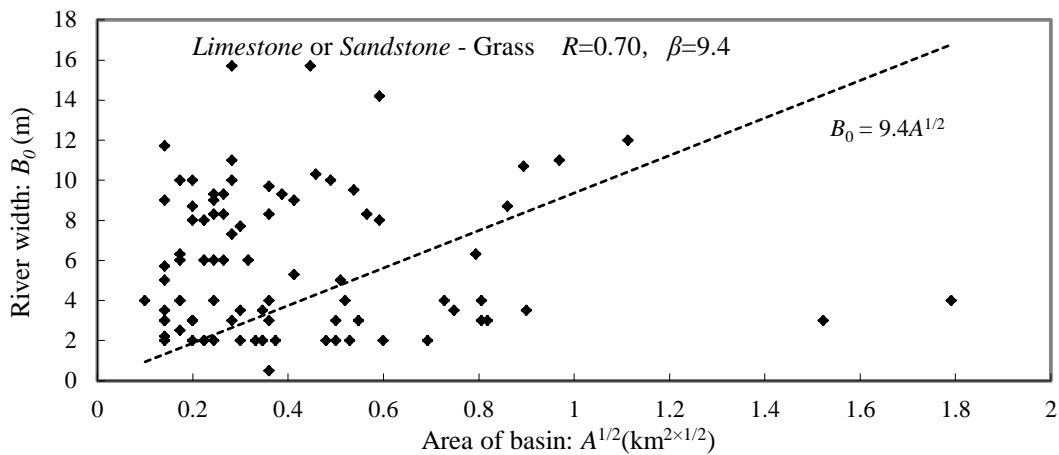


Figure 4.3: Relationship between channel width and basin area
(geology: *Limestone or Sandstone*; vegetation: Grasses).

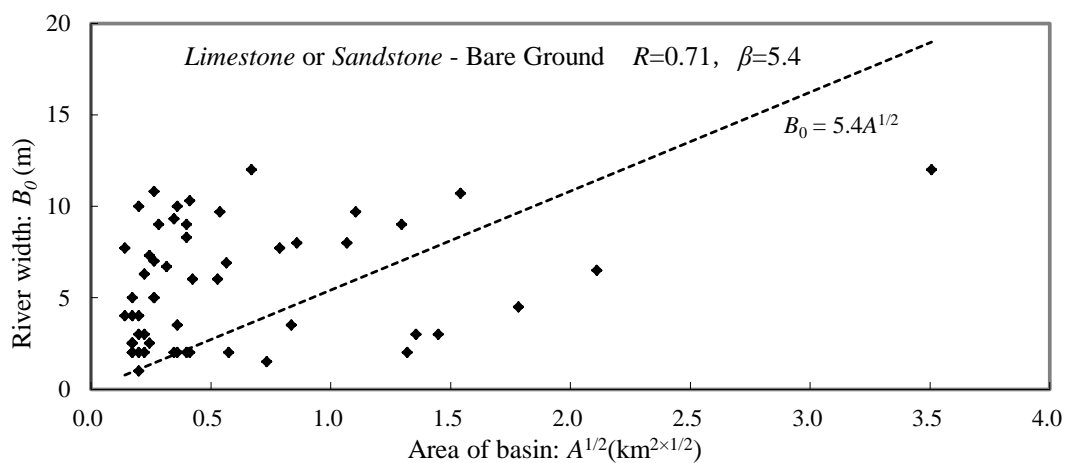


Figure 4.4: Relationship between channel width and basin area
(geology: *Limestone or Sandstone*; vegetation: Bare ground).

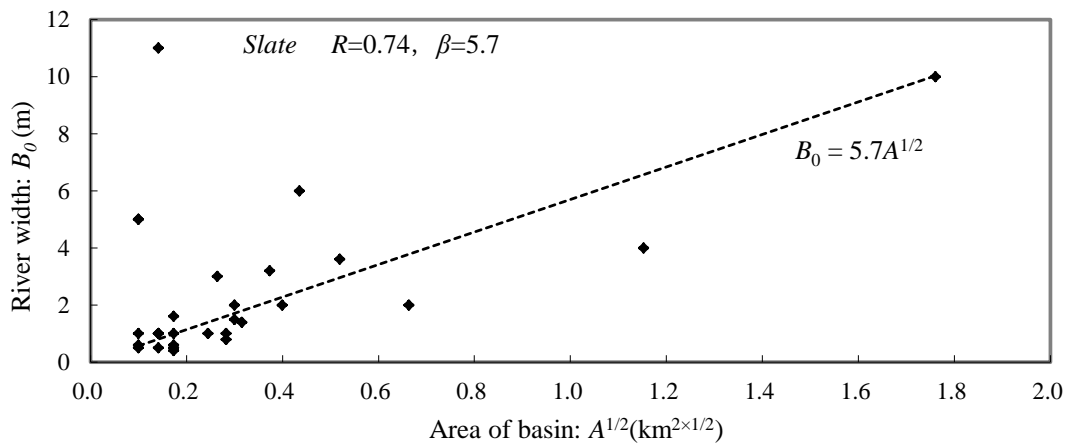


Figure 4.5: Relationship between channel width and basin area (Geology: *Slate*).

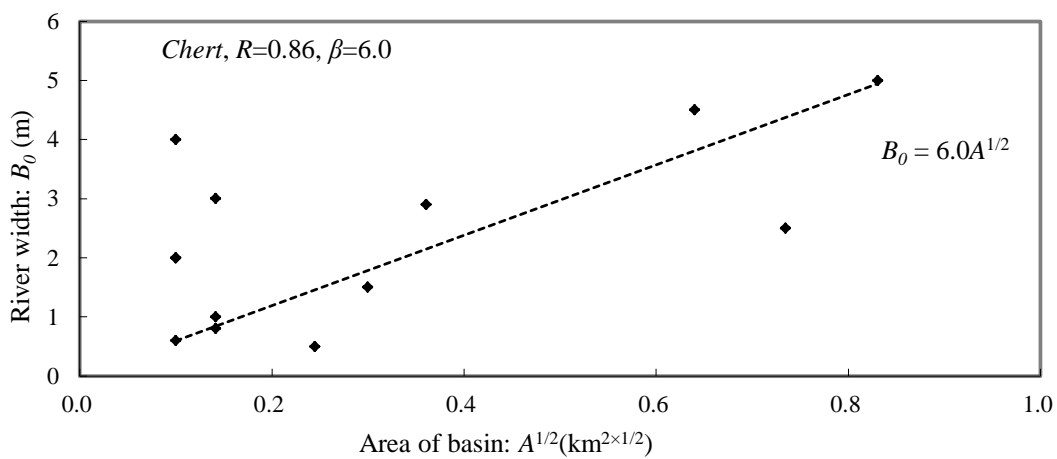


Figure 4.6: Relationship between channel width and basin area (geology: *Chert*).

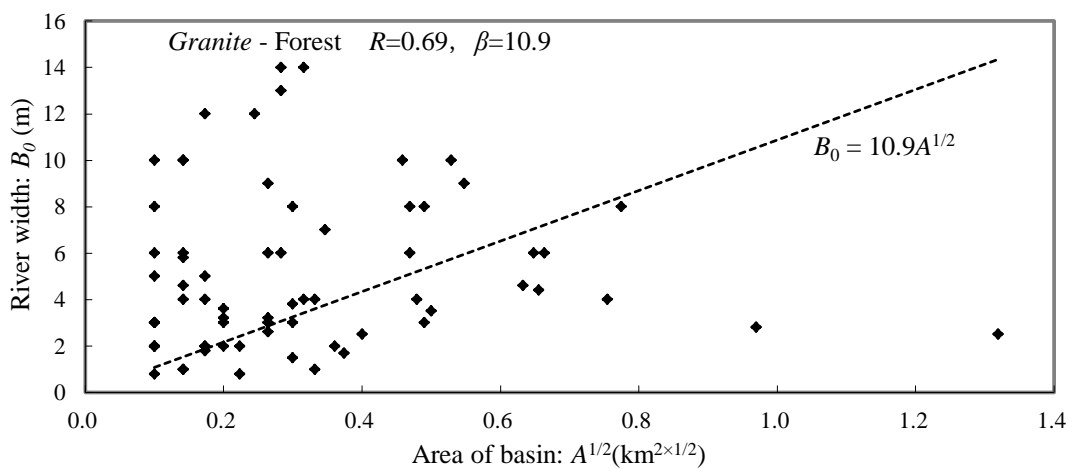


Figure 4.7: Relationship between channel width and basin area (geology: *Granite*; vegetation: *Forest*).

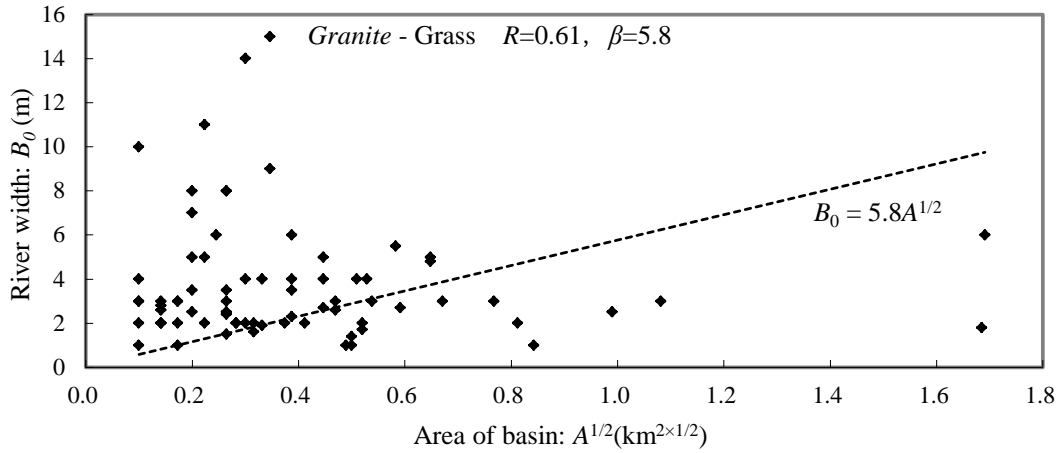


Figure 4.8: Relationship between channel width and basin area (geology: *Granite*; vegetation: Grasses).

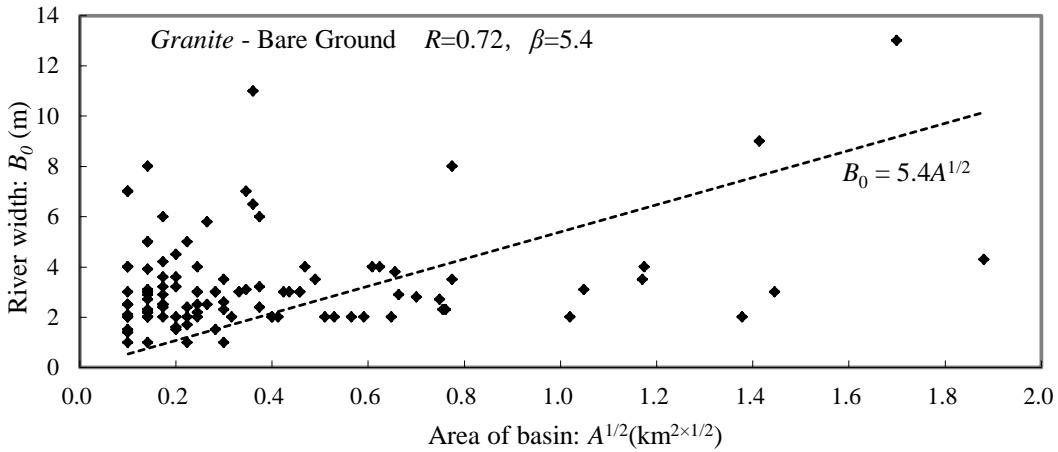


Figure 4.9: Relationship between channel width and basin area (geology: *Granite*; vegetation: Bare ground).

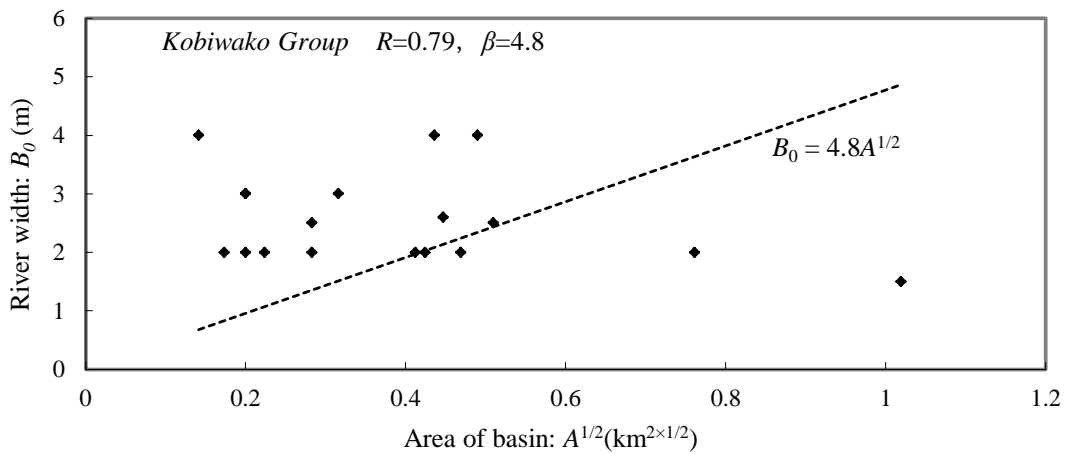


Figure 4.10: Relationship between channel width and basin area (geology: *Pliocene–Pleistocene Kobiwako Group*).

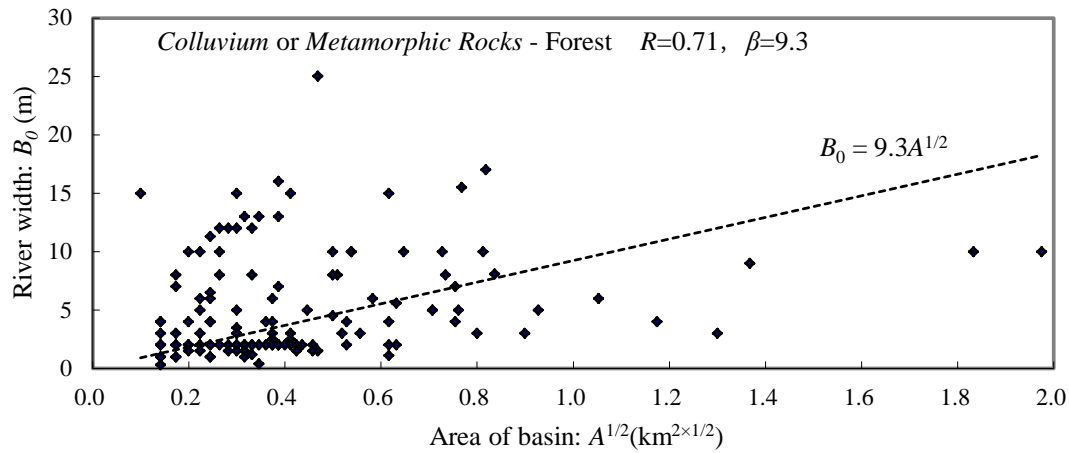


Figure 4.11: Relationship between channel width and basin area (geology: *Colluvium or Metamorphic Rock*; vegetation: Forest).

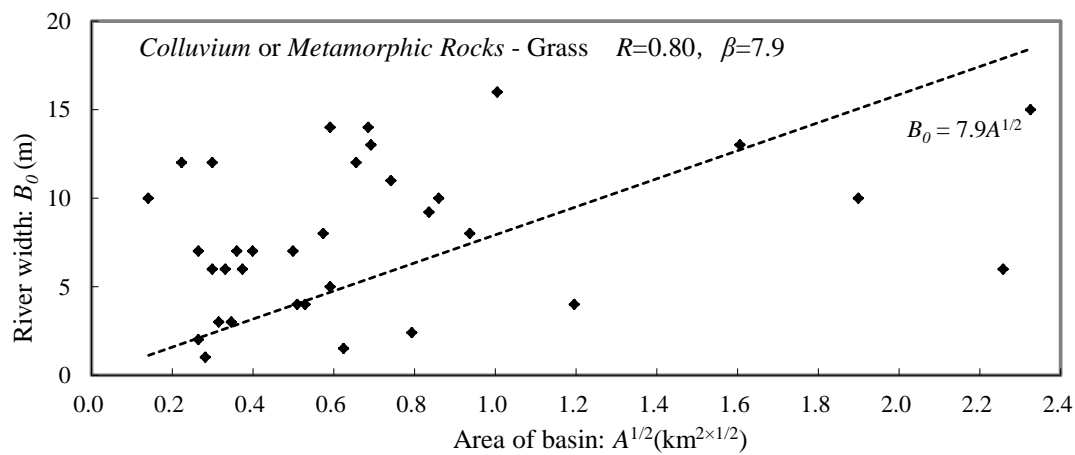


Figure 4.12: Relationship between channel width and basin area (geology: *Colluvium or Metamorphic Rock*; vegetation: Grasses).

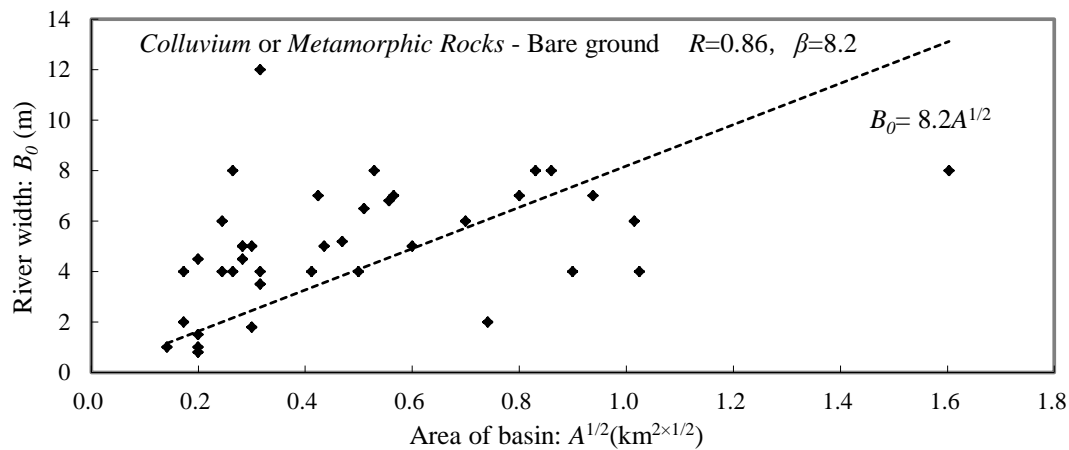


Figure 4.13: Relationship between channel width and basin area (geology: *Colluvium or Metamorphic Rock*; vegetation: Bare ground).

4.3. Numerical analysis for prediction of sediment runoff in mountain channels

The numerical model for prediction of sediment runoff takes into consideration unit slope area and unit channel width in the basin, gathering both water and sediment yield in the slope area flow into adjacent channels. In addition, the one-dimensional flood runoff numerical model of Takahashi *et al.* (2000), which considers sediment runoff, was used to calculate the variations of the channel bed.

4.3.1. Basic equations for the prediction of flood and sediment runoff

a. Flood runoff analysis

Flood runoff is obtained on all calculation meshes under given rainfall conditions prior to calculating sediment runoff, and before the riverbed variations assumed to be the sediment source in the water flow can be calculated. The following Kinematic Wave Method is used, governed by the equation of motion, the continuity equation for water flow, and Manning's uniform flow equations. Hence, the fundamental equations on the mountain slope include

$$q_s = \alpha_k h^m, \quad \alpha_k = \frac{\sin^{1/2} \theta_s}{n_e}, \quad \text{and} \quad (4.3)$$

$$\frac{\partial h}{\partial t} + \frac{\partial q_s}{\partial x} = r_e, \quad (4.4)$$

where q_s is the unit width discharge of surface flow, θ_s is the slope gradient, n_e is the equivalent roughness coefficient, r_e is the effective rainfall intensity, h is the flow depth, and m is a coefficient.

The unit length discharge of flow into the channel q_{in} is given by equations (4.3) and (4.4) as follows:

$$q_{in} = q_s \frac{l'}{l}, \quad l' = \frac{S}{L_s}, \quad (4.5)$$

where l' is the slope width corresponding to channel length, l is the channel length corresponding to the adjacent slope, S is the slope area, and L_s is the slope length as shown in **Figure 4.14**.

The unit width discharge in the channel at the uppermost channel q_{in} is

$$q_{in} = q_s \frac{l'}{B}, \quad (4.6)$$

where B is the channel width as shown in **Figure 4.15**.

Neglecting the increase and decrease in discharge due to erosion and deposition, respectively, of sediment, flood runoff analysis in the river channel is calculated by

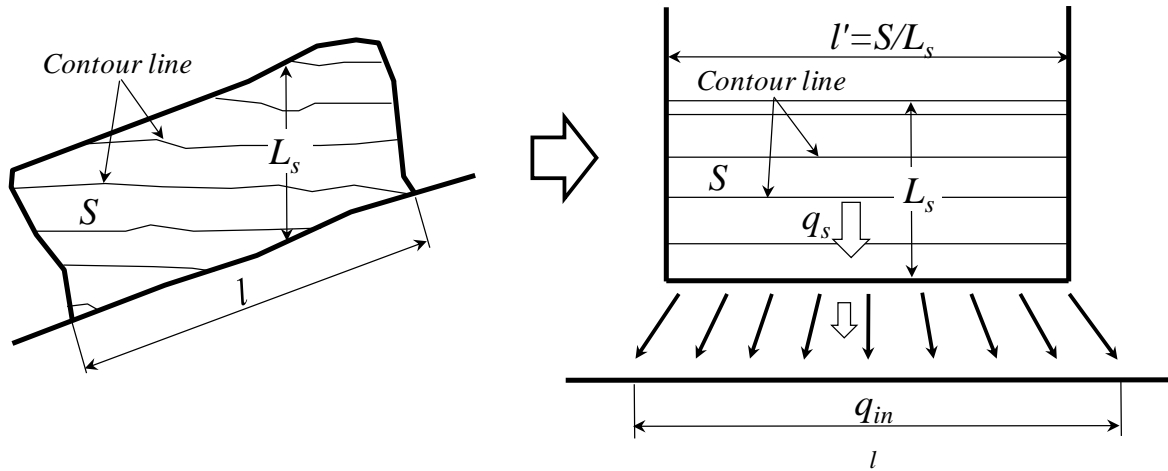


Figure 4.14: Schematic for calculation of flood runoff in the river channel from the slope.

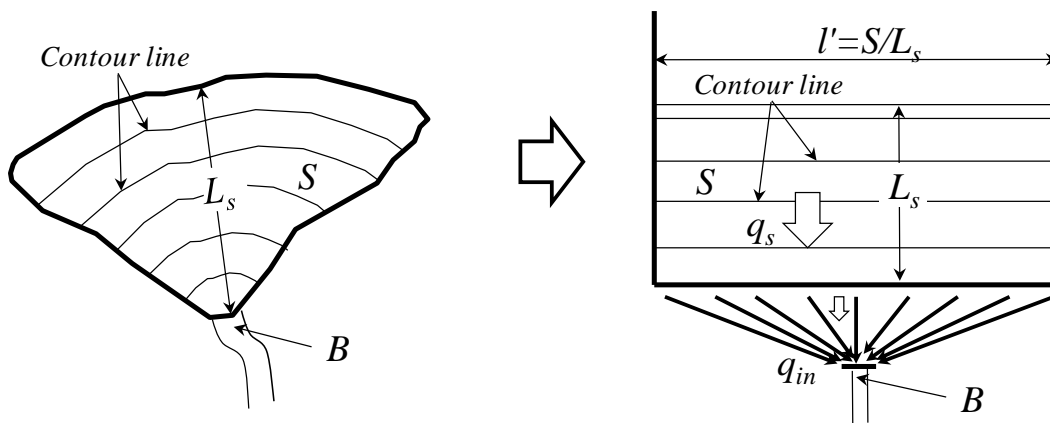


Figure 4.15: Schematic for calculation of flood runoff at uppermost channel from the slope.

$$q = \frac{1}{n_m} h^{5/3} \sin^{1/2} \theta_w, \text{ and} \quad (4.7)$$

$$\frac{\partial h}{\partial t} + \frac{\partial q}{\partial x} = q_{in}, \quad (4.8)$$

where q is the unit width discharge in the river channel, n_m is the Manning's riverbed roughness coefficient, and θ_w is the water surface gradient.

b. Riverbed shearing inflow

Due to slope failures along riverbanks, river water flow erodes the slumped material and transports the resulting sediment downstream. In general, sediment concentration suspended in the flow is

strongly affected by the riverbed gradient. If the sediment concentration in the flow is considered, riverbed shearing can be classified into three flow types (Takahashi & Nakagawa, 1991):

1. Stone debris flow: $C_L \geq 0.4C_{*L}$

$$q = \frac{2}{5d_{mL}} \left\{ \frac{g}{0.02} \frac{\sigma \cdot C_L + (1 - C_L)\rho}{\sigma} \right\}^{1/2} \cdot \left\{ \left(\frac{C_{*L}}{C_L} \right)^{1/3} - 1 \right\} h^{5/2} \sin^{1/2} \theta_w, \quad (4.9)$$

2. Immature debris flow: $0.01 < C_L < 0.4C_{*L}$

$$q = \frac{0.7\sqrt{g}}{d_{mL}} h^{5/2} \sin^{1/2} \theta_w, \quad (4.10)$$

3. Bed load transport: $h/d_{mL} \geq 30$ or $C_L \leq 0.01$

$$q = \frac{1}{n_m} h^{5/3} \sin^{1/2} \theta_w, \quad (4.11)$$

where q is the unit width flow discharge including the sediment discharge, g is the acceleration due to gravity, ρ is the interstitial fluid density, σ is the bulk density of grains, C_L is the sediment concentration of the volume flow, d_{mL} is the particle diameter of grains, C_{*L} is the sediment concentration by volume in the movable bed, and n_m is Manning's riverbed roughness coefficient. However, further investigations of the n_m of turbulent debris flow are required.

c. Preparation for calculation of particle diameter change

In general, erosion and deposition are neglected in flood runoff analysis. However, depending on the gradient, the riverbed material together with confined water within the bed will be captured in the flow, if the solids load in the flow is still less than equilibrium and erosion continues. In contrast, if the ability of the flow is insufficient to transport the load, sediment will be deposited. Therefore, erosion and deposition will change the flow discharge, as well as the particle composition in the flow and on the bed.

To consider the variation in particle-size distribution of the flow and on the bed, the grain size is divided into k_e grades, and the diameter of the k th grade grain is written as d_k . Particles from grade $k = 1$ to $k = k_1$ are defined as fine and considered to constitute a fluid phase if carried in suspension in the flow. Particles from grades $k = k_1 + 1$ to $k = k_e$ are defined as coarse.

The volumetric concentration of coarse C_L and fine C_F fractions, density of the interstitial muddy fluid ρ_m , and mean diameter of the coarse particles in the flow d_{mL} are expressed as follows:

$$C_L = \sum_{k=k_1+1}^{k_e} C_k, \quad (4.12)$$

$$C_F = \frac{\sum_{k=1}^{k_1} C_k}{1 - C_L}, \quad (4.13)$$

$$\rho_m = \rho + \frac{\sigma - \rho}{1 - C_L} \sum_{k=1}^{k_1} C_k = \rho + (\sigma - \rho)C_F, \quad \text{and} \quad (4.14)$$

$$d_{mL} = \frac{\sum_{k=k_1+1}^{k_e} d_k C_k}{C_L}, \quad (4.15)$$

where C_k is the volumetric concentration of grade k particles in the total water and sediment volume. As the particle size composition of the riverbed material is not necessarily the same as that in the flow above the bed, the composition of the flow will be depleted by the transfer of sediment to the riverbed. To determine the particle size composition of runoff sediment, the particle composition of the riverbed, along with the flow exchange particles, must be determined.

Assuming that the total volume of grade k particles on the bed is V_k , the ratio of particles of this grade to the total particles (coarse plus fine) f_{bk} is

$$f_{bk} = \frac{V_k}{V_L + V_F}, \quad (4.16)$$

where V_L and V_F are the total volumes of coarse and fine particles, respectively, and are represented as follows:

$$V_L = \sum_{k=k_1+1}^{k_e} V_k, \quad V_F = \sum_{k=1}^{k_1} V_k. \quad (4.17)$$

The ratio of grade k particles (grade k coarse material) to the total coarse particles f_{bLk} is

$$f_{bLk} = \frac{f_{bk}}{\sum_{k=k_1+1}^{k_e} f_{bk}}. \quad (4.18)$$

The following points about the structure of the bed should be noted. If the total volume of fine particles is small, the coarse particles form a skeleton structure; and if the fine particles are stored

only in the void space, C_{*k} ($k: 1 \sim k_1$) is obtained. If the total volume of the bed is V_V and the volume of the void space is then $V_L + V_V = V$. $V_L/V = C_{*L}$ is obtained, where C_{*L} is equal to the volume concentration of all the coarse particles when the bed is composed of only coarse particles. Consequently,

$$C_{*k} = \frac{V_k}{V_V} = \frac{C_{*L}}{1 - C_{*L}} \frac{V_k}{V_L} = \frac{C_{*L}}{1 - C_{*L}} \frac{f_{bk}}{\sum_{k=k_1+1}^{k_e} f_{bk}}, \quad k = 1 \sim k_1. \quad (4.19)$$

As this formula was deduced assuming that fine particles are stored only in the void space of the framework formed by coarse particles, the formula should become

$$\sum_{k=1}^{k_1} C_{*k} = \frac{C_{*L}}{1 - C_{*L}} \frac{\sum_{k=1}^{k_1} f_{bk}}{\sum_{k=k_1+1}^{k_e} f_{bk}} = \frac{C_{*L}}{1 - C_{*L}} \frac{1 - F}{F} \leq C_{*F}, \quad (4.20)$$

where C_{*F} is the volume concentration of all the fine particles when composed only of fine particles. By introducing the definition of F in equation (4.18) into equation (4.20), equation (4.20) can be rewritten as follows:

$$F = \sum_{k=k_1+1}^{k_e} f_{bk}, \text{ and} \quad (4.21)$$

$$F \geq \frac{C_{*L}}{C_{*F} + C_{*L} - C_{*L}C_{*F}}. \quad (4.22)$$

For simplicity, both C_{*L} and C_{*F} are assumed to be 0.65, so equation (4.22) is rewritten as follows:

$$F \geq 0.74. \quad (4.23)$$

Thus, when the ratio of the fine particles is greater than 26%, coarse particles can no longer form a skeleton and will be scattered among the accumulated fine particles. These fine particles will form a skeletal structure with the volume concentration C_{*F} , but its void space will be too small to store coarse particles. In this case, because $(V - V_L)$ is the bulk volume of fine particles plus the void space between them, the substantial volume of the fine particles V_F is given as follows:

$$V_F = (V - V_L) \cdot C_{*F}. \quad (4.24)$$

The definition of C_{*k} , the volume ratio of grade k particles (grade k signifying fine material), to the volume $(V - V_L)$ is as follows:

$$C_{*K} = \frac{V_k}{(V_F / C_F)} = \frac{V_k C_{*F}}{(V_L + V_F) \sum_{k=1}^{k_1} f_{bk}} = \frac{f_{bk} C_{*F}}{1 - F}. \quad (4.25)$$

Using the relationships of $V_F = (V_L + V_F) (1 - F)$ and $V_L = (V_L + V_F) F$, the volume concentration of the coarse particle fraction on the bed C_{*L} is

$$C_{*L} = \frac{F \cdot C_{*F}}{C_{*F} F + 1 - F}. \quad (4.26)$$

Summarizing the above discussion, the following relationships are obtained as shown in **Figure 4.16**:

1. When $F \geq 0.74$:

Coarse particle concentration: $C_{*L} = 0.65$, and

Fine particle concentration: $C_{*K} = C_{*L} f_{bk} / \{(1 - C_{*L}) F\}$; but

2. when $F < 0.74$:

Coarse particle concentration: $C_{*L} = F C_{*F} / (C_{*F} F + 1 - F)$, and

Fine particle concentration: $C_{*K} = C_{*F} f_{bk} / (1 - F)$.

d. Fundamental equation for prediction of flow in a river channel

The fundamental equations for flow in a channel include the one-dimensional momentum conservation equation of flow and the continuity equations that take erosion and deposition into account.

The continuity equation for the total volume of water plus sediment is

$$\frac{\partial h}{\partial t} + \frac{1}{B} \frac{\partial (qB)}{\partial x} = i_{sb} K_1 + \frac{q_{in}}{B} + i_g K_2 \frac{L}{B}, \quad (4.27)$$

where B is the channel width, q_{in} is the inflow discharge per unit length of channel from bank sedimentation, L is the slope length, i_{sb} is the substantial erosion/deposition velocity, and i_g is the side-shore erosion velocity.

In addition, K_1 is the coefficient given as $C_{*L} + (1 - C_{*L}) \{C_{*F} + (1 - C_{*F}) s_b\}$ when erosion takes place ($i_{sb} > 0$), and $K_1 = 1$ when deposition takes place ($i_{sb} \leq 0$), where s_b is the degree of saturation of the bed. K_2 is the coefficient given as $K_2 = C_{*gL} + (1 - C_{*gL}) \{C_{*gF} + (1 - C_{*gF}) s_g\}$, where C_{*gL} is the volume concentration of coarse particles in the riverbank sediment, s_g is the degree of saturation of the bank sedimentation, and C_{*gF} is the volume concentration of fine particles contained within the skeleton structure of coarse particles in the riverbank sediment.

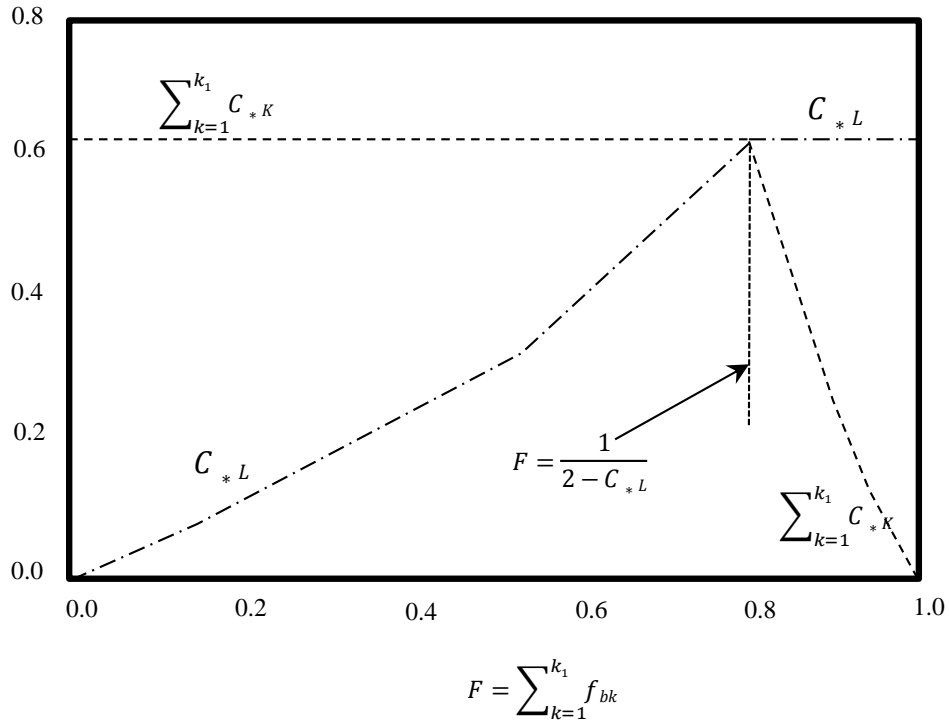


Figure 4.16: Relationship between concentrations of coarse and fine particles on the riverbed.

The inflow discharge per unit length of the channel from the riverbank sediment q_{in} is the inflow discharge from the slope, where the channel width is the flow width, and the sediment yield is supplied directly from the slope. In contrast, the inflow discharge per unit length of channel from the riverbank sediment q_{in} is needed to consider the developing/disappearing processes of sedimentation, *i.e.*, the inflow discharge, given as $i_g K_2 L/B$.

The continuity equation for each particle grade is

$$\frac{\partial(C_k h)}{\partial t} + \frac{1}{B} \frac{\partial(q C_k B)}{\partial x} = \frac{(C_k q_{in})}{B} + i_{sbk} + i_{gk} \frac{L}{B}, \quad (4.28)$$

where i_{sbk} is the erosion/deposition velocity on the riverbed of the k th grade of particles, and i_{gk} is the side-shore erosion velocity of k th grade particles.

The equation for the bed variation is

$$\frac{\partial z}{\partial t} + \frac{B}{B_0} i_{sb} = \frac{C_{*L} q_{in}}{B_0} + i_g \frac{L}{B_0}, \quad (4.29)$$

where z is the depth of sediment on the bed. In addition, when the valley bottom width B_0 is different from the stream channel width B , the erosion velocity becomes B/B_0 times that of the case where $B_0 = B$.

e. Erosion and deposition velocity

In general, the erosion of the bed is due to the scouring of individual particles from the bed surface by the effects of shear stress generated. Shear stress will become too weak to pick up particles at the point when the sediment concentration in the flow attains full equilibrium. Therefore, erosion of the bed continues as long as the sediment concentration in the flow is less than the equilibrium value. Analogous to the non-equilibrium bed load transportation formula, the following erosion velocity equation is assumed:

$$\frac{i_{sb0}}{\sqrt{gh}} = K \sin^{3/2} \theta_w \frac{\rho_m}{(\sigma - \rho_m)} \cdot \left(\frac{C_{L\infty} - C_L}{C_{L\infty}} \right)^{3/2} \frac{h}{d_{mL}}, \quad (4.30)$$

where K is a coefficient, i_{sb0} is the erosion/deposition velocity of one particle diameter, and $C_{L\infty}$ is the equilibrium concentration at that point.

In mature and immature debris flows, the largest particle that can be moved due to the effect of surface flow is assumed to have a diameter that is the same as the depth of flow. Under this assumption, if $d_{k_{2+1}} > h \geq d_{k_2}$ is satisfied, the ratio of erodible coarse sediment to all coarse particles K_3 is as follows:

$$K_3 = \sum_{k=k_1+1}^{k_2} f_{bLk}. \quad (4.31)$$

The substantial volume of coarse particles belonging to grades $k_1 < k \leq k_2$ is as follows:

$$\frac{V_k}{V} = \frac{C_{*L} V_k}{V_L} = C_{*L} f_{bLk}. \quad (4.32)$$

The erosion velocity for each particle grade when $d_{k_{2+1}} > h \geq d_{k_2}$ is as follows:

$$\left. \begin{array}{ll} k_1 < k \leq k_2 & ; \quad i_{sbk} = K_3 f_{bLk} C_{*L} \\ k > k_2 & ; \quad i_{sbk} = 0 \end{array} \right\}. \quad (4.33)$$

Under the bed load transport type ($\tan\theta < 0.03$), the critical tractive force of flow determines the size of the erodible particles on the bed and the erosion velocity of particles larger than that size is zero.

The erosion velocity of fine particles ($k \leq k_1$) is given as follows:

$$i_{sbk} = i_{sb0} K_3 (1 - C_{*L}) C_{*k}. \quad (4.34)$$

When the volumetric concentration of coarse particles in the flow C_L at a certain position is larger than the equilibrium concentration $C_{L\infty}$ at that position, the coarse particles will be deposited on the riverbed. The bulk deposition velocity i_{sb0} will be given, neglecting the effect of inertial motion, as follows:

$$i_{sb0} = \delta_d \frac{C_{L\infty} - C_L}{C_* h} \frac{q}{h}, \quad (4.35)$$

where δ_d is a coefficient of the deposition velocity.

The deposition velocity of each coarse particle grade i_{sbk} is given as follows:

$$i_{sbk} = i_{sb0} \frac{C_k}{C_L} C_{*L\max} \quad (k > k_1), \quad (4.36)$$

where $C_{*L\max}$ is the volume concentration of the coarse particles in the maximum compacted state.

If the settling due to its own density is neglected, the fine particle fraction mixed with water in the flow is considered to constitute a fluid phase and it becomes trapped within the voids of the coarse particles' skeleton produced by the deposition of coarse particles. Then, the deposition velocity for fine particles i_{sbk} is as follows:

$$i_{sbk} = i_{sb0} \left(1 - C_{*L\max}\right) \frac{C_L}{1 - C_L} \quad (k \leq k_1). \quad (4.37)$$

However, at an estuary or immediately upstream of a check dam, if the shear velocity at a position is less than the settling velocity w_{0k} of the k th grade particle, deposition due to particle settling will also arise. In such a case, the deposition velocity for a fine particle i_{sbk} is as follows:

$$i_{sbk} = -w_{0k} C_k + i_{sb0} \left(1 - C_{*L\max}\right) \frac{C_L}{1 - C_L}. \quad (4.38)$$

The settling velocity can also be taken into account for coarse particles.

Consequently, the erosion/deposition velocity in bulk that includes a void space i_{sb} is given as follows:

$$i_{sb} = \frac{1}{C_{*L\max}} \sum_{k=k_1+1}^{k_e} i_{sbk} + \frac{1}{C_{*F\max}} \sum_{k=1}^{k_3} (-w_{0k} C_k), \quad (4.39)$$

where k_3 is the largest particle grade that satisfies $u_* < w_{0k}$, and $C_{*F\max}$ is the volume concentration of the fine particles in the maximum compacted state.

The surface slope angle of the side-bank sedimentation is the same grade as the internal friction angle of the particle; the sedimentation is initiated due to slope failure. The talus sedimentation is then

eroded due to the flow with riverbed erosion.

Assuming that the side-shore velocity is the same as the erosion velocity i_{sb} of the riverbed for simplicity, the erosion velocity i_g of the side-bank sedimentation is as follows:

$$i_g = \frac{1}{2} i_{sb}. \quad (4.40)$$

In addition, the erosion velocity i_{gk} of the particle diameter d_k is as follows:

$$i_{gk} = i_g \frac{f_{gk}}{\sum_{k=k_1+1}^{k_e} f_{gk}} C_{*gL}, \quad (4.41)$$

and the erosion velocity i_{gk} of the fine particles d_k is as follows:

$$i_{gk} = i_g (1 - C_{*gL}) \cdot C_{*gk}, \quad (4.42)$$

where f_{gk} is the ratio of grade k particles to the total particles, and C_{*gL} is the volume concentration of all the coarse particles.

The volume ratio of the fine particles to the volume of the void space in the sedimentation C_{*gk} is as follows:

$$C_{*gk} = \left(\frac{C_{*gL}}{1 - C_{*gL}} \right) \frac{f_{gk}}{\sum_{k=k_1+1}^{k_e} f_{bk}}. \quad (4.43)$$

f. Particle diameter change in the riverbed

Prior to predicting long-term sediment runoff, consideration of the particle diameter change in the riverbed due to erosion and deposition of the flow is important. As shown in **Figure 4.17**, the deposit layer is assumed to be divided into segments of equal thickness δ_s . Assuming that the riverbed exists in the m th, the depth of the m th segment δ_a is as follows:

$$\delta_a = (z - z_s) - (m - 1) \cdot \delta_s, \quad (4.44)$$

where z_s is the height of the fixed bed from base level, and m is the number of the layers deposited.

For the deposition time Δt on the riverbed, the bulk volume of the total particles in the m th layer is $(\delta_a \Delta x B_0 J_0) + (-i_{sb} \Delta t \Delta x B J)$. In addition, the bulk volume of the grade k particles in the m th layer is $(\delta_a \Delta x B_0 J_0 f_{0k}) + (-i_{sb} \Delta t \Delta x B J f_{bk})$. Hence, the ratio of grade k particles to the total particles in the m th layer f_{0knew} is as follows:

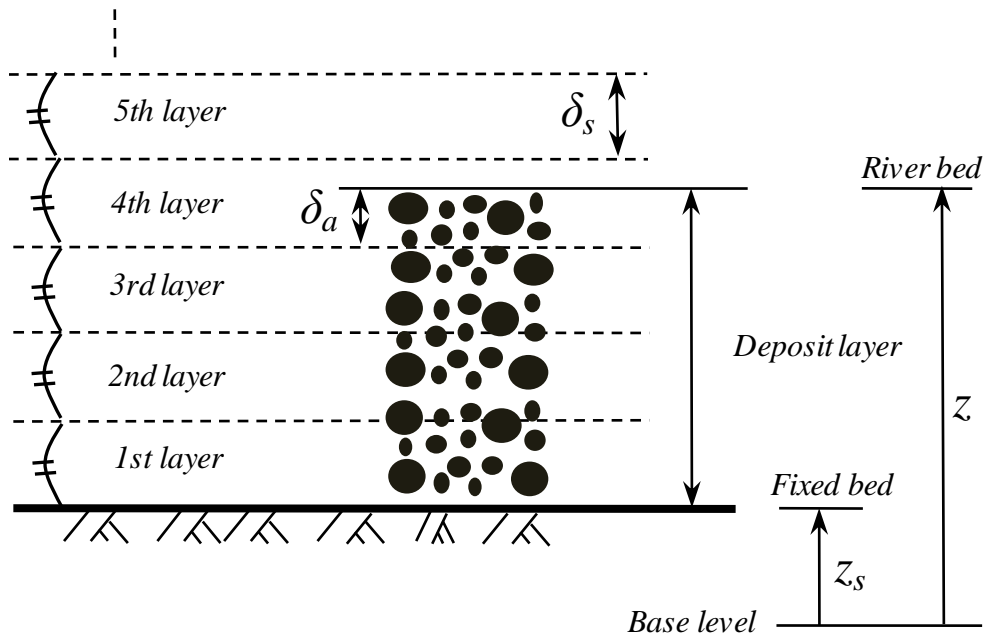


Figure 4.17: Schematic of the riverbed deposit model.

$$f_{0knew} = \frac{\delta_a \Delta x B_0 J_0 f_{ok} - i_{sb} \Delta t \Delta x B J f_{bk}}{\delta_a \Delta x B_0 J_0 - i_{sb} \Delta t \Delta x B J} = \frac{\delta_a J_0 f_{ok} - i_{sb} \Delta t (B / B_0) J f_{bk}}{\delta_a J_0 - i_{sb} \Delta t (B / B_0) J}, \quad (4.45)$$

where J and J_0 is the ratio between the real volume and entire volume, including void spaces.

g. Developing and disappearing processes of sedimentation

In general, sediment yield due to slope failure composes sedimentation in the riverside, not flow into the channel directly. Assuming that the sediment flow into the channel is through the developing/disappearing processes of sedimentation on the riverside, as shown in **Figure 4.18**, $(C_k q_m) B^{-1}$ is omitted from equation (4.28).

The continuity equation of unit length for the total volume of the sediment is as follows:

$$\frac{\partial S}{\partial t} + q_{sgin} - q_{sgout} = 0, \quad (4.46)$$

where S is the cross-sectional area of the sediment.

Equation (4.40) is rewritten as follows:

$$q_{sgout} = \frac{1}{2} i_g L, \quad (4.47)$$

where q_{sgout} is the sediment discharge into the channel from the riverbank.

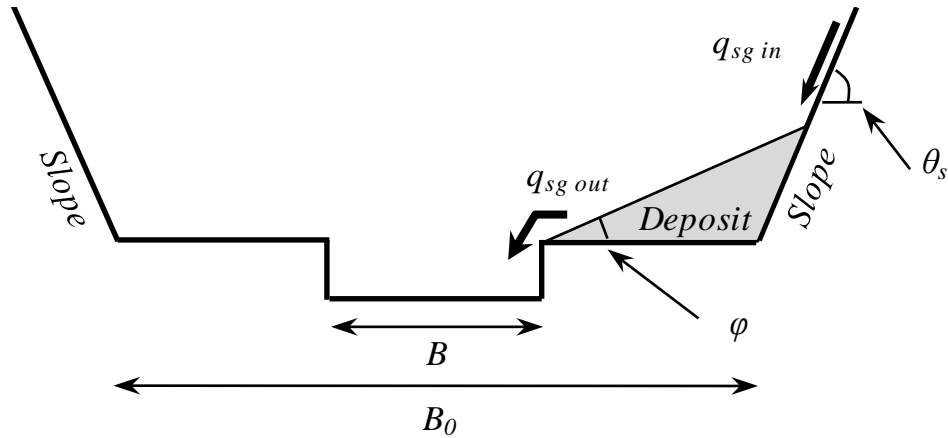


Figure 4.18: Schematic of developing/disappearing processes of sedimentation.

Hayami *et al.* (2012) suggested that slope failure is affected more by short-term rainfall than long-term rainfall in mountainous areas, which yield more sediment than other areas, considering sediment yield processes.

Here, the sedimentation yield due to slope failure corresponds to the area of the bare-ground slope when precipitation exceeds a certain critical threshold. The unit length sediment discharge of the sediment yield due to slope failure q_{sgin} is as follows:

$$q_{sgin} = kr_0 A_h / l_g, \quad (4.48)$$

where k is a coefficient, r_0 is the precipitation exceeding the critical line, A_h is the area of bare-ground slope, and l_g is the channel length corresponding to the adjacent slope. Further work is needed to identify the slope failure processes due to rainfall based on observation.

4.3.2. Calculation conditions

The flood runoff, sediment runoff, and riverbed variation in a mountainous area (Jintuu River, Ashiaraidani basin), which has a basin area of approximately 6.5 km², were calculated using the developed numerical model based on Hirasawa *et al.* (2012). Comparison between the calculated and observed data, which had been continually measured in the field, confirmed its validity. The preceding model for the area (Hirasawa *et al.*, 2012) assumed an invariable channel width in the sub-basin, neglecting the differences in channel width, and did not consider the sediment yield due to the slope failure.

The bare ground slope and channel width were established using aerial photography and topography. A part of the channel width, which was not recognizable in the initial data, was estimated using the relationship ($\beta = 8.0$: geology and vegetation condition in the field) between the channel

width and area of the upper basin (**Section 4.2**). The relationship between the calculated and observed results confirmed its validity.

Figure 4.19 shows the basin area and bare-ground slopes; **Figure 4.20** shows the arrangement of slopes in the simulation; and **Figure 4.21** shows the arrangement of the calculation points. Here, the study period was from April to October 2012. The observed bed load measurement data of sediment discharge were estimated using hydrophones. The relationship between total rainfall intensity and rainfall loss in the area (Hirasawa *et al.*, 2012), as shown in **Figures 4.22** and **4.23**, was used to estimate the effective rainfall intensity. In addition, the base discharge ($\sim 1.0 \text{ m}^3 \text{ s}^{-1}$ at point NO. 1) was considered as a surrogate for rainfall loss.

Tables 4.22 and **4.23** show the parameters used in the calculation and the parameters referenced from previous studies (Hirasawa *et al.*, 2012).

Table 4.22: Parameters used in the calculation.

β	h_0 (cm)	δ_s (cm)	σ (kg/m ³)	C_*	Δt (s)
8.0	300	50	2650	0.6	0.2 – 5.0

Table 4.23: Parameters used in the calculation.

ρ (kg/m ³)	g (m s ⁻²)	δ_e	δ_d	n_m (m ^{-1/3} s)	n_e
1000	9.8	0.005	0.0002	0.003 – 0.05	1.0

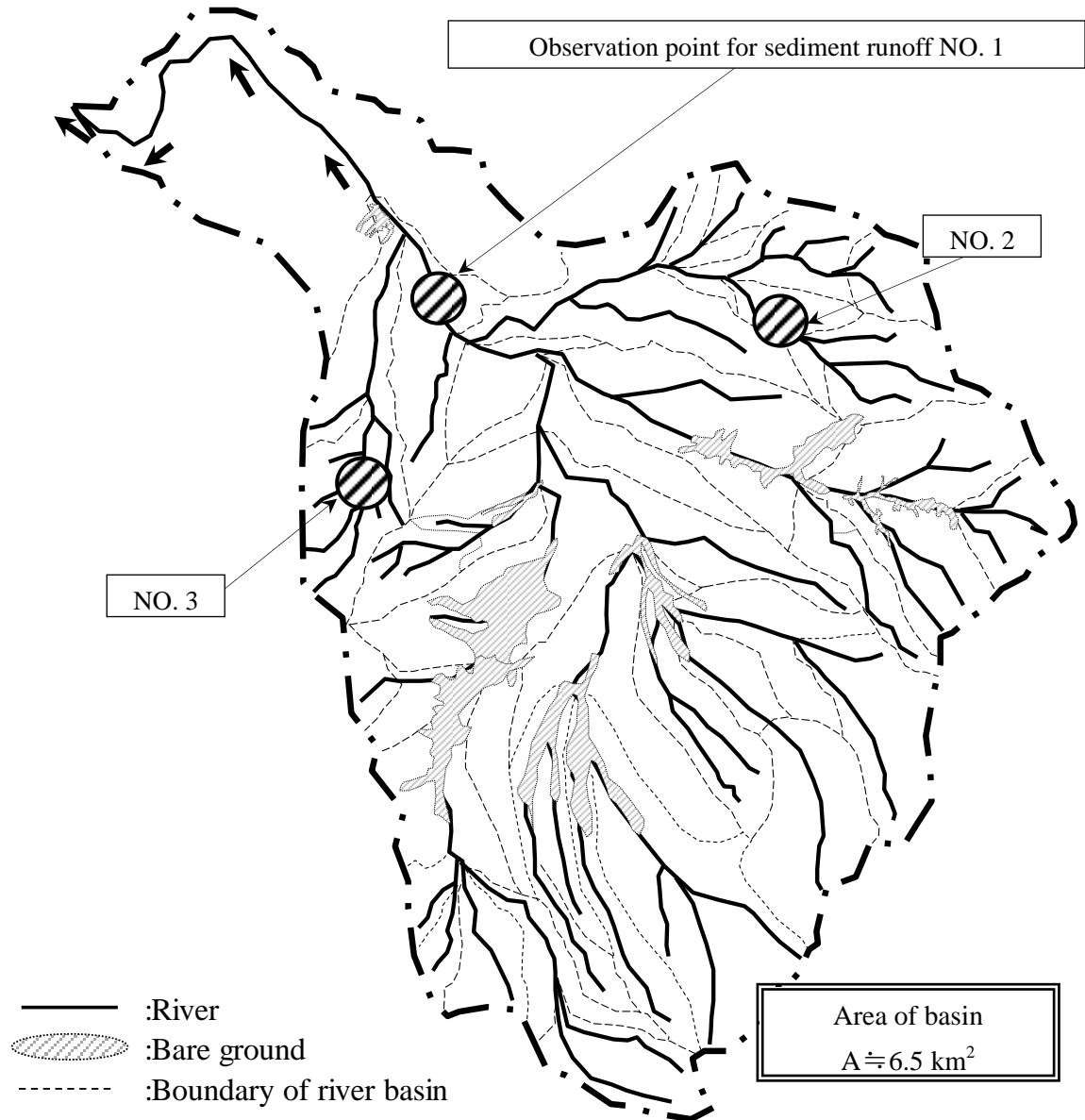


Figure 4.19: Schematic map of the basin area and bare ground slopes.

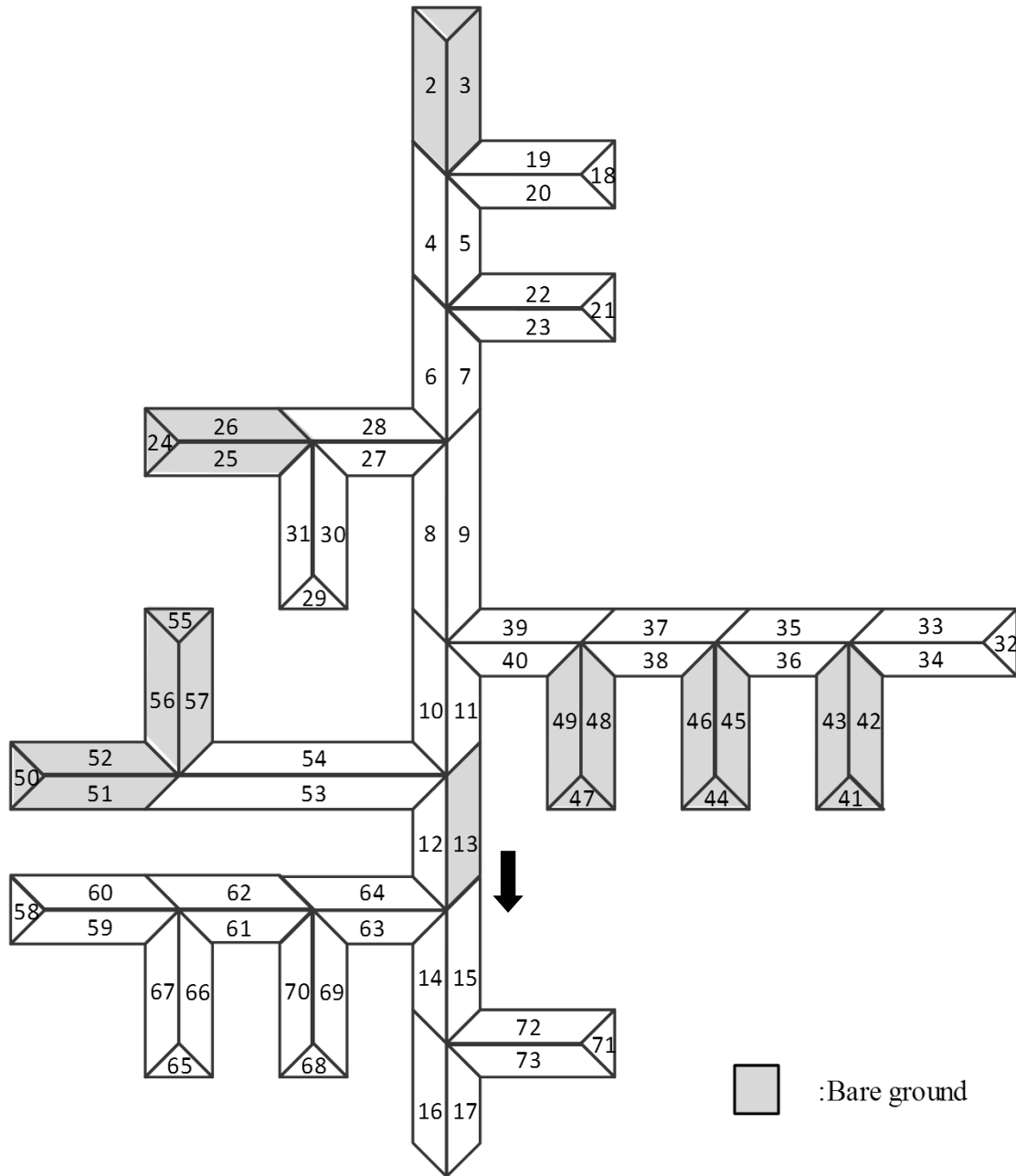


Figure 4.20: Arrangement of slopes in the simulation.

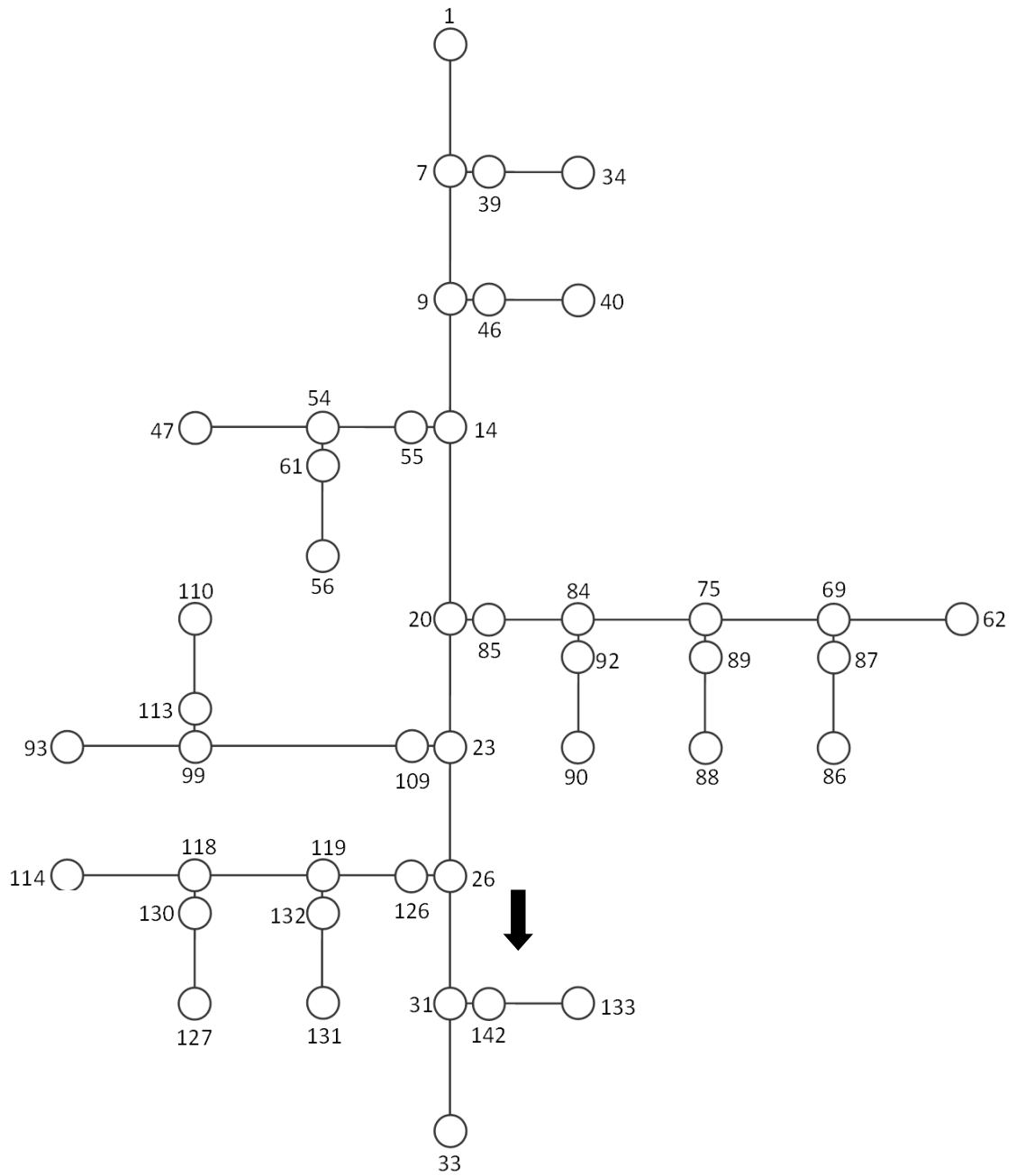


Figure 4.21: Arrangement of the calculation points in the simulation.

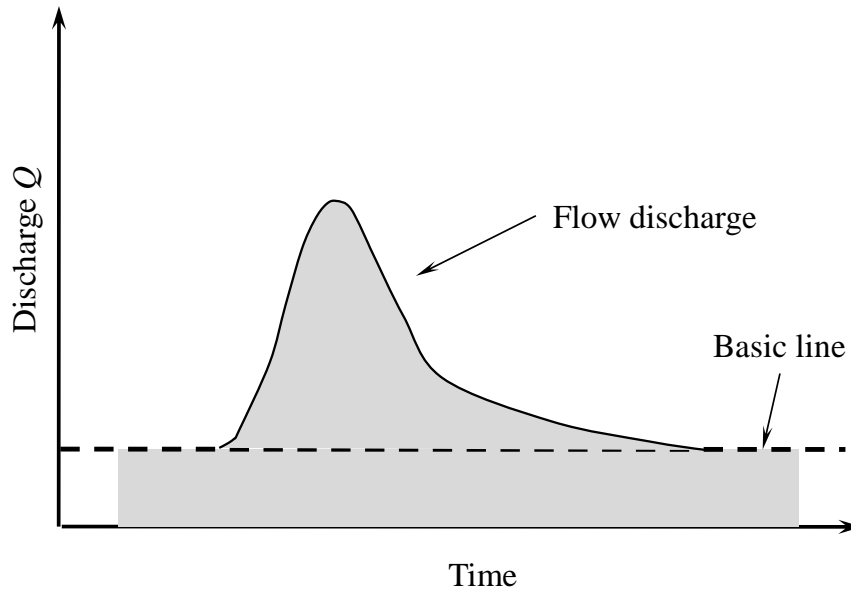


Figure 4.22: Schematic of the relationship between flood discharge and base discharge.

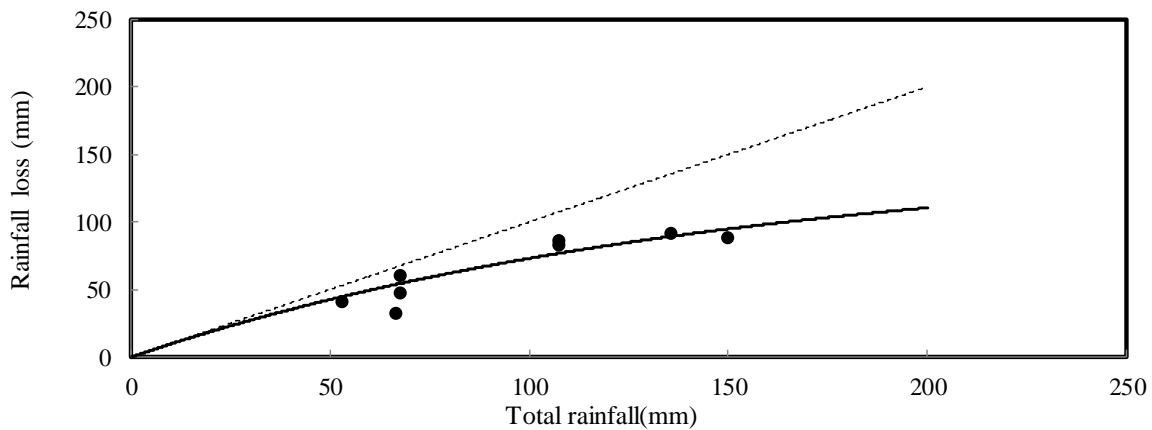


Figure 4.23: Relationship between total rainfall intensity and rainfall loss (Hirasawa *et al.*, 2012).

4.3.3. Comparison between observed and calculated results of sediment runoff

To confirm the validity of the numerical model, **Figure 4.24** shows the comparison between the observed and calculated results of the flood runoff discharge at the NO.1 observation point, as shown in **Figure 4.19**, in a mountainous area during a heavy rainy season. The model almost exactly simulated the flood runoff discharge shown in **Figure 4.24**. However, the comparison showed some differences because the roughness coefficient assumed for the mountainous slope was inadequate as it did not account for topographic conditions.

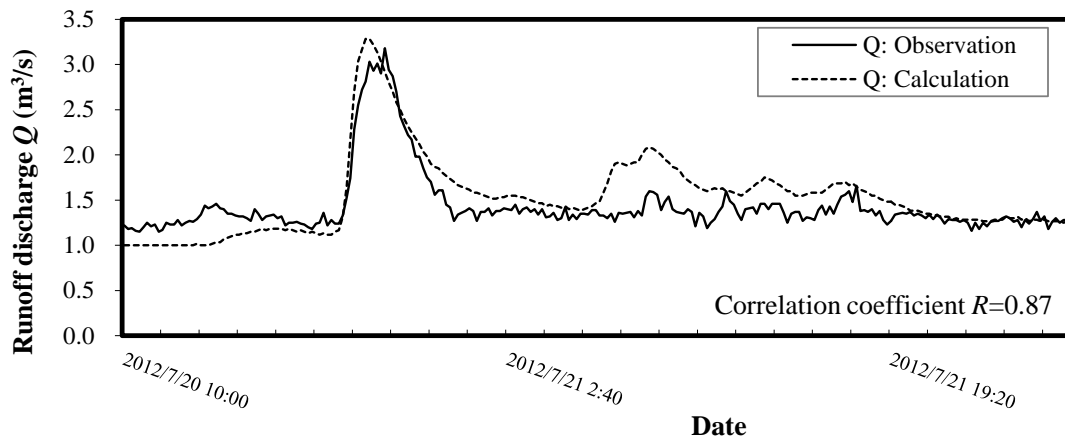


Figure 4.24: Comparison between results of analysis and observational data of the flood runoff discharge at observation point NO. 1.

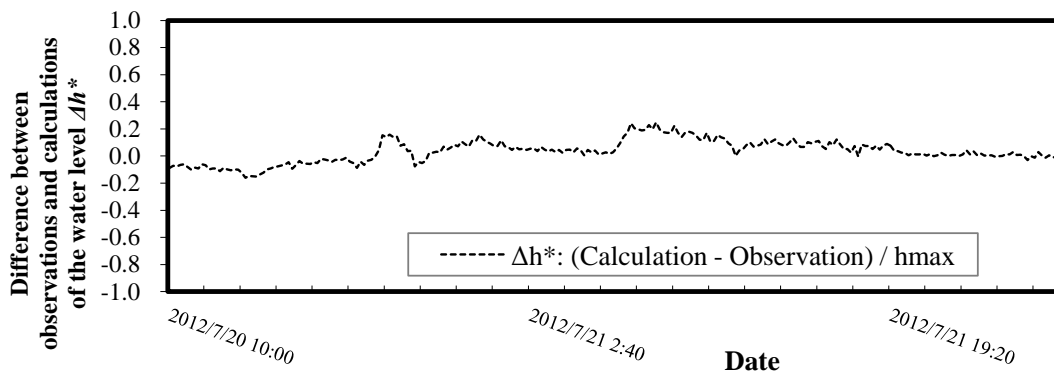


Figure 4.25: Comparison between results of analysis and observational data of the water level at observation point NO. 1.

Figure 4.25 shows a comparison between the observed and calculated results of the water level at observation point NO. 1 for the same period. In addition, the water level was described as the non-dimensional water level. As shown in **Figure 4.25**, the model almost exactly simulated the water level, even taking riverbed variation into consideration.

Figure 4.26 shows a comparison between the observed and calculated results of the cumulative sediment discharge at observation point NO. 1, as shown in **Figure 4.19**, in a mountainous area. The model almost correctly simulated the sediment discharge, as shown in **Figure 4.26**; the accumulated sediment discharge using the preceding model (Hirasawa *et al.*, 2012), which did not consider sediment yield processes due to slope failure, was approximately 15,000 m³. However, the comparison showed some differences because the roughness coefficient of the mountainous slope was assumed, and did not consider the changes in particle diameter due to wear produced by the runoff.

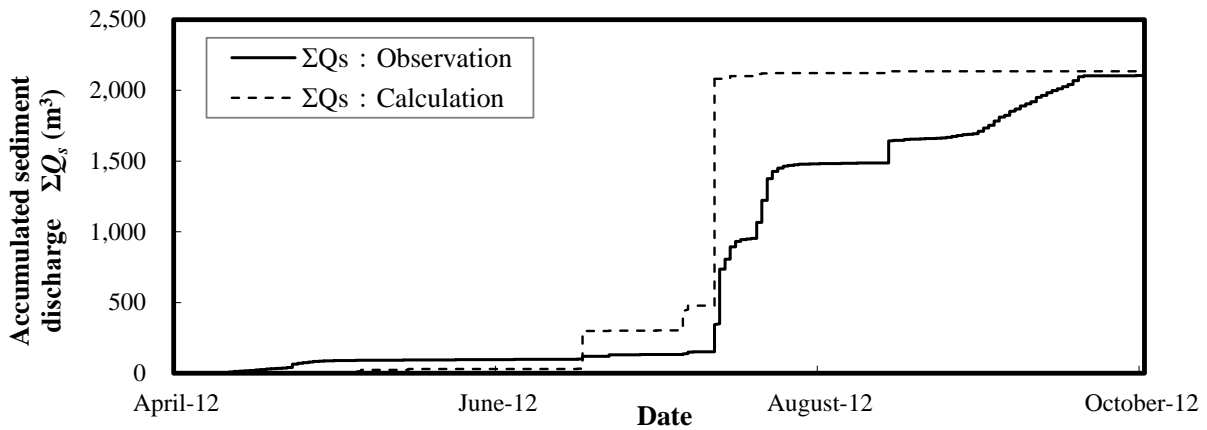


Figure 4.26: Comparison between results of analysis and observational data of the cumulative sediment discharge at observation point NO. 1.

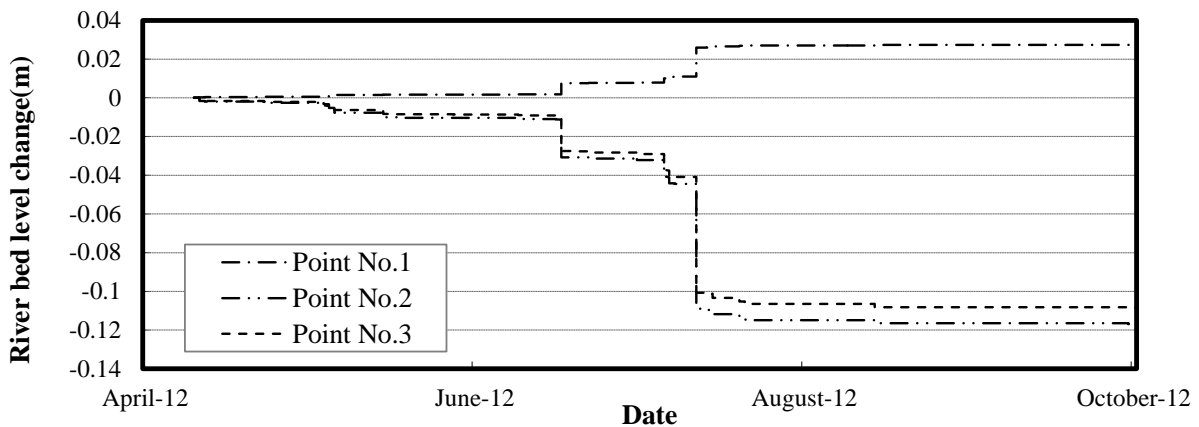


Figure 4.27: Prediction of riverbed variation at observation points NOs. 1, 2, and 3.

In reference to the calculated result using the model, **Figure 4.27** shows the riverbed variations using the numerical model at the observed points (NOs. 1, 2, & 3), as shown in **Figure 4.19**. However, these calculated results could be not verified by the observational results. Further studies are needed to verify the relationship between the calculated and observed data.

4.4. Summary

To confirm the validity of the developed numerical model, which predicted the flood and sediment runoff using the rainfall intensity conditions, the relationship was compared between the calculated and observed data for a mountainous area.

Considering the geology and vegetation in the basin area, the relationship between the channel width and area of the upper basin was inferred using regression analysis; the calculated results were

verified by comparison with the observation data in the field.

A numerical model was developed with consideration of the sediment yield due to slope failure, based on Hirasawa *et al.* (2012). In addition, using the proposed relationship between the channel width and area of the upper basin corrected the channel width in the sub-basin area. Comparison between the calculated and observed data suggested that it is necessary to consider the sediment yield in the rainfall–runoff prediction in mountainous areas, which yield more sediment than other areas.

BIBLIOGRAPHY

1. Araki K & Yonese Y. 2008. Flood forecasting system that uses radar rain data and distributed runoff model. *Advance in River Engineering*, Vol. 14: 31-34.
2. Hashimoto H, Park K, Takaoka H & Arasawa M. 2003. Runoff analysis of sediment and water due to heavy rain from a mountain river drainage. *Annual Journal of Hydro science and Hydraulic Engineering*, Vol. 47: 745-750.
3. Hayami S & Satofuka Y. 2013. Observation of moisture changes in the deposit on riverbed and sediment movement in the mountainous watershed. *Annual Journal of Hydro science and Hydraulic Engineering*, Vol. 69: 943-948.
4. Hirasawa Y, Satofuka Y, Mizuyama T & Tutumi D. 2012. Development and application of a sediment runoff from a mountain watershed simulator (SERMOW-II). *Journal of the Japan Society of Erosion Control Engineering*, Vol.64: 32-37.
5. Mouri G, Shibata M, Hori T & Ichikawa Y. 2003. Modeling of water and sediment dynamic in the basin scale and its application to the actual basin. *Annual Journal of Hydro science and Hydraulic Engineering*, Vol. 47: 733-738.
6. Ozawa K, Nagatani G, Mizuno N, Takata Y, Ishida H & Takara K. 2011. A study on sediment yield and transport properties at basin scale using a distributed rainfall and sediment runoff model. *Advance in River Engineering*, Vol. 17: 59-64.
7. Shiga prefecture. 2011. Investigation report for the maintenance of landslide disaster area data.
8. Takahashi T, Inoue M, Nakagawa H & Satofuka Y. 2000. Prediction of sediment runoff from a mountain watershed. *Annual Journal of Hydro science and Hydraulic Engineering*, Vol. 44: 717-722.
9. Takahashi T & Nakagawa H. 1991. Prediction of stony debris flow induced by severe rainfall. *Journal of the Japan Society of Erosion Control Engineering*, Vol.44: 12-19.
10. Takahashi T, Nakagawa H, Satofuka Y & Suzuki N. 1999. Prediction model for sedimentation runoff due to heavy rainfall. *Advance in River Engineering*, Vol. 5: 177-182.

Chapter 5

Debris Flow Control by Steel-grid SABO Dams

“Wisdom makes one wise person more powerful than ten rulers in a city.”

Ecclesiastes 7:19

5.1. Introduction

Debris flows in mountainous areas pose a threat to property and human well-being. Technologies such as steel-grid SABO dams are intended to mitigate these risks by controlling debris hazards in areas threatened by sediment flows. However, the exact mechanisms by which steel-grid SABO dams mitigate debris hazards is not fully understood, as reported by Hashimura *et al.* (2012).

According to the design code of steel-grid SABO dams (Japanese government, 2007), the permeable width of the barricade must be the same size as the D_{95} , which is the particle diameter equivalent to 95% of debris accumulation based on the frequency distribution of sediment sizes within a stream. Consequently, the permeable width of the barricade is determined not by considering particles under the 95% size distribution curve based on the particle diameter frequency distribution, and not by the grain-size accumulation rate (which is the relationship between the particle diameter and passage weight percentage). In contrast, the former SABO dam design code (2000) ascribes the permeable width of the barricade as 1.5–2.0-fold that of the large particle diameter D_{95} . Hence, the width determined by the former design code (2000) is wider than that of the new code (2007). For this

design code transition, determining the debris capture rate of steel-grid SABO dams is critical in terms of outlining how well these dams control potentially damaging sediment flows.

How steel grid SABO dams capture debris-flow sediment has been previously investigated: Ashida *et al.* (1987), Mizuyama *et al.* (1995), Mizuno *et al.* (2000), and Takahashi *et al.* (2001). Ashida *et al.* (1987) proposed a probability model that predicts the sediment volume that flows out of the SABO dam grid. Mizuyama *et al.* (1995) considered the relationship between the SABO dam function and the characteristics of debris flow. Mizuno *et al.* (2000) analyzed the movement of each particle using the distinct element method. Takahashi *et al.* (2001) developed a numerical model that considers the momentary blockage-probability of a SABO dam. Additionally, Takahashi *et al.* (2001) showed the relationship between the permeable width of the barricade and the coarse particle diameter using blockage mechanisms provided by the arch action of coarse particles, as shown in **Figure 5.1**.

Referencing the steel-structure, Yazawa *et al.* (1986) proposed a new method to control debris flow using a steel-grid constructed under a riverbed, which separates water and sediment in debris flowing through the grid. No study has reported the capture mechanisms of the grid SABO dam, considering the details behind the capture rate, such as differences in the cross-section type of grid, or the barricade incline of the riverbed, as well as verifying the applicability of the permeable width of the barricade as determined by the SABO dam design code (Japanese government, 2000 & 2007).

To identify the ideal structure for controlling debris flow, the capture rate of a small grid dam in a laboratory flume was observed by varying several design parameters, such as the permeable width of the barricade, the cross section of the grid component and the barricade incline of the riverbed. By calculating the capture rate under these conditions, the ideal permeable width of the barricade was determined by identifying the necessary volume concentration of the particle (which determines the grid size) within a debris flow.

Finally, to evaluate the capture rate of a grid SABO dam designed according to code (2000), taking into consideration different particle size distributions, the grid size was altered according to the various particle size distribution curves.

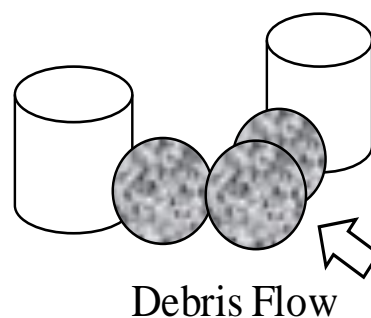


Figure 5.1: Mechanisms of capture by the arch action of steel-grid SABO dams (Takahashi *et al.*, 2001).

5.2. Ideal structure of a grid SABO dam for controlling sediment runoff

To identify factors that affect the capture rate of the grid SABO dam, the experiments were conducted on a laboratory flume by varying several operational parameters.

5.2.1. Materials and Methods

Figure 5.2 shows the experimental flume apparatus. The experimental waterway, which was 10 cm in height and width and 100 cm in length, was constructed and incorporated a small grid SABO dam barricade at the downstream point.

Sediment with a particle diameter of ~ 7 mm (as separated by a sieve), was used to fill the waterway-bed. Water containing stones was allowed to flow through the apparatus, emulating natural flows of sediment in water as would occur due to water movement. The weight of both particles captured by the barricade and particles flowing out of the barricade were recorded. Various dam design parameters were altered to determine the impact on the capture rate, which is the relationship between the weight of grit blockaded by the obstacle grid and the weight of grit supplied from the upper point. These parameters include the type of dam (vertical grid, horizontal grid or mesh grid), as shown in **Figure 5.3**; cross section type of grid component (square or circle), as shown in **Figure 5.3** (upper left); the permeable width of the barricade (grid size); the barricade incline of the riverbed, as shown in **Figure 5.4**; and changing to a front-bar type of grid (where the vertical and horizontal components are arranged on the upstream, debris flow side), as shown in **Figure 5.3** (upper right).

Finally, the effect on capture rate of the volume concentration of the sediment under debris flow (necessary sediment concentration for the blockage by barricade) was discussed.

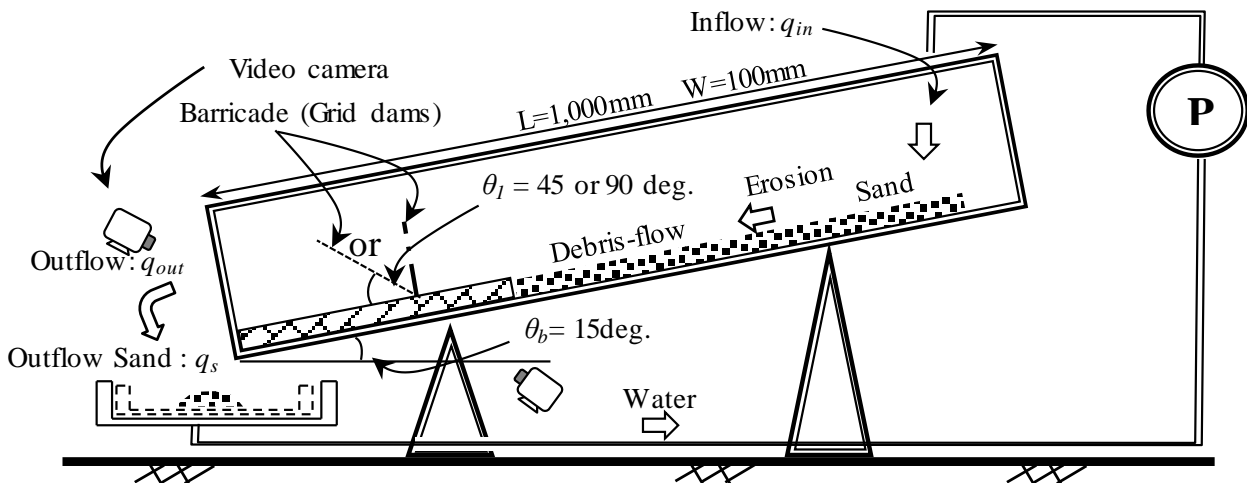


Figure 5.2: Diagram of the experimental model.

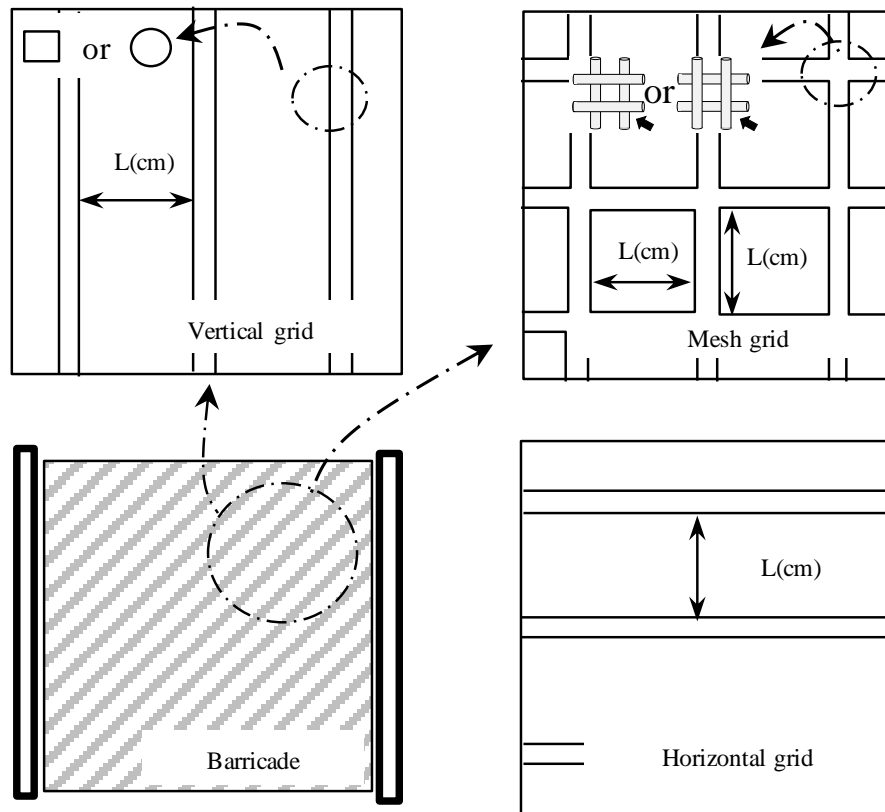


Figure 5.3: Dam type (vertical grid, horizontal grid or mesh grid) and cross-section type of the grid component (square or circle) used in the experimental case study.

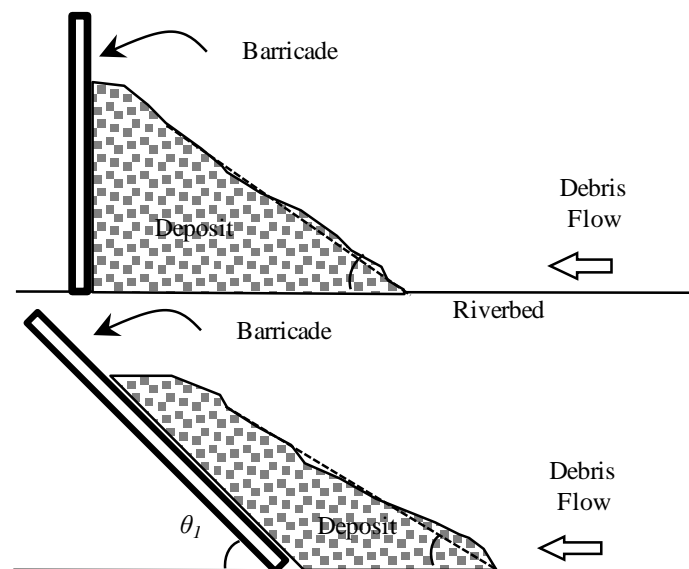


Figure 5.4: Barricade incline of the riverbed used in the experimental case study.

Tables 5.1, 5.2 and 5.3 show the case study optimized by considering performance parameters.

Table 5.1: Experimental case study (NO. 1).

	$\theta_l(^{\circ})$	$L(*d)$	Dam type	Grill type	Front bar type	$Q(\ell/s)$	
1-1	90	1.5	Gr.	□	Ver.	0.72	
1-2					Hor.		
1-3				○	Ver.		
1-4			Hor.	□	-		
1-5							
1-6			Ver.	○			
1-7		2.0	Gr.	□	Ver.		
1-8			Ver.		-		
1-9			Hor.				
1-10			Ver.	○			
1-11		2.5	Gr.	□	Ver.		0.95
1-12		1.0					
1-13		2.5					
1-14		2.5					
1-15		2.0					

Gr.: Mesh grid, Hor.: Horizontal (grid), Ver.: Vertical (grid), □ : Square & ○: Circle component

Table 5.2: Experimental case study (NO. 2).

	$\theta_l(^{\circ})$	$L(*d)$	Dam type	Grill type	Front bar type	$Q(\ell/s)$
2-1	45	1.5	Gr.	□	Ver.	0.72
2-2			Ver.		-	
2-3			Hor.			
2-4			○			
2-5		2.0	Gr.	□	Ver.	
2-6			Ver.		-	
2-7		1.0	Hor.			
2-8		1.5	Gr.		□	
2-9	2.0					
2-10	45	1.5	Hor.	-	0.50	
2-11						
2-12	90	2.0	Gr.	□	Ver.	0.50

Table 5.3: Experimental case study (NO. 3).

	θ_1 (°)	$L(*d)$	Dam type	Grill type	Front bar type	V_L/V_S (kg/kg)	Q (ℓ/s)
3-1	90	2.0	Gr.	□	Ver.	0.8/0.2	0.72
3-2						0.6/0.4	
3-3						0.4/0.6	
3-4						0.2/0.8	
3-5						0.3/0.7	
3-6						0.5/0.5	0.50
3-7							0.95
3-8							0.72
3-9	1.5						
3-10	45	2.0				0.95	
3-11		1.5				0.50	
3-12						0.72	
3-13	90	2.0				Mix ¹⁾	0.72

*1: $d \doteq 1, 3.5, 7 \text{ \& } 10$ mm (one-fourth).

θ_1 is barricade incline of the riverbed, as shown in **Figure 5.4**. $L(*d)$ is the permeable width of the barricade (the ratio between the permeable width and the particle diameter d , where $d = 7$ mm); dam type is the type of grid structure (vertical grid, horizontal grid or mesh grid); grill type is the cross section type of the grid component (square or circle, upper left); front-bar type is the grid component type for upstream (the difference between vertical component and horizontal component arranged to upstream, debris flow side) as shown in upper right (all shown in **Figure 5.3**), V_L/V_S is the ratio between the coarse particle (V_L) and fine particle (V_S) weights of the case study (from CASE 3-1 to CASE 3-12); and Q is the water discharge. Additionally, four particle diameters ($d =$ approximately 1, 3.5, 7, & 10 mm) were used to fill the water-way bed at the same ratio (one-fourth) as in CASE 3-13.

The blockade of the small grid SABO dam was recorded using video cameras. During this time, water flowed continually for 3 seconds after the blockade of the barricade in order to better understand the deformation of the deposit caused by erosion due to overtopping after the dam became blocked with sediment.

5.2.2. Ideal structure of grid SABO dam

The experiment was repeated three times under one condition, considering the inhomogeneous of the particle distribution under debris flow. **Table 5.4** shows the experimental results of capture rate by the barricade.

Table 5.4: Experimental results of the capture rate (%).

	1 st	2 nd	3 rd		1 st	2 nd	3 rd
1-1	96	96	96	2-6	0	0	0
1-2	94	94	96	2-7	96	95	95
1-3	96	96	96	2-8	6	2	4
1-4	82	86	86	2-9	88	88	88
1-5	92	90	90	2-10	8	38	8
1-6	90	90	94	2-11	76	88	82
1-7	90	86	90	2-12	94	94	94
1-8	72	74	82	3-1	74	74	72
1-9	0	0	0	3-2	58	70	60
1-10	24	52	32	3-3	50	0	34
1-11	38	36	42	3-4	0	0	0
1-12	96	96	98	3-5	0	0	0
1-13	62	58	44	3-6	60	58	60
1-14	4	30	16	3-7	60	60	56
1-15	56	54	62	3-8	52	56	54
2-1	94	94	96	3-9	62	48	60
2-2	80	44	82	3-10	6	16	16
2-3	62	74	58	3-11	52	46	56
2-4	10	70	22	3-12	68	58	68
2-5	90	90	76	3-13	61	54	63

To clarify how the capture rate is affected by the design, **Figures 5.5 to 5.10** show the difference between measured capture rates, including each trial and the average capture rate, as well as the non-dimensional capture rate, which was normalized according to the maximum capture rate under the same design condition. **Figure 5.5** shows the capture rate when the incline of the barricade was set at a 90 ° angle with the riverbed, and **Figure 5.6** shows the capture rate when the incline of the barricade was 45 ° to the riverbed using various grid types. Dam design (as shown in **Figure 5.3**) did not affect capture rate, as shown in **Figure 5.5**. In contrast, experimental results suggested that the vertical component strongly contributed to blockage of the dam under experimental conditions (with a grid size twofold larger than the particle diameter) when the horizontal component was absent, as shown in **Figure 5.5**. In terms of the effect of barricade incline on sediment capture, the vertical-incline barricade ($\theta_1 = 90^\circ$) captured more sediment particles than the diagonal-incline grid ($\theta_1 = 45^\circ$), as shown in **Figures 5.5 and 5.6**; only the vertical or horizontal component of the dam (non mesh-grid types; $\theta_1 = 45^\circ$) did not capture particles (with a grid size twofold larger than the

particle diameter), as shown in **Figure 5.6**.

Figure 5.7 shows the relationship between the permeable width of the barricade (mesh grid) and the capture rate. The capture rate was ~85% greater when the permeable width of the barricade was less than twofold the particle diameter, as shown in **Figure 5.7**. In contrast, the capture rate was ~39% when the permeable width of the barricade was 2.5-fold the particle diameter, as shown in **Figure 5.7**.

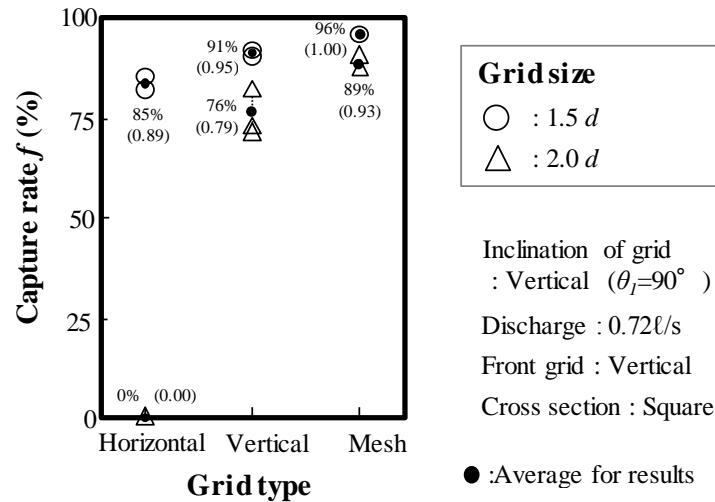


Figure 5.5: Effect of grid type on the capture rate (incline of the dam = 90°).

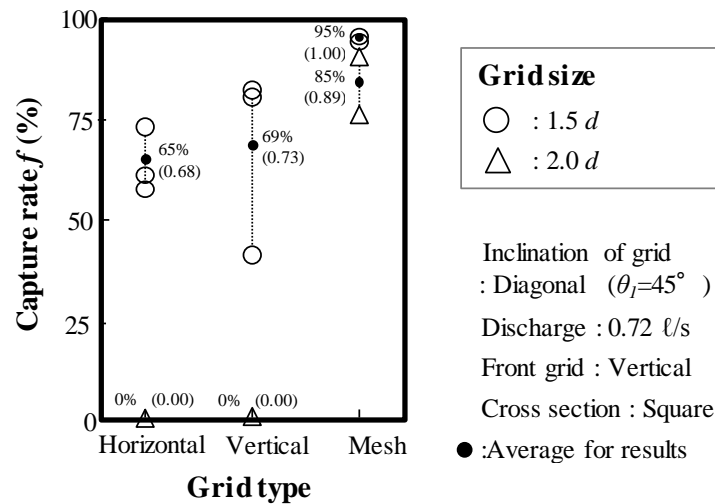


Figure 5.6: Effect of grid type on the capture rate (incline of the dam = 45°).

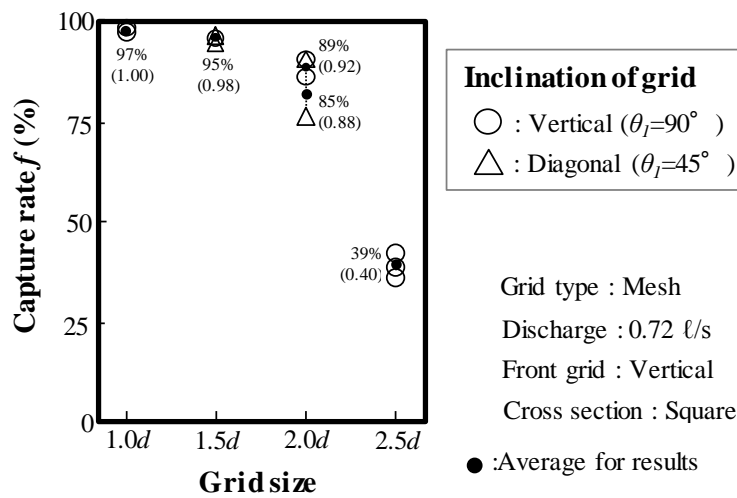


Figure 5.7: Effect of the permeable width grid-size on the capture rate (grid type = mesh grid).

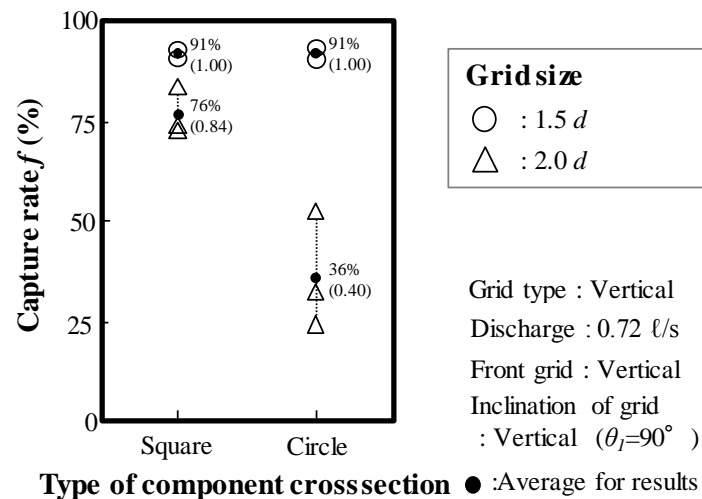


Figure 5.8: Effect of grid cross-section on the capture rate.

Figure 5.8 shows the relationship between the capture rate and the grid component cross-section. The cross-section did not affect the capture rate when the permeable width of the barricade was less than 1.5-fold the particle diameter, as shown in **Figure 5.8**. However, the square cross-section captured twofold more than the circular cross-section, possibly because particles center on the square component more easily without slipping, as shown in **Figure 5.1**, allowing an arch of particles to form rapidly. This promoted rapid blockage, which contributed to the high capture rate.

Figure 5.9 shows the relationship between the capture rate and discharge. No effect of discharge on capture rate was found when the permeable width of the barricade was twofold the coarse particle diameter, as shown in **Figure 5.9**, where the capture rate decreased in response to an increase in flow.

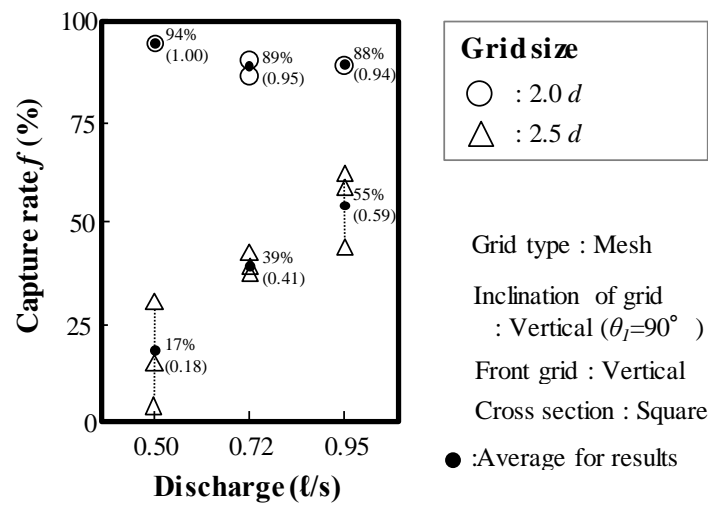


Figure 5.9: Effect of water discharge on the capture rate.

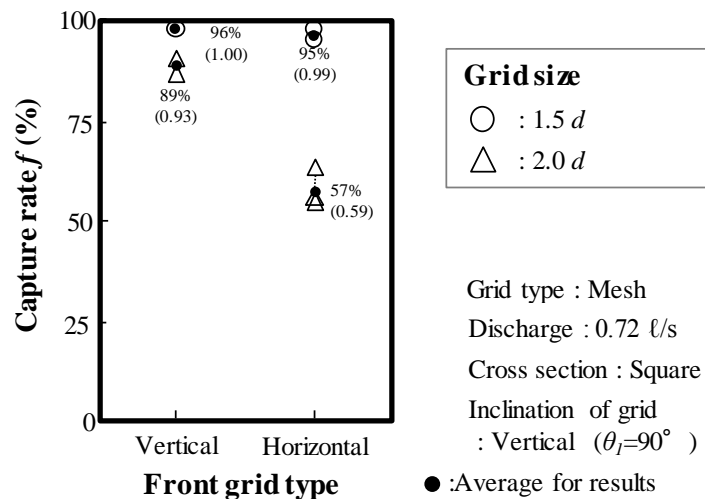


Figure 5.10: Effect of a front-bar-type mesh grid on the capture rate.

This is because almost all particles are initially captured by the barricade when the permeable width of the barricade is less than twofold the particle diameter. A proportion of the captured particles are eroded when flow overtops the dam; erosion due to overtopping causes a decrease in the capture rate. In contrast, the capture rate increases in response to an increase in flow when the permeable width of the barricade is 2.5-fold the particle diameter. To explain this, it is assumed that the flow velocity (including water and particles) increases due to the increase in flow; the increase in the particle-flow velocity affects the early blockage, as shown in **Figure 5.1**. Finally, the volume of particles flowing through the barricade decreases upon deposition. Future work is needed to verify the relationship between capture rate and flow velocity.

Figure 5.10 shows the relationship between capture rate and the mesh grid's component oriented

toward upstream as shown in **Figure 5.3** (upper right). No effect on capture rate was observed when the permeable width of the barricade was 1.5-fold the particle diameter, as shown in **Figure 5.10**. However, use of a front-bar type in a vertical oriented toward upstream demonstrated a capture rate ~ 1.5 -fold that of the horizontal oriented, when the permeable width of the barricade was 2.0-fold the particle diameter.

These results (**Figures 5.5 to 5.10**) indicate the ideal structure of the grid SABO dam, as shown in **Figure 5.11**. This configuration assumes that it is difficult to remove captured particles from the square grid; thus, this study proposes that a trapezoid grid would make maintenance simpler, and removing particles easier, than a square grid.

Experiments were conducted in cases 3-1 to 3-12, a scenario that involves two particle diameters ($d = 3.5$ & 7 mm), and CASE 3-13, which uses four particle diameters ($d = 1, 3.5, 7$ & 10 mm), as shown in **Table 5.3**. **Figure 5.12** shows the relationship between the capture rate and the volume concentration of the coarse particle (more than $d = 7$ mm) under debris flow. As shown in **Figure 5.12**, the x -axis is the volume concentration of coarse particles within debris flow C_L , and the y -axis is the capture rate when the permeable width of the barricade is twofold the coarse particle diameter; discharge did not affect capture rate when the permeable width of the barricade was twofold the particle diameter, as shown in **Figure 5.9**.

Figure 5.12 shows the regression line of each capture rate in cases 3-1 to 3-12 using each minimum capture rate. The correlation coefficient using the regression coefficient R was 0.94, as shown in **Figure 5.12**. Future work is needed to verify the regression coefficient.

Assuming that the necessary minimum capture-rate is 70 % to achieve a blockade, the necessary volume concentration C_L of coarse particles is more than 0.4 (40%), as shown in **Figure 5.12**.

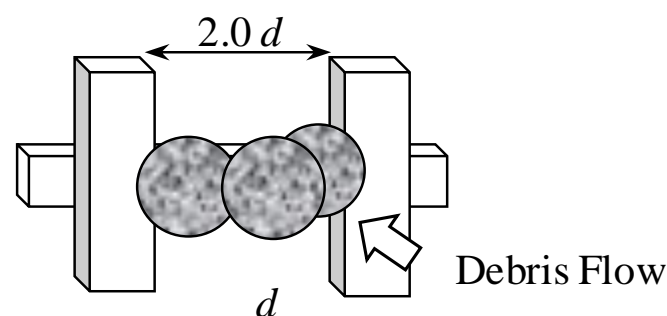


Figure 5.11: Schematic of an ideal grid SABO dam, based on the experimental results.

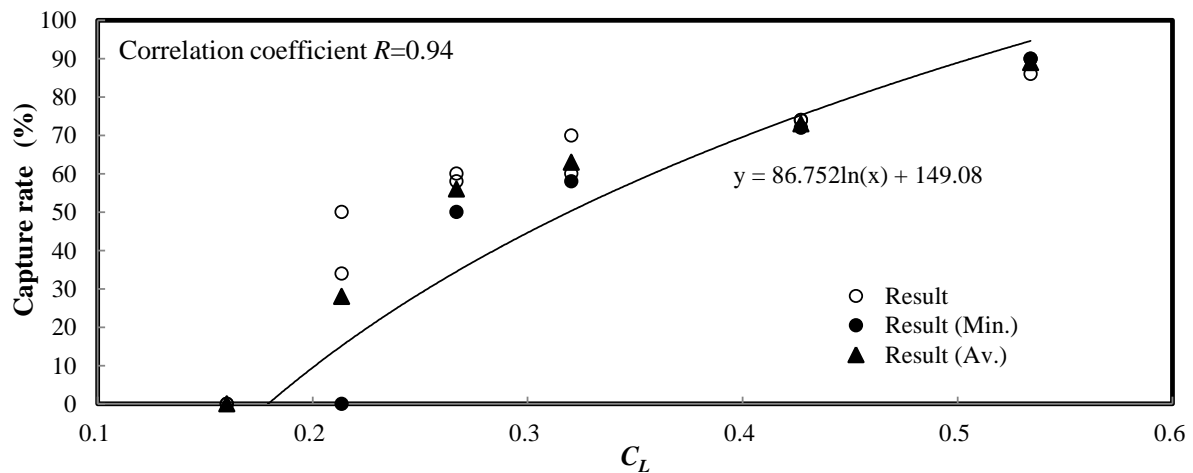


Figure 5.12: The relationship between capture rate and the volume concentration of coarse particles in sediment runoff (where grid size = twofold the coarse particle diameter).

5.3. Evaluating capture rate versus grain-size distribution in a real mountain streambed

To understand how the capture rate is affected by the particle diameter distribution, one first needs an understanding of the grain-size distribution encountered in the field, assuming to connect laboratory experiments to how this technology would function in real situations.

5.3.1. Examination conditions

Figure 5.13 shows the four distribution curves of the grain-size frequency under examination: three frequency distribution curves (Torrents A, B & C) were investigated in mountain streambeds, and one distribution curve (Test case) was assumed to understand how the capture rate is affected by grain-size distribution.

Figure 5.14 shows the grain-size accumulation rate, which is the relationship between the particle diameter and passage weight percentage using the grain-size frequency as shown in **Figure 5.13**, assuming the same distribution as in **Figures 5.13** and **5.14** in order to determine the effect of the grain-size distribution using the volume concentration of coarse particles in sediment runoff.

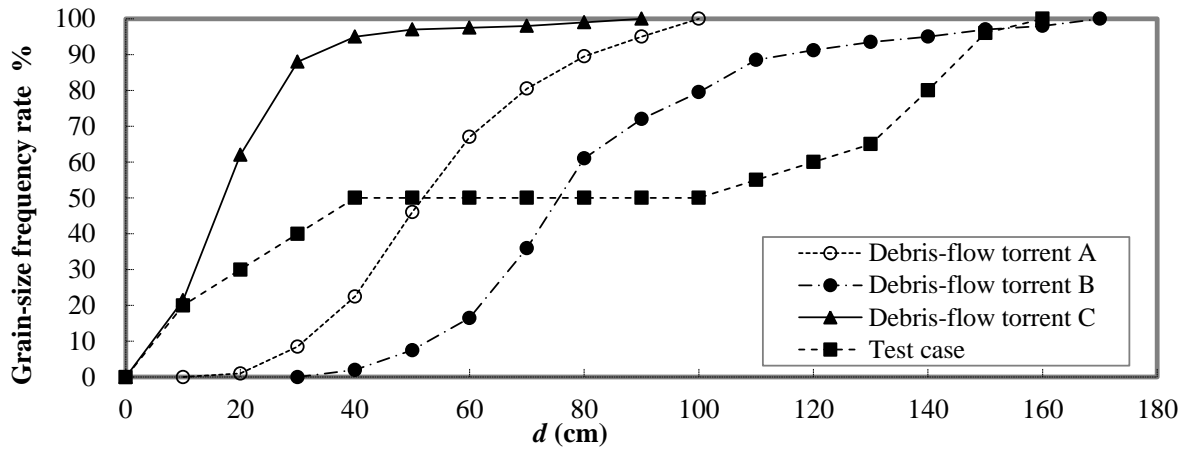


Figure 5.13: Distribution curves of grain-size frequency.

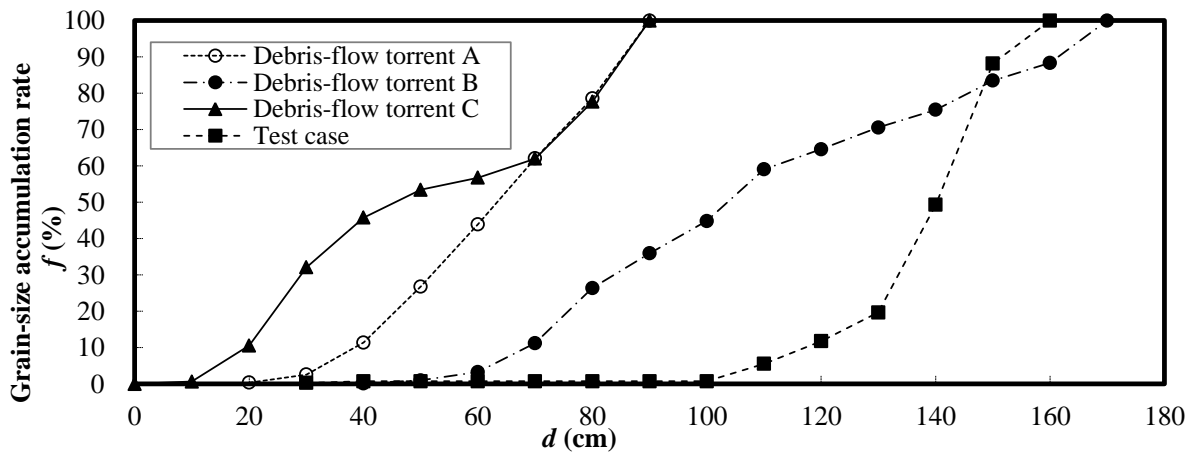


Figure 5.14: Grain-size distribution curve (relationship between the particle diameter and grain-size accumulation rate: passage weight percentage).

Previously, it was assumed that the riverbed incline around a dam is constant, that the incline would not change due to debris deposition on the riverbed, and that the volume concentration of coarse particles under debris flow is constant ($C_{max} = 0.54$: the design code for SABO dam, 2007). Additionally, it was assumed that the interstitial particle density is constant.

5.3.2. Relationship between the permeable barricade width and grain-size distribution

Table 5.5 shows the permeable width of the barricade as determined by the SABO dam design code (2000 & 2007) using grain-size distributions (Torrents A, B, C & Test case) as shown in Figure 5.14. Specifically, the permeable width of the barricade is 1.0 or 1.5-fold the coarse particle diameter (D_{95}), which was determined with Figure 5.13. The volume concentration of coarse particles ($C_L = 0.4$) necessary to cause blockage was divided by the volume concentration of all particles ($C_{max} = 0.54$).

Table 5.5: The permeable width of the barricade according to the 2000 & 2007 design codes, and the capture rate (%) of a grid planned according to the 2000 design code ($1.5D_{95}$).

	$1.5D_{95}$ (cm)	$1.0D_{95}$ (cm)	$2.0D_{CL}$ (cm)	Capture rate: $1.5D_{95}$ (%)
Torrent A	120	80	90	52
Torrent B	210	140	150	41
Torrent C	60	40	50	63
Test case	210	140	270	78

Table 5.5 shows an ideal grid of $2.0D_{cL}$ for the blockage, which is twofold the particle diameter d considering the coarse particle existence rate $f_{bL} = 24\%$, where $f_{bL} = (1 - C_L/C_{max}) \cdot 100\%$. The new width D_{cL} was determined by the grain-size distribution curves, as shown in **Figure 5.14**, using the calculated existence rate f_{bL} of coarse particles out of the total particles. This permeable barricade width of $2.0D_{cL}$ is ideal when the grain-size distribution is considered. A permeable width of $2.0D_{cL}$ lies in-between the width determined by the 2000 design code ($1.5D_{95}$) and that of the 2007 code ($1.0D_{95}$) for real mountain streams (Torrents A, B & C). In contrast, a barricade permeable width of $2.0D_{cL}$ in the test case is wider than those determined by the old and new design codes. Hence, consideration of the grain-size distribution is necessary prior to construction of a new SABO dam.

To understand the capture rate of a barricade with a permeable width of $1.5D_{95}$, as determined by the 2000 design code for mountain streambeds, the existence rate of the coarse particle fraction was calculated using the grain-size distribution, as shown in **Figure 5.14**. Finally, the volume concentration of coarse particles within the debris flow C_L was calculated by multiplying the existence rate of coarse particles f_{bL} by the volume concentration of all particles (where $C_{max} = 0.54$). **Table 5.5** shows the capture rate ($1.5D_{95}$) of mountain streambeds (Torrents A, B & C) shown in **Figure 5.14**, using both the volume concentration of coarse particles within debris flow C_L and the relationship between the capture rate and the volume concentration of coarse particles, as shown in **Figure 5.12**. The barricade capture rate changed with grain-size distribution; mountain streambeds (Torrents A, B & C) demonstrate a difference of 1.5-fold greater capture rate, as shown in **Table 5.5**. Additionally, the capture rate of a grid SABO dam built according to the specifications of the 2000 design code was less than 70% (*i.e.*, 41-63%).

This work assumes that the volume concentration of particles within a debris flow is constant. However, when a riverbed around a grid SABO dam is on a gradual incline or flat ground, coarse particles separate from debris flow, deposit on the riverbed and cannot flow to the barricade, as shown in **Chapter 1**. Hence, the barricade cannot capture fine particles without the formation of a blockage. The capture rate is discussed by considering the relationship between capture rate and the riverbed incline around the upstream the dam.

Using the relationship between the riverbed incline and the volume concentration of particles within the debris flow (the design code, 2007), the equilibrium concentration C_∞ at the point is expressed as:

$$C_\infty = \frac{\rho \tan \theta_w}{(\sigma - \rho)(\tan \phi - \tan \theta_w)}, \quad (5.1)$$

where ρ is the interstitial fluid, σ is the density of the particle, ϕ is the internal frictional angle of grit, and θ_w is the riverbed incline at that point. Assuming that the volume concentration of coarse particles within the debris flow C_L equals the equilibrium concentration at the point C_∞ in question, **Figure 5.15** shows the relationship between the riverbed incline and the volume concentration of particles C_∞ ($= C_L$) according to equation 5.1, where the volume concentration of the coarse particles C_L is assumed to be 0.54 (C_{max}), as per the 2007 design code.

To capture more than 70% of sediment flow using the barricade, the volume concentration of coarse particles in sediment runoff must be more than 40% as shown in **Figure 5.12**. In addition, when the internal frictional angle of the particle is 35° , the suggested riverbed angle must be greater than 13° , as shown in **Figure 5.15**.

Figure 5.16 shows the relationship between grain-size determined by distribution curve and the ideal permeable width of the barricade under incline conditions ($13\text{--}15^\circ$). The internal frictional angle of grit is assumed to be 35° , and the depth of debris flow is greater than the particle diameter.

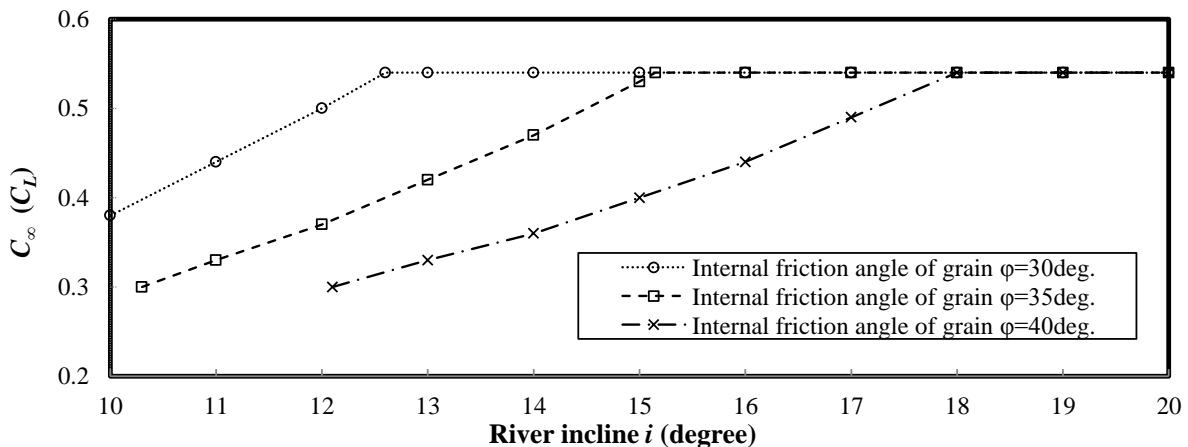


Figure 5.15: Relationship between the riverbed incline and the volume concentration of particles: the equilibrium concentration at each point.

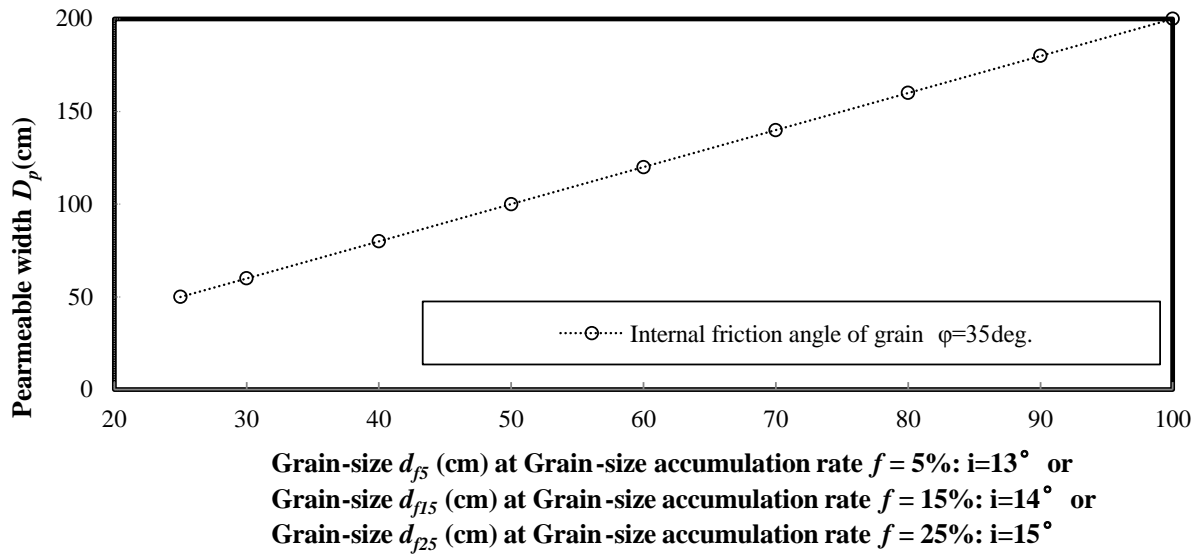


Figure 5.16: Relationship between the permeable barricade width and grain-size distribution curve.

The particle existence rate f is 5%, where $f = (1.0 - C_L/C_\infty) \cdot 100\%$, when the volume concentration of the coarse particles ($C_L = 0.4$, $C_\infty = 0.42$) necessary to blockade the barricade is divided by the volume concentration of particles on the riverbed incline (13°), as shown in **Figure 5.15**. Additionally, the particle existence rate f of the necessary volume concentrations of particles on riverbed inclines of 14° and 15° are 15% and 25%, respectively. The grain-size d_{j5-25} is calculated with the above particle-rate f using the grain-size distribution curve (e.g., **Figure 5.14**). Furthermore, the relationship between the permeable width of the barricade and the grain-size d_{j5-25} , as shown in **Figure 5.16**, can be used to describe the function of grid SABO dams.

5.4. Summary

To identify the ideal structure for controlling sediment runoff, this study examined the function of multiple grid SABO dam design parameters, and determined how capture rate is affected by different configurations. Additionally, the function of SABO dams constructed under different design codes was examined.

This work shows that the vertical component of the dam grid was critical in blocking sediment, whereas the horizontal component was less important. Considering the relationship between the permeable width of the barricade and capture rate, this suggests that the necessary permeable width of the barricade is less than approximately twofold the coarse particle size ($2.0d$). Additionally, these results show that a square grid retains more sediment than a round grid when considering capture rate. Furthermore, the vertical incline of the barricade, when compared to the riverbed and the mesh grid's

vertical component oriented toward upstream, is important in terms of optimizing capture rate. Assuming that these laboratory experiments are directly applicable to field function, the volume concentration of coarse particles should be greater than 0.4 (capture rate = more than 70%), and the permeable width of the barricade should be twofold the coarse particle diameter.

This study, which took into consideration the grain-size distribution in a mountain streambed, showed that the capture rate was markedly affected by the grain-size distribution. In terms of riverbed characteristics, the incline of the riverbed upstream of a dam must be greater than 13° to block more than 70% of sediment. Finally, this work suggests that the ideal permeable width of the barricade under different incline conditions (13° , 14° & 15°) should be determined with consideration of the grain-size distribution.

BIBLIOGRAPHY

1. Ashida K, Egashira S, Kurita M & Aramaki H. 1987. Debris flow controlled by grid dams. *Disaster Prevention Research Institute Annuals for Kyoto University*, Vol. 30/B: 441-456.
2. Hashimura K, Hashimoto H, Miyoshi T, Ikematu S, Hasuo S, Farouka M & Sakata K. 2012. Flume experiment for capture ability of wood, stone and water by grid SABO dam. *Annual research presentation meeting. Japan Society of Erosion Control Engineering*, B: 72-73.
3. Ministry of Construction, Japan. 2000. *Manual of Technical Standard for designing Sabo facilities against debris flow*.
4. Mizuno H, Mizuyama T, Minami T & Kuraoka C. 2000. Analysis of simulating debris flow captured by permeable type dam using Distinct Element Method. *Journal archive/sabo*, Vol. 52/ No.6: 4-11.
5. Mizuyama T, Kobashi S & Mizuno H. 1995. Control of passing sediment with grid-type dams. *Journal archive/sabo*, Vol. 47/ No.5: 8-13.
6. National Institute for Land and Infrastructure Management Ministry of Land, Japan. 2007. *Manual of Technical Standard for designing Sabo facilities against debris flow and driftwood*.
7. Takahashi T, Nakagawa H, Satofuka Y & Wang H. 2001. Stochastic model of blocking for a grid-type dam by large boulders in a debris flow. *Annual Journal of Hydro science and Hydraulic Engineering*, Vol. 45: 697-702.
8. Yazawa A, Mizuyama T & Morita A. 1986. Experiments and analysis on Debris Flow Braker screen. *Memorandum of PWRI*, Vol. 2374.

Chapter 6

Conclusion and Future Works

“These proverbs will give insight to the simple, knowledge and discernment to the young.”

Proverbs 1:4

This thesis discussed the prediction of sediment runoff in a mountain watershed and the countermeasures for debris control using experimental and simulation results, taking into consideration the structural design. This final chapter summarizes the results obtained in this study and outlines future work.

Chapter 2 discussed the deformation and flood outflow accompanying landslide dam failure and presented experiments with a small-scale artificial landslide dam in a mountain stream in order to understand these processes. The landslide dam deformation and outflow processes due to overtopping erosion using the experimental results were analyzed using a numerical model. The factors that affect flood outflow processes from a reservoir were analyzed using the calculated results, and the effects of moisture content on the erosion of landslide dams were investigated using a numerical model that incorporated both erosion and infiltration flow processes under saturated and unsaturated conditions. Experiments with a small-scale artificial landslide dam showed that erosion had a greater effect than other collapse processes. In addition, it examined the effects of the difference in the gradients upstream and downstream, difference in the water volume in the reservoir behind the landslide dam, and the difference in water depth caused by water exchange with deposit.

To understand the flood runoff to the downstream area affected by the characteristics of the inflow hydrograph from the reservoir (*e.g.*, pond or landslide dam), **Chapter 3** analyzed the relationship between the effects and characteristics of the hydrograph from the reservoir using a one-dimensional numerical model that took into consideration the water and sediment flow. The results suggested that the characteristics of the inflow hydrograph from the reservoir due to the levee failure affected flood runoff processes downstream. In addition, a new index of flood hazard grade in the downstream areas was proposed, considering the characteristics of the inflow hydrograph from the reservoir.

To confirm the validity of the developed numerical model based on Hirasawa *et al.*, 2012, which predicted the flood and sediment runoff using the rainfall intensity, **Chapter 4** compared the calculated and observed data for a mountainous area. Considering the geology and vegetation in the basin, a relationship between the channel width and area of the upper basin was inferred using regression analysis; the calculated results were verified by comparison with field observations. This comparison suggested that it is necessary to consider the sediment yield in rainfall–runoff prediction in mountainous areas, which yields more sediment than other areas.

To identify the ideal structure for controlling sediment runoff, **Chapter 5** examined the function of multiple grid SABO dam design parameters, and determined how different configurations affect the capture rate. In addition, the function of SABO dams constructed under different design codes was examined. This work shows that the vertical component of the dam grid was critical for blocking sediment, whereas the horizontal component was less important. Moreover, the experimental results show that a square grid retains more sediment than a round grid when considering capture rate. Furthermore, the vertical incline of the barricade when compared to the riverbed and the mesh grid's vertical component oriented toward upstream, is important in terms of optimizing capture rate. This study considered the grain-size distribution in a mountain streambed and showed that the capture rate was markedly affected by the grain-size distribution.

This thesis showed that the designers of structures that control sediment runoff should consider topography, particle diameter distribution, and precipitation conditions. However, the exact mechanisms of sediment yield and flood runoff processes from mountainous areas are not fully understood, as shown in this thesis. More work is needed to identify the applicability to other watersheds of the proposed prediction and control method for sediment runoff, and to verify the assumed coefficient in this thesis.

